POLITECNICO DI TORINO
I Facoltà di Ingegneria

Master of Science in Civil Engineering

Master’s Degree Thesis

Study of the behaviour at failure of complex materials at different observation scales

Supervisor:
Prof. ^{ssa} Monica Barbero

Co-supervisors:
Ing. Maria Lia Napoli
Ing. Lorenzo Milan

Candidate:
Salvatore Agrillo

July 2021

Summary

Introduction **13**

1. Structurally complex formations **14**

1.1 Mélanges 14

1.2 Critical aspects 17

1.2.1 Geological complexity 18

1.2.2 Geotechnical complexity 19

1.2.3 Engineering complexity 20

1.2.4 In-situ sampling 21

1.2.5 Laboratory characterization 22

1.3 Characteristic engineering dimension L_c 23

1.4 Mechanical behaviour of a structurally complex formation 25

1.4.1 Lindquist's experimental study (1994) 26

1.4.2 Sonmez et al. experimental study (2006) 30

1.4.3 Zhang et al. experimental study (2016) 34

2. Tortuous failure surfaces **37**

2.1 Study on tortuous failure surfaces conducted by Medley (2004) 38

2.2 Study on tortuous failure surfaces conducted by Montoya-Araque et al. (2020) 41

2.2.1 pyBIMstab software and A* algorithm 46

3. Contribution to the study of tortuous failure surfaces **48**

3.1 Study on tortuous failure surfaces conducted by Napoli et al. 49

3.2 Average tortuosity index and standard deviation as VBP varies 53

3.3 Bimslopes stability analysis: failure zone width 56

3.4 Failure zone width estimation as VBP varies 61

3.5 Results comparison and considerations 64

4. Triaxial tests on laboratory reconstituted material **65**

4.1 Triaxial test overview ... 66
    4.1.1 UU test ... 70
    4.1.2 CD and CU tests ... 71
4.2 Triaxial CIU test ... 72
    4.2.1 Skempton's coefficient A and B ... 72
    4.2.2 Equipment ... 79
    4.2.3 Installation and assembly ... 87
    4.2.4 Saturation, Consolidation and Shear phases ... 89
4.3 Reconstituted samples preparation ... 93
    4.3.1 Settlement under one-dimensional conditions ... 101
    4.3.2 One-dimensional consolidation theory ... 104
5. Test results ... 108
5.1 Triaxial tests on homogeneous material ... 109
5.2 Triaxial tests on heterogeneous material ... 117
5.3 Test results interpretation ... 122
Conclusions and future developments ... 129
Bibliography ... 131
Annex 1 ... 134
Annex 2 ... 137
Annex 3 ... 139
Acknowledgments ... 141

Summary of the figures

Figure 1: Global mélanges distribution (Festa et al., 2010). 15

Figure 2: Representation of the chaotic configuration of the Franciscan Mélange (Medley et al., 1994). 15

Figure 3: Different block types inside the in the mélange present in the Marin County north of San Francisco (Medley, 2001). 16

Figure 4: Samples of sedimentary mélange of the Oltrepò Pavese area artificially cut to show the internal composition (Milan, 2020). 17

Figure 5: Extraction of a Oltrepò Pavese mélange sample (highlighted in red) using hammer and chisel (Cerise, 2019). 22

Figure 6: Example demonstrating the influence of block size on the scale of interest: the black block of size of 1 m considerably influences the implementation of a pipeline represented with the dotted line, while it is considered as part of the matrix if you consider the entire area of 100 x 100 m^2 (Medley, 2001). 24

Figure 7: Weights of the elements forming the matrix and blocks (Lindquist, 1994). ... 27

Figure 8: Rappresentazione grafica dei modelli fisici impiegati per la determinazione delle caratteristiche (Lindquist, 1994). 27

Figure 9: Variation of the internal friction angle for the different VBP and for different block orientations with respect to the application of the maximum load (Lindquist, 1994). 29

Figure 10: Variation in cohesion for different VBP and for different block orientations with respect to the application of the maximum load (Lindquist, 1994). 29

Figure 11: Stages of preparation of artificial bimrock samples (Sonmez et al., 2006). 31

Figure 12: Cumulative frequency of error ratio, obtained using the values of σ_1 evaluated with the empirical solutions found from Mohr-Coulomb and Hoek & Brown equations (Sonmez et al., 2006). 33

Figure 13: Grading curves of the four types of samples used for the triaxial tests (Zhang et al., 2016). 35

Figure 14: CT triaxial apparatus and workstations (Zhang et al., 2016). 36

Figure 15: 3D CT images of the four types of samples (Zhang et al., 2016). 36

Figure 16: Shear strenght parameters of the four types of samples obtained from the triaxial tests at different confining pressures (Zhang et al., 2016). 37

Figure 17: Measurement were made of: a) the length of the breaking tortuous surface (yellow highlighted line), b) the estimated length of the average smooth surface (red line); and c) the total length of the block contacts along the failure surface (Medley, 2004). 38

Figure 18: Scans of traced lines of failure surfaces and compared to type profiles for JRC 10 to 20 (Barton et al., 1977). 39

Figure 19: Parameters measured and calculated from traced lines of tortuous failure surfaces (Medley, 2004). 40

Figure 20: The most basic bimslope model (Montoya-Araque et al., 2020). 42

Figure 21: Triangular mesh inside the polygon of the bimslope boundary with each triangle filled with circular blocks of different sizes (Montoya-Araque et al., 2020). ... 42

Figure 22: Bimslope model with circular blocks of different sizes (Montoya-Araque et al., 2020). 43

Figure 23: Matrix-only circular failure surface and Tortuous failure surface inside a bimslope (Montoya-Araque et al., 2020). 44

Figure 24: Profile of the Tortuous failure surface lenght along the straightened Matrix-only failure surface length (Montoya-Araque et al., 2020). 44

Figure 25: Possible Tortuous failure surfaces profiles for different Areal Block Proportions (ABPs) with respect the perpendicular depth d starting from the slope surface. It's evident that the roughest profiles are traced for the highest ABP (Montoya-Araque et al., 2020). 45

Figure 26: Ten modules with their respective classes (Montoya-Araque et al., 2018).. 46

Figure 27: Grid graph representation of a cell array with hindered cells (black cells), allowed cells (grey cells) in which the path can be traced and cells out of the problem frame (white cells) (Montoya-Araque et al., 2019). 47

Figure 28: (a) TFS obtained with the classical A pathfinding algorithm, (b) TFS obtained with the modified A* pathfinding algorithm (Montoya-Araque et al., 2019).*. 48

Figure 29: Circular failure surface obtained in the homogeneous material with VBP = 0%. 49

Figure 30: TFS path with VBP = 25%. 50

Figure 31: TFS path with VBP = 70%. 50

Figure 32: Overlapping of all the 15 TFS obtained from the 15 models with VBP = 25%. 51

Figure 33: Scheme of the image proportions used to find the tortuosity index in Montoya et al. (2020) research. 52

Figure 34: Scheme of the image proportions used to find the tortuosity index in this thesis. 52

Figure 35: Models obtained on RS2 and imported on AutoCAD. 54

Figure 36: Average tortuosity index and Standard deviation trends as a function of VBP. 55

Figure 37: Band of potential tortuous failure surfaces obtained overlapping the tortuous failure surfaces obtained from the 15 models with VBP = 25%. 56

Figure 38: Band of potential tortuous failure surfaces obtained overlapping the tortuous failure surfaces obtained from the 15 models with VBP = 40%. 57

Figure 39: Band of potential tortuous failure surfaces obtained overlapping the tortuous failure surfaces obtained from the 15 models with VBP = 55%. 57

Figure 40: Band of potential tortuous failure surfaces obtained overlapping the tortuous failure surfaces obtained from the 15 models with VBP = 70%. 58

Figure 41: Failure zone width identified in case of VBP = 25%. 58

Figure 42: Failure zone width identified in case of VBP = 40%. 59

Figure 43: Failure zone width identified in case of VBP = 55%. 59

Figure 44: Failure zone width identified in case of VBP = 70%. The minimum fictitious tortuous failure surface in this case is very superficial. 60

Figure 45: Minimum fictitious tortuous failure surface in case of VBP = 70%. 60

Figure 46: Maximum depths of the maximum and minimum fictitious tortuous failure surfaces in case of VBP = 25%. 61

Figure 47: Maximum depths of the maximum and minimum fictitious tortuous failure surfaces in case of VBP = 40%. 61

Figure 48: Maximum depths of the maximum and minimum fictitious tortuous failure surfaces in case of VBP = 55%. 62

Figure 49: Maximum depths of the maximum and minimum fictitious tortuous failure surfaces in case of VBP = 70%. 62

Figure 50: Maximum depth of the minimum fictitious tortuous failure surface in case of VBP = 70%. 62

Figure 51: dmin /L_c and dmax /L_c trends as a function of VBP. 64

Figure 52: Mohr – Coulomb circles at failure and strenght characteristics in effective stresses (AGI, 1994). 67

Figure 53: Failure envelopes of three samples in terms of total stresses (Cianci et al., 2016). 71

Figure 54: Initial state (Whitlow, 1996). 73

Figure 55: Instantaneous increase of the total stress state (Whitlow, 1996). 73

Figure 56: Decomposition of the increase of the total stress state (Whitlow, 1996). 74

Figure 57: Typical relationship between Skempton's coefficient B and degree of saturation S_r *(Whitlow, 1996).* 77

Figure 58: Triaxial test equipment cross section (Lancellotta, 2012). 80

Figure 59: Triaxial cell in the geotechnical laboratory of the Polytechnic of Turin. It is possible to observe the tested sample wrapped by the latex membrane, the transducers for measuring pore pressure at the top and at the bottom of the specimen (1), the transducer for measuring vertical displacements (LVDT) (2), the connecting valves to cell pressure control system and filling tank (3), the transducer for measuring cell pressure (4), the load cell for axial load measurement (5), the anchor pin for securing the cylindrical plexiglass container (6). 81

Figure 60: "Air-water" pressure transmission system. 82

Figure 61: Volumometer and LVDT displacement transducer. 85

Figure 62: Sample preparation equipment. 86

Figure 63: Consolidation curve in isotropic compression phase (AGI, 1994). 91

Figure 64: Pieces of sedimentary mélange of the Oltrepò Pavese area dissolved in water. 93

Figure 65: Liquid mixture filtered through a 75 μm sieve (ASTM E-11). 94

Figure 66: Mixture dried in the oven and spatulated. 94

Figure 67: Weighed fine gravel with sizes comprised between 2 mm and 4.75 mm. 95

Figure 68: Filling of the consolidometer steel cylinder. One half is filled with material with VBP = 25% and the other half with VBP = 45%. 96

Figure 69: Consolidometer in the Laboratory of Geotechnics of the Polytechnic of Turin used to consolidate the material. It's possible to observe the load cell display (1), the load cell (2), the LVDT transducer to measure the vertical displacements (3), the piston for axial load application (4) and the steel cylinder containing the material (5). 97

Figure 70: Sample of consolidated material extracted from the consolidometer. 98

Figure 71: Six wedges of paraffinized consolidated material, three wedges with VBP = 25% and other three with VBP = 45%. 99

Figure 72: Sample of heterogeneous material after cutting. 100

Figure 73: Final reconstituted specimen of heterogeneous material. 100

Figure 74: Paraffinized samples. 101

Figure 75: The three separated phases of an equivalent volume of a generic soil sample (Lancellotta, 2012). 102

Figure 76: Total and effective stress paths obtained from the four triaxial tests carried out on the homogeneous reconstituted samples with VBP = 0%. 110

Figure 77: Failure surface of the specimen obtained from the TX 315 test having VBP = 0% after a consolidation of 25 kPa. 111

Figure 78: In the image on the left the failure surface of the specimen obtained from the TX 304 test having VBP = 0% after a consolidation of 50 kPa is represented. Instead in the image on right the failure surface of the specimen obtained from the TX 302 test having VBP = 0% after a consolidation of 100 kPa is represented (Milan, 2020). 112

Figure 79: Barrel deformation of the TX 303 test specimen (Milan, 2020). 112

Figure 80: Deviatoric stress trends as a function of axial strain during the four triaxial tests on homogeneous reconstituted samples with VBP = 0%. 113

Figure 81: Excess pore pressure trends as a function of axial strain during the four triaxial tests on homogeneous reconstituted samples with VBP = 0%. 114

Figure 82: Deviatoric force trends during triaxial tests on homogeneous reconstituted samples with VBP = 0%. 115

Figure 83: Total and effective stress paths obtained from the four triaxial tests carried out on the heterogeneous reconstituted samples with VBP = 25%. 118

Figure 84: Total and effective stress paths obtained from the four triaxial tests carried out on the heterogeneous reconstituted samples with VBP = 45%. 118

Figure 85: Deviatoric stress trend as a function of axial strain during the four triaxial tests on heterogeneous reconstituted samples with VBP = 25%. 119

Figure 86: Deviatoric stress trend as a function of axial strain during the four triaxial tests on heterogeneous reconstituted samples with VBP = 45%. 120

Figure 87: Excess pore pressure trends as a function of axial strain during the four triaxial tests on heterogeneous reconstituted samples with VBP = 25%. 121

Figure 88: Excess pore pressure trends as a function of axial strain during the four triaxial tests on heterogeneous reconstituted samples with VBP = 45%. 122

Figure 89: Deviatoric stress trends obtained from triaxial tests confined at 25 kPa as a function of axial strain varying the VBP. 124

Figure 90: Deviatoric stress trends obtained from triaxial tests confined at 50 kPa as a function of axial strain varying the VBP. 125

Figure 91: Deviatoric stress trends obtained from triaxial tests confined at 100 kPa as a function of axial strain varying the VBP. 125

Figure 92: Deviatoric stress trends obtained from triaxial tests confined at 200 kPa as a function of axial strain varying the VBP. 126

Figure 93: Effective cohesion trend as a function of VBP. 128

Figure 94: Effective friction angle trend as a function of VBP. 128

Figure 95: TX 317 sample confined at 25 kPa with VBP = 25%. 134

Figure 96: TX 319 sample confined at 50 kPa with VBP = 25%. 134

Figure 97: TX 312 sample confined at 100 kPa with VBP = 25%. 135

Figure 98: TX 318 sample confined at 200 kPa with VBP = 25%. 135

Figure 99: TX 320 sample confined at 25 kPa with VBP = 45%. 135

Figure 100: TX 310 sample confined at 50 kPa with VBP = 45%. 136

Figure 101: TX 313 sample confined at 100 kPa with VBP = 45%. 136

Figure 102: TX 321 sample confined at 200 kPa with VBP = 45%. 136

Figure 103: Change in effective stress paths of all the samples confined at 25 kPa as a function of VBP. 137

Figure 104: Change in effective stress paths of all the samples confined at 50 kPa as a function of VBP. 137

Figure 105: Change in effective stress paths of all the samples confined at 100 kPa as a function of VBP. 138

Figure 106: Change in effective stress paths of all the samples confined at 200 kPa as a function of VBP. 138

Figure 107: Excess pore pressure trends as a function of axial strain of all the samples confined at 25 kPa varying the VBP. 139

Figure 108: Excess pore pressure trends as a function of axial strain of all the samples confined at 50 kPa varying the VBP. 139

Figure 109:Excess pore pressure trends as a function of axial strain of all the samples confined at 100 kPa varying the VBP. 140

Figure 110: Excess pore pressure trends as a function of axial strain of all the samples confined at 200 kPa varying the VBP. 140

Summary of the tables

Table 1: Mohr-Coulomb empirical equations normalized with respect to the matrix parameters (Sonmez et al., 2006). 32

Table 2: Hoek & Brown empirical equations normalized with respect to the matrix parameters (Sonmez et al., 2006). 32

Table 3: Summary of the values obtained from Medley's experiments (Medley, 2004). 41

Table 4: Average tortuosity index and Standard deviation values obtained for each VBP. 55

Table 5: d_{min} *and* d_{max} *values for each VBP.* 63

Table 6: d_{min}/L_c *and* d_{max}/L_c *values for each VBP.* 63

Table 7: Relationship between the degree of saturation of the tested sample and the applicable back pressure according to AGI (1994). 90

Table 8: Characteristics of the specimens used to perform triaxial tests. The specimens highlighted in orange were tested and elaborated by Milan in 2020. The specimens highlighted in blue were tested and elaborated in this thesis. 108

Table 9: Shear strenght parameters c' and φ' obtained from the homogeneous reconstituted tested samples with VBP = 0%. 111

Table 10: Axial strain values at failure for each radial confinement σ'_r *with VBP = 0%.* 116

Table 11: Values of the secant modulus corresponding to the range of axial strain [0%; 0.1%] $E_{0.1\%}$*, to a deviatoric stress equal to half of the deviatoric stress at failure* $E_{0.5}$ *and to an axial strain of 9% (value of the axial strain at failure)* $E_{9\%}$ *of the homogeneous reconstituted samples with VBP = 0%.* 117

Table 12: Coefficients m and q *obtained from the interpolating lines and shear strenght parameters c' and φ' for the cases with VBP = 25% and VBP = 45%.* 119

Table 13: Values of the secant modulus corresponding to the range of axial strain [0%; 0.1%] $E_{0.1\%}$*, to a deviatoric stress equal to half of the deviatoric stress at failure* $E_{0.5}$ *and to an axial strain of 9%* $E_{9\%}$ *of the heterogeneous reconstituted samples with VBP = 25%.* 120

Table 14: Values of the secant modulus corresponding to the range of axial strain [0%; 0.1%] $E_{0.1\%}$*, to a deviatoric stress equal to half of the deviatoric stress at failure* $E_{0.5}$ *and to an axial strain of 9%* $E_{9\%}$ *of the heterogeneous reconstituted samples with VBP = 45%.* 121

Table 15: Axial strain values at failure of each tested sample for different effective confinement in function of VBP. 126

Table 16: Values of the secant modulus corresponding to the range of axial strain [0%; 0.1%] $E_{0.1\%}$*, to a deviatoric stress equal to half of the deviatoric stress at failure* $E_{0.5}$ *and to an axial strain of 9% (value at failure of the homogeneous samples)* $E_{9\%}$ *of all the tested samples for different effective confinements in function of VBP.* 127

Introduction

The purpose of this paper is to define to study the behaviour at failure of a complex block in matrix formation at different observation scale, with particular attention to the influence of the volumetric percentage of blocks (VBP) on its behaviour. The term "complex block in matrix formations" refers to heterogeneous geological formations as mélange, bimsoil or bimrocks, which consist essentially in blocks incorporated into a weaker matrix. Because of their composition and structure, are difficult to classify and involve considerable problems in their characterization and definition of shear strenght parameters (AGI, 1979). The mechanical behaviour of these materials is difficult to characterize due to the many difficulties that arise in laboratory sampling and testing. From an engineering point of view, the variability of mechanical behaviour that characterizes these materials is problematic because it creates difficulties in design and construction of engineering works such as excavations, tunnels and /or slope stabilization works. Currently designers who face geotechnical designs in complex formations with block-in-matrix fabric do not have enough data to make their real mechanical behaviour reliable, so the design practice presents several difficulties due to the absence of certain methods to make reliable the design data relating to the values of: resistance, deformability and volumetric blocks proportion (VBP). Therefore, the study conducted in this thesis project has been developed on two parts concerning the issues presented above but analyzing them with two different observation scales. First, critical aspects related to complex materials were evaluated at in-situ scale. The purpose was to estimate how the average tortuosity index varies according to the VBP within a bimslope and to identify a failure zone width, which can be useful to designers in making correct assessments of the technical and economic feasibility of the intervention that is intended to be carried out.

In the second part of the thesis, a laboratory testing campaign already started by Milan in 2020 was conducted. It was carried out using non-conventional methods in order to analyse the mechanical behaviour of the matrix and heterogeneous material. Triaxial tests have been performed to evaluate the influence of VBP on the mechanical behaviour of a heterogeneous material reconstituted in the laboratory from the matrix of the Oltrepò Pavese samples, due to the impossibility to carry out its sampling. The results showed a significant influence of VBP on shear strenght, stiffness, and post-failure behaviour of the specimens.

1. Structurally complex formations

Many geological formations, because of their composition and structure, cause many difficulties in solving engineering problems and cannot be easily classified from a geotechnical point of view. Formations of this type are widespread all over the world and have been conventionally called "structurally complex" (AGI, 1979). The complexity is due to the extreme heterogeneity that distinguishes them, making their classification very difficult. These complex formations include a large family of materials linked to phenomena of sedimentary tectonic origin or to chemical and physical processes. The study of such formations is complex because of the variability of the mechanical characteristics of the components: the strenght parameters may vary in different orders of magnitude and this increases difficulties in choosing the geo-mechanical reference model to be adopted. The overall mechanical behaviour of a formation cannot be associated either with that of a rock mass or with that of a soil. In fact, the strength properties depend on the characteristics of individual components, their spatial distribution, and their mutual interactions.

1.1 Mélanges

Complex formations include a wide variety of geological bodies. Within the various types of complex formations, it is possible to make a first distinction between *bimrock* (*block-in-matrix rock)* and *bimsoil* (*block-in-matrix soil*). The first was introduced by Medley et. al in 1994 giving this definition: *"a mixture of rocks composed of geotechnically significant blocks within a bonded matrix of finer texture"*. The term *"geotechnically significant blocks"* underlines the contrast in terms of mechanical strength between blocks and matrix and that the size and number of clasts play a fundamental role in the evaluation of mechanical properties of the bimrock. While the term bimsoil describes a material like bimrock but with an inconsistent matrix with poor mechanical characteristics. Different types of material belong to the category of bimrock including *mélanges* (Medley, 2002); they have originated in mountainous areas because of tectonic motions of subduction in over 60 countries worldwide (Figure 1).

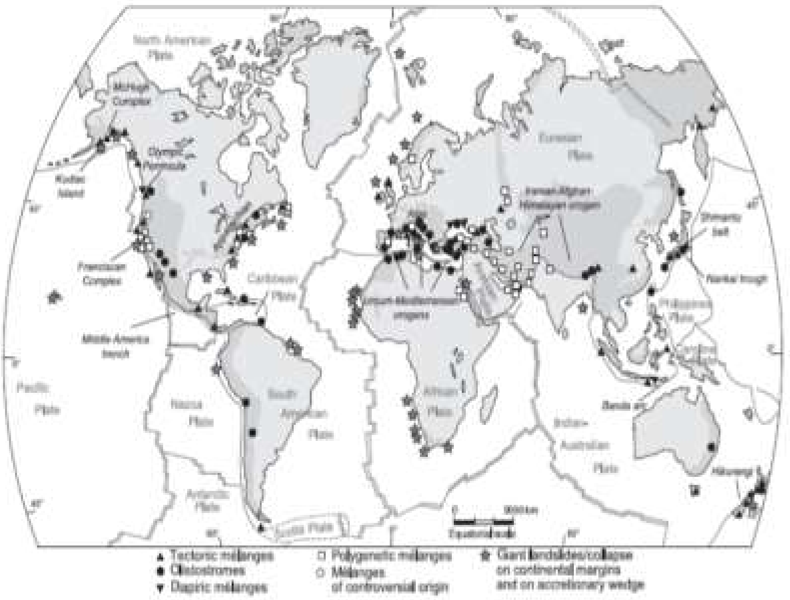

Figure 1: Global mélanges distribution (Festa et al., 2010).

Medley ranked mélanges like that subgroup of bimrocks that manifests more problems from the engineering point of view (Medley, 2002). The interest for structurally complex rock formations was born with Medley's study about a particular type of mélange, called *Franciscan Mélange*, located in northern California. This geological formation consists of sedimentary rock formations immersed in a sheared clay matrix (Figure 2). From a textural point of view, the Franciscan Complex consists of the typical structural mélanges conformation which contains heterometric and heterogeneous blocks chaotically arranged inside the matrix (Medley et al., 1994).

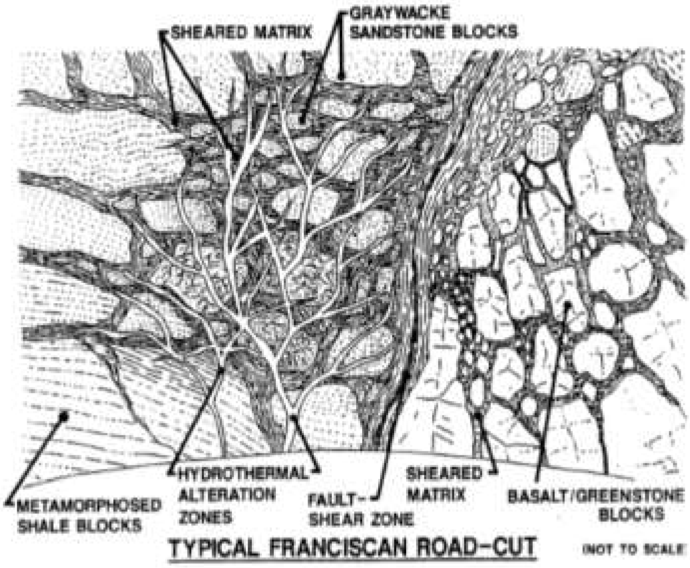

Figure 2: Representation of the chaotic configuration of the Franciscan Mélange (Medley et al., 1994).

Within the Franciscan Complex the lithology of the materials involved is extremely variable and this was also evident from the studies conducted by Medley in 2001, through which the author confirmed the great variability. In particular, he estimated that in the mélange present in the Marin County north of San Francisco (Figure 3), the blocks belong to different types and, specifically about 60% to 70% of blocks are greywacke which is an arenaceous sedimentary rock, from 15% to 20% are volcanic, 15% to 20% are serpentinite, 5% to 10% are chert which is a siliceous sedimentary rock, and the remaining blocks are rare limestone and exotic metamorphic rock.

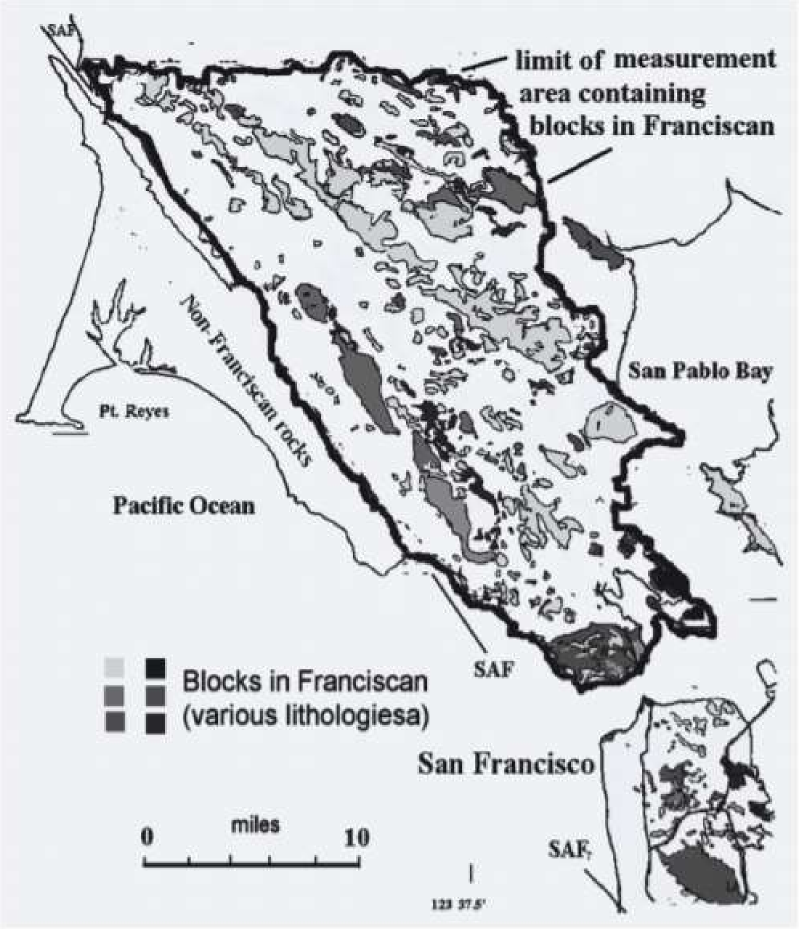

Figure 3: Different block types inside the in the mélange present in the Marin County north of San Francisco (Medley, 2001).

Starting from the study of this complex rock formation, over the years further surveys and studies were conducted concerning heterogeneous rock masses identified also in other locations. In Italy, for example, the focus has been on the analysis of clays located in the Tuscan-Emilian Apennines and in some areas of southern Italy (Wakabayashi et al., 2004). The samples analysed in this thesis were collected on 18/04/2018 from an outcrop of the Vogherese Apennines between Borgo Priolo and Ruino, in the Oltrepò Pavese area (Milan, 2020). It is a sedimentary mélange characterized by variable dimensional gradation, which has a stratigraphy with a decreasing volumetric percentage of blocks (VBP) as depth increases. The material consists of limestone blocks incorporated in a marly matrix (Figure 4).

Figure 4: Samples of sedimentary mélange of the Oltrepò Pavese area artificially cut to show the internal composition (Milan, 2020).

1.2 Critical aspects

The structurally complex formations are not classifiable neither as rock masses nor as soils, therefore, their mechanical characterisation cannot be conducted by the classical methods used in rock mechanics and in soil mechanics. The complexity that distinguishes these materials can take on different connotations depending on whether it is assessed from a geological, geotechnical, and engineering point of view.

1.2.1 Geological complexity

The definition of geological complexity is not simple, in fact it is possible to assess the complexity as a function of the geological history and the heterogeneity of the formation materials, although these two concepts do not appear to be very disconnected. In fact, a dependence is possible if the heterogeneity of the formation is the result of a complex geological history, however, is not possible to apply the contrary. The geological history does not necessarily presuppose heterogeneity because a series of genetic and epigenetic processes can lead the degree of heterogeneity of formation to decrease (Dzulynski, 1977). The ambiguity is also found about the more specific term of structurally complex formations. The sense of the “structural” attribute can be related to the current formation situation, without taking into account the processes that led to have that particular appearance; on the other hand it highlights the tectonic process that include all those complex formations whose heterogeneity is due exclusively to fractures, faults or permanent deformations (Barbier, 1977). The heterogeneity of complex formations can be the result of multiple variables combined, in fact the origin of the formations can be of various type, including a wide range of deposits, including sedimentary, evaporitic, igneous, volcanic and turbidic. However, it is important to underline that the overlap and succession of different processes does not necessarily lead to an increase in complexity. In fact, in some cases, a very intense degradation process can destroy all traces of previous processes and produce a structure with almost homogeneous characteristics. In general, the origin can be classified according to a genetic or epigenetic process, related to deformations and changes in diagenesis after deposit formation, or coating, related to climatic actions (Dzulynski, 1977). Different mechanisms are included in the genetic process: sedimentary and metamorphic, where deposits are characterized in general by the alternation of various materials; glacial mechanisms and subglacial erosions, where the moraines of Central Europe or North America are characterised by fractions of fine-grained or coarse-grained soil with variable presence of small or large blocks; mechanisms of moving boulders as the outcrops of breaches and finally mechanisms in which magma penetrates sedimentary formations giving rise to igneous deposits. Epigenetic processes group up: tectonic mechanisms including a variety of fractured rocks, sudden changes in the orientation of schistosity and layers of material due to overlapping plates and finally tectonic mélanges characterized by fragments of rock included inside of a fine-grained matrix; transformations due to atmospheric agents, such as the case of rocks characterized by the presence of open discontinuities submitted to water seepage which produce chemical processes; alterations, even at great depth, due to water or thermal changes that lead to a change in structure and mechanical characteristics; finally by combinations of phenomena, such as rocks altered by water or heat nearby a fault line (Anagnostou et al., 2014).

In conclusion, the geological complexity indicates a heterogeneity from the geological history and lithology point of view. The concept of heterogeneity should be considered in relation to the scale of analysis, since depending on it, a material can be considered homogeneous or heterogeneous. All materials in microscopic scale are however classifiable as heterogeneous and discontinuous.

1.2.2 Geotechnical complexity

Geotechnical complexity means the high variability and heterogeneity of geotechnical properties. It differs from geological complexity since the latter does not imply necessarily a geotechnical complexity (Morgenstern et. al, 1977). The Italian Geotechnical Association (AGI, 1979) has decided to use the concept of geotechnical complexity indicating as complex the formations which heterogeneities created extreme difficulties in samples creation for carrying out representative tests at an engineering scale, both as regards the mechanical characterisation and at the design and executive stage. Geotechnical complexity may affect formations which from a geological point of view are not complex. It is the case of homogeneous deposits of sensitive marine clays which are considered complex formations in relation to the difficulty of characterizing their geotechnical behaviour instead they are considered homogeneous from the geological point of view (Morgenstern et al., 1977). The concept of geotechnical complexity includes, in addition to phenomena of heterogeneity and variability of geotechnical characteristics, formations in which the characterization of the behaviour was found to be unusual. Geotechnically complex formations have not conceptual schemes, calculation methods and experimental and executive techniques, precisely because such behaviour hasn’t been found before in other situations.

This causes difficulties in characterizing the material leading to further difficulties in the design phase and in the construction phase of the engineering work.

1.2.3 Engineering complexity

From the modelling point of view, the complexity is given by the limited knowledge about the mechanical behaviour of the complex formation due to the lithological and structural heterogeneity. In some cases, the geological and modelling complexity can be overcome by adopting simplified constitutive models, which allows to describe in an appropriate way the real behaviour. The presence of blocks, although with different motivations, can lead to greater complexity from the engineering point of view. In fact, in the execution phase it can be difficult to penetrate material much more resistant than the one considered in design phase. It is therefore not possible to simplify the problem considering only the matrix behaviour, which represents the weak portion, but it is necessary to consider the presence of blocks, going to model a more complex configuration. This type of situation requires a more complex project to take into account this problem. Engineering complexity may also affect formations in which the geology and mechanical characteristics of the deposit are known. During the construction of engineering works involving materials as mélange, there are several critical factors to consider in defining the techniques and more appropriate method of excavation: the characteristics of the blocks, such as size distribution, volumetric percentage, lithology, and shear strenght. Moreover, the stress state within the mélanges, on which depends the behaviour of the material during the construction phase, is influenced by lithology, particle size distribution, orientation, and shape of blocks (Medley et al., 2004). Other important factors which must be considered are the characteristics of the matrix, such as shear strenght parameters and the orientation of the shear surfaces, and the hydrogeological configuration of the site. The aquifer has an important impact on stresses and mechanical properties. In mélanges, permeability may vary of different orders of magnitude in a short distance. This characteristic depends on the presence of intact blocks, fractured blocks and matrix which may have different permeability. Therefore, it’s easy to imagine that even if the mechanical characteristics of the materials constituting the mélange are known, the definition of interface behaviour between block and matrix results extremely complex (Medley et al., 2011).

This is another reason why the great simplification generally done by assimilating the natural material to a soil composed only of homogenous matrix may have adverse consequences in execution phase.

1.2.4 In-situ sampling

The hydrogeological and geotechnical characterization of a complex block-in-matrix formation is fundamental, since the presence of blocks and their distribution influence permeability, shear strenght and choice of engineering construction methods. The most used technology today for better understand the non-visible geomechanics composition of a soil or rock mass is the geognostic survey which is performed by the surface. Through this survey, information concerning physical properties, lithology, mineralogy, hydrology, and structural characteristics in relation to sampling depth can be obtained. One of the aims of the in-situ investigations is to obtain and determine the placement of rocky inclusions in the formation of interest. The extraction of a loose sandy material is difficult, since its geotechnical properties are lost, in a similar way, in the case of a survey inside a bimrock material, the samples do not remain undisturbed: this behaviour is due to the degree of alteration induced by the core in the area of contact between blocks and matrix, because the different mechanical strength of the two materials makes the cutting phases more difficult. During core drilling, the samples are disturbed to a certain degree, and the contrast between the blocks and the matrix has a considerable impact on the quality of the test samples, since the shear strenght contrast leads to difficulties in the carving and extraction phase. Even if the procedure of extraction and carving of the test sample has been carried out in the best possible way, the test, in almost all cases, could not be representative of complex formation of interest (Lindquist, 1994).

In the case under examination, it was very difficult to take an undisturbed sample of sedimentary Oltrepò Pavese mélange with the standard coring methods because it was very difficult to extract it from the drilling bit due to the clay matrix and also due to the use of water which could have destroyed the matrix tissue. In addition, in previous extractions, a dry drilling was attempted. However, some problems emerged during the extraction of the material from the die. In fact, it was completely stuck, and a hammer was used inevitably destroying the sample. Moreover, it was not possible to reach the area with an excavator, so it was not possible to dig. For these reasons, the samples were manually collected using a chisel and hammer (Figure 5). A surface layer of a few centimetres was removed initially in which there was damaged material from the atmospheric agents. Then, by sticking the chisel in the material and using a hammer, some pieces with a length of the order of few decimetres were extracted (Cerise, 2019). The samples of mélanges taken were then wrapped in newsprint and sealed with paper scotch. This technique has proven effective for good preservation of the material.

Figure 5: Extraction of a Oltrepò Pavese mélange sample (highlighted in red) using hammer and chisel (Cerise, 2019).

1.2.5 Laboratory characterization

The complex formations are materials with considerable difficulty in manufacturing representative specimens at engineering scale. Such difficulties lead to further complications in the design phase and in the execution phase of the engineering work. In this thesis, important critical issues arise from the fact that the Oltrepò Pavese mélange analyzed is in an intermediate position between soil and rock, therefore both the theories of soil mechanics and of rock mechanics are hardly applicable. The mélange studied, in fact, is rigid and compact, seemingly like a rock, but it is weak if subjected to shear forces or impacts. In addition, the marly matrix of which is compound is soluble in water. These problems prevent the extraction of samples with the most classic techniques. As will be seen in more detail in the following paragraphs, due to these numerous difficulties an unconventional test procedure has been chosen to characterize this mélange, creating a reconstituted material which is first consolidated through a consolidometer and then tested by triaxial test to determine its failure criterion, strength, and deformability parameters.

1.3 Characteristic engineering dimension L_c

The *characteristic engineering dimension* L_c of the problem, also called characteristic length, is defined as the length of an element of the engineering model that is representative of the geometry of the problem under consideration (Medley et al., 1994). It represents the dimensional threshold that divides the blocks from the fragments of rock believed to be part of the matrix (Medley, 2001). Depending on this length, therefore, it is possible to define a size range within which the size of the blocks is considered significant. The choice of the engineering size is made, generally, with ample flexibility, always considering the design problem under examination. More specifically, the characteristic length depends on the scale of interest and the size of the engineering work which is, for example, equal to the:

- width of a foundation;
- diameter of a tunnel;
- area of the site under investigation;
- slope height.

In the case of laboratory tests, L_c coincides with a size of the test sample, generally with the diameter. If instead you want to analyse a surface covered by shooting photographic or thematic papers, the characteristic length is equivalent to A, where A corresponds to the test area. As mentioned at the beginning of the paragraph, this size is crucial for the determination of the threshold between blocks and matrix. Medley in 1994 established that blocks larger than 5% of the characteristic length L_c can be considered significant for the geotechnical interest according to the scale of reference. Moreover, he defined that with blocks larger than 75% of L_c, the formation can no longer be considered as a mélange, but as a rock mass. Below there is a description of an example proposed by Medley in 2001, in which an area of study A was considered entirely consisting of Franciscan Mélange.

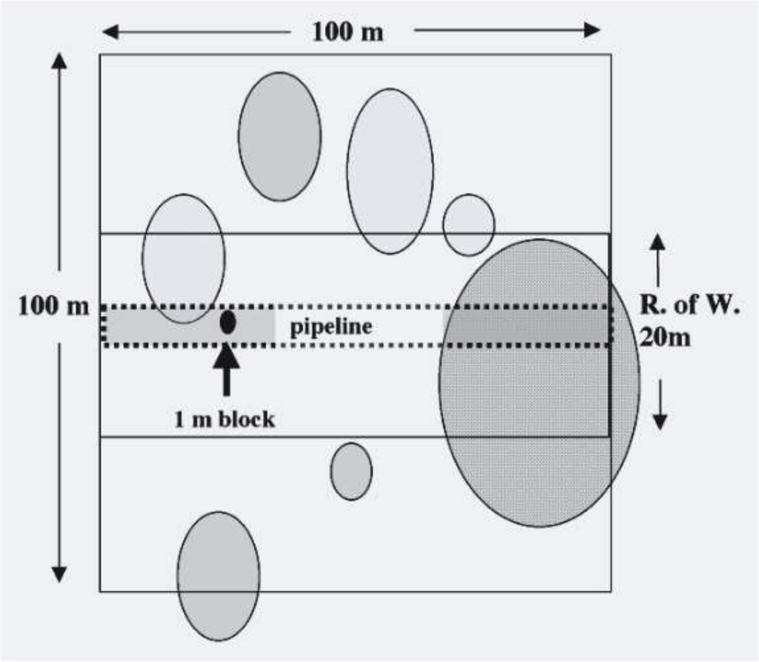

Figure 6: Example demonstrating the influence of block size on the scale of interest: the black block of size of 1 m considerably influences the implementation of a pipeline represented with the dotted line, while it is considered as part of the matrix if you consider the entire area of 100 x 100 m^2 (Medley, 2001).

The example showed in Figure 6 helps to notice the effect of the scale of the problem on the block/matrix threshold. As can be observed, the total area of study A was represented proposing a scheme in which are shown various scale relative to a road and to a trench excavated for the pipeline installation. The road is 20 m wide while the trench is 2 m wide and deep. Considering this, it is possible to make some considerations. Initially, an area A of size 100 x 100 m is considered in which the Franciscan Mélange is present. In this case, the characteristic length L_c is equivalent to square root of the area A, then equal to 100 m. The limit between blocks and matrix is $0.05 \cdot L_c$ equal to 5 meters, while the maximum size of a block is equal to $0{,}75 \cdot L_c$ then equal to 75 m. In this case, it is interesting to note that the black block of 1 m size located in the central part of the total area is part of the matrix. Looking at the scale of the road, the characteristic engineering dimension L_c is 20 m; the threshold between blocks and matrix, equal to $0.05 \cdot L_c$, is now equal to 1 m; the maximum size of the block can be considered equal to $0,75 \cdot L_c$ therefore, equal to 15 m. Finally, considering the scale of the trench, the L_c corresponds to the depth of the excavation which is equal to 2 m; in the same way as the previous case, the limit between blocks and matrix and the largest block size is obtained equal to 0.1 and 1.5 m respectively. This means that the black block of 1 m size, present in the central part of Figure 6, is considered to belong to the blocks and no longer to the matrix, both in this case and in the previous one. In conclusion in this case study, proposed by Medley in 2001, it is clear how important the scale of reference of the problem under consideration is and how fundamental, although flexible and relatively arbitrary, the choice of the characteristic engineering dimension L_c is.

1.4 Mechanical behaviour of a structurally complex formation

The structurally complex formations such as mélanges or more generally bimrocks are those geological bodies, which contain blocks immersed in a matrix with a chaotic and heterogeneous structure in which it is possible to find an important variability of the mechanic characteristics of the elements that compose them. This leads to significant problems in the phase of characterisation and definition of shear strenght parameters. A geological body can be classified as bimrock if it meets some fundamental properties:

- the volumetric blocks proportion (VBP) must be between 5% and 75%, according to the studies proposed by Lindquist in 1994. The VBP expresses the ratio of blocks volume to total mass volume. Below 25 % in fact shear strenght characteristics are controlled by the properties of the matrix. With VBP higher than 75% the behaviour can be assimilated to that of an extremely fractured rock mass. The blocks and matrix elements have a high difference in terms of strength and just this contrast develops shear deformations in the matrix. The weakest element within a mélange is commonly the contact layer between block and matrix, where the failure surfaces generally appear and consequently assume a tortuous shape around the blocks (Medley et al., 2004);

- the threshold value in terms of friction angle φ must be (Eq.1):

$$\frac{\tan \varphi_{\mathrm{blocks}}}{\tan \varphi_{\mathrm{matrix}}} \geq 2 \qquad \text{(Eq.1)}$$

while in terms of Young's modulus E is (Eq.2).

$$\frac{E_{\mathrm{blocks}}}{E_{\mathrm{matrix}}} \geq 2 \qquad \text{(Eq.2)}$$

Moreover, according to the literature (Sonmez et al., 2009) the uniaxial compressive strength (UCS) of blocks and matrix shall be such that (Eq.3):

$$\frac{\mathrm{UCS}_{\mathrm{block}}}{\mathrm{UCS}_{\mathrm{matrix}}} \geq 2 \qquad \text{(Eq.3)}$$

They are threshold values because in presence of minor contrasts the failure surface tends to develop also within the blocks rather than only in the matrix and the mechanical behaviour approaches that of a homogeneous medium (Medley et al., 2011). When the shear strenght contrast exceeds the threshold value the shear strenght of the blocks plays an important role on the mechanical properties of the bimrock. The overall strength of a mélange is directly proportional to the percentage volumetric block (VBP) and is independent of the strength of individual blocks (Lindquist, 1994).

Lindquist (1994) made his first observations on artificial tests simulating behaviour of Franciscan Mélange and based on the results obtained he highlights the increase in shear strenght to the increase in the volumetric content of the blocks (VBP).

1.4.1 Lindquist's experimental study (1994)

Lindquist, starting from the observations made by Medley et al. in 1994 on the Franciscan mélange, reproduces samples in the laboratory with similar characteristics to be tested to determine their mechanical behaviour at failure. He made more than one hundred samples. He performed triaxial tests on cylindrical samples with a diameter of 150 mm and a height of 300 mm. Portland cement with bentonite was chosen as the main material that forms the matrix. While to simulate the shear surfaces present inside, wax layers were introduced inside as plans of weakness; in addition, to reduce excessive friction between the materials, the layers were coated with talc. The blocks were instead made with sand, fly ash, cement, and water (Figure 7).

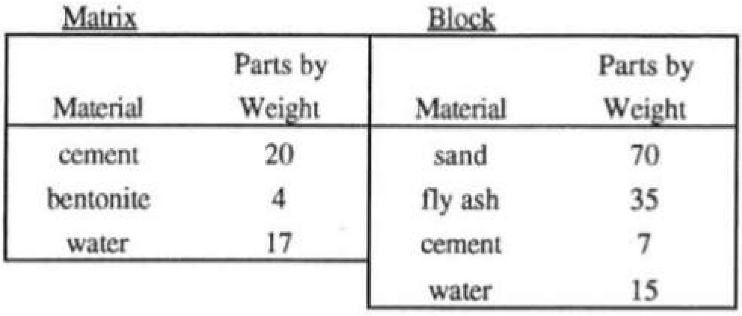

Matrix		Block	
Material	Parts by Weight	Material	Parts by Weight
cement	20	sand	70
bentonite	4	fly ash	35
water	17	cement	7
		water	15

Figure 7: Weights of the elements forming the matrix and blocks (Lindquist, 1994).

Three volumetric blocks proportion (VBP) were considered: 30%, 50%,70% with the following orientation of the elliptical inclusions with respect the horizontal plane: 0°, 30°, 60°, 90°. He therefore realized 5 samples for each of the 4 models represented schematically in the first four squares on the left as shown in Figure 8. In addition, to characterize the matrix and blocks, he prepared 7 samples of 200 mm diameter consisting of matrix only and 10 samples of 70 mm diameter of only material used to make blocks. In total, also considering the trial mixtures made to define the model, more than 180 specimens were produced.

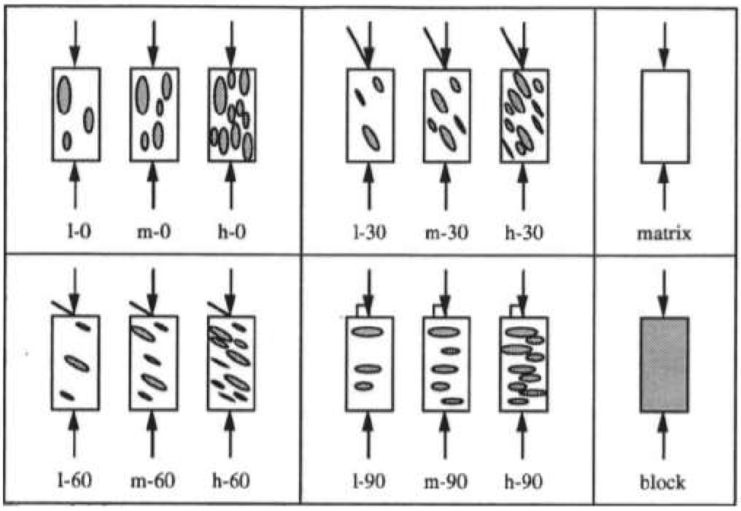

Figure 8: Rappresentazione grafica dei modelli fisici impiegati per la determinazione delle caratteristiche (Lindquist, 1994).

The various elements are subjected to triaxial tests to measure the change in mechanical properties as a function of the different percentage volumetric of the blocks and their orientation. After performing triaxial tests, he decided to interpret the experimental results with the linear failure criterion defined by Mohr-Coulomb (Eq.4):

$$\tau = c' + \sigma' \cdot \tan \varphi' \qquad \text{(Eq.4)}$$

where τ represents shear stress, c' is the effective cohesion, σ' is the normal stress and φ' is the internal friction angle of the material. Lindquist made the following observations:

- the modulus of deformation is greater in the samples with higher VBP values;
- the modulus of deformation assumes higher values when the load is applied parallel to the orientation of the blocks;
- increasing the VBP there was an increase of the internal friction angle of 15°-20° with respect to that of the matrix only (Figure 9). The increase is due to the increase in the tortuosity of the failure surface;
- an increase in the VBP implies a cohesion reduction due to poor interface properties around edges of the blocks where the deformations develop; the lowest values of cohesion were recorded in the case of inclination of the blocks of 30° with respect to the direction of load application (Figure 10);
- samples with a VBP of about 25-30% showed values of cohesion and internal friction angle almost equal to those of the matrix, while those with VBP above 70% had values like those of blocks. Based on these observations, it was argued that the blocks do not affect the mechanical shear strenght of the heterogeneous material for VBP values less than 25-30%, while for VBP values above 70%, the contribution to the shear strenght offered by the matrix is negligible and the material can be considered as a single block.

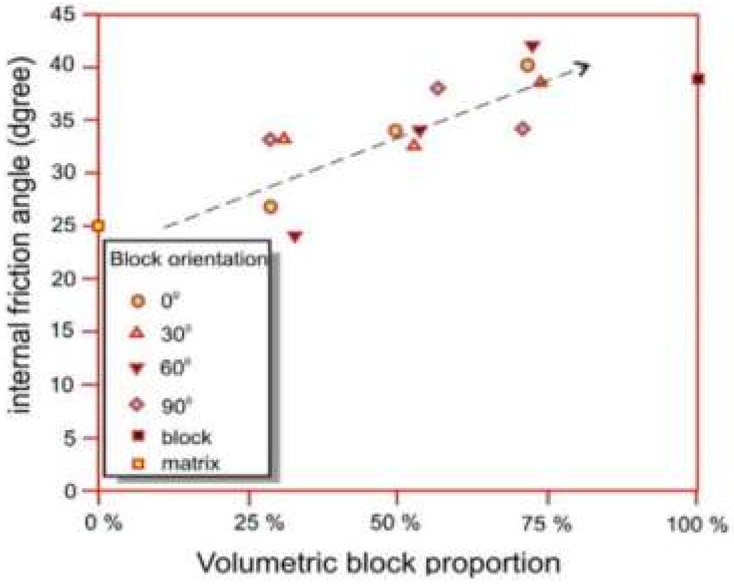

Figure 9: Variation of the internal friction angle for the different VBP and for different block orientations with respect to the application of the maximum load (Lindquist, 1994).

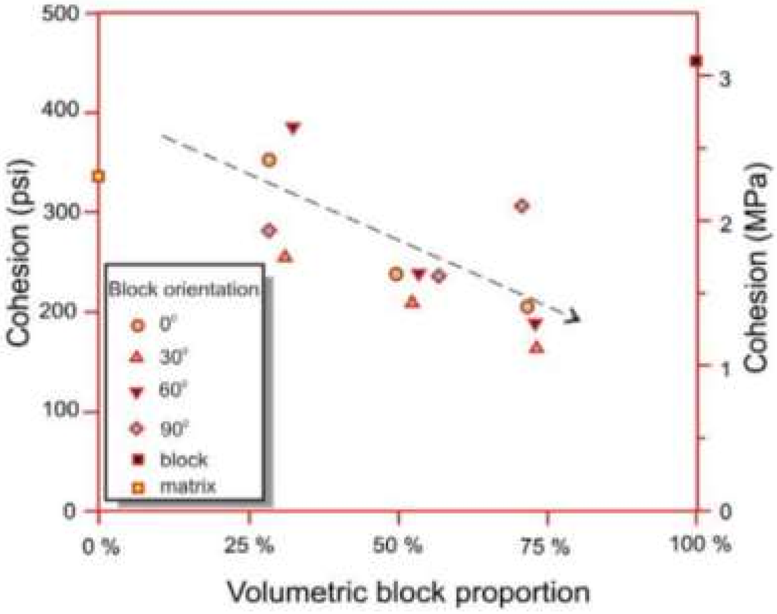

Figure 10: Variation in cohesion for different VBP and for different block orientations with respect to the application of the maximum load (Lindquist, 1994).

Based on triaxial test results obtained, Lindquist proposes a change to the Mohr-Coulomb failure criterion introducing the effect of VBP (Eq.5), in order to provide a failure criterion by considering the complex material as a homogeneous equivalent material:

$$\tau_{\mathrm{bimrock}} = c_{\mathrm{matrix}} \cdot (1 - \mathrm{VBP}) + \sigma \cdot \tan(\varphi_{\mathrm{matrix}} + \Delta\varphi(\mathrm{VBP})) \qquad \text{(Eq.5)}$$

where $\Delta\varphi(\mathrm{VBP})$ represents the increase of the internal friction angle as the VBP increases and, for VBP values greater than 25%, it undergoes an increment equal to 3° for every increment of the VBP of 10%. It is important to notice that the (Eq.5) reflects the results obtained from triaxial tests: cohesion decreases as the VBP increases, while the friction angle increases. The assumption of this criterion, as shown by subsequent studies (Irfan et al., 1993) is a conservative choice.

1.4.2 Sonmez et al. experimental study (2006)

Sonmez et al. (2006) have tried to develop empirical equations that describe the strength parameters of a complex material such as bimrock based on data obtained from uniaxial compression tests (UCS) and triaxial tests on samples artificially prepared in laboratory. Plaster of Paris, bentonite, cement, and water were mixed with different quantities to obtain matrix with various strength. Moreover, tuff and andesite were fragmented to centimeter sizes to produce blocks. These blocks were then mixed with the various matrixes to create artificial bimrock samples and to imitate the presence of inclusions inside the material (Figure 11).

Figure 11: Stages of preparation of artificial bimrock samples (Sonmez et al., 2006).

The UCS and triaxial test were previously conducted on matrix only samples, to get proper mixture ratios to be used in the preparation of artificial bimrock, and then on artificial bimrock samples having different VBP. Triaxial tests were carried out under cell pressures of 75 kPa, 100 kPa, 150 kPa and 300 kPa to obtain the failure envelopes. After all these tests, a statistical analysis was carried out and a relationship has been found between the strength parameters of blocks inserted in the samples and the value of global uniaxial compressive strength (UCS), according to different VBP. In this way, it was possible to define Mohr-Coulomb strength parameters (c and φ) and Hoek & Brown strength parameter (m_i) formulating the following empirical equations, respectively in Table 1 and Table 2, normalized with respect to the matrix parameters.

Table 1: Mohr-Coulomb empirical equations normalized with respect to the matrix parameters (Sonmez et al., 2006).

$\mathrm{c_N} = 1.25 - \exp\left(\frac{\mathrm{VBP} - 100}{75}\right)$	$\mathrm{c_{bimrock}} = \mathrm{c_N x c_{matrix}}$
$\varphi_\mathrm{N} = \exp\left(\frac{\mathrm{8xVBP}}{1000}\right)$	$\varphi_\mathrm{bimrock} = \varphi_\mathrm{N} \mathrm{x} \varphi_\mathrm{matrix}$
$\mathrm{UCS_N} = 1 - \exp\left(\frac{\mathrm{VBP} - 100}{25}\right)$	$\mathrm{UCS_{bimrock}} = \mathrm{UCS_N x UCS_{matrix}}$
$\mathrm{UCS_{bimrock}} = \frac{2\mathrm{c} \cos \varphi_\mathrm{bimrock}}{1 - \sin \varphi_\mathrm{bimrock}}$	$\sigma_1 = \mathrm{UCS_{bimrock}} + \left(\frac{1 + \sin \varphi}{1 - \sin \varphi}\right) \sigma_3$

Table 2: Hoek & Brown empirical equations normalized with respect to the matrix parameters (Sonmez et al., 2006).

$\mathrm{m_{i\_N}} = \exp(0.015\mathrm{xVBP})$	$\mathrm{m_{i\_bimrock}} = \mathrm{m_{i\_N} x m_{i\_matrix}}$
$\sigma_1 = \sigma_3 + \mathrm{UCS_{bimrock}} \sqrt{\left(\mathrm{m_{bimrock}} \frac{\sigma_3}{\mathrm{UCS_{bimrock}}} + 1\right)}$	

Where c and φ represent respectively the cohesion and internal friction angle, UCS the uniaxial compressive strength, m_i is the value of the Hoek-Brown constant for an intact rock, σ_1 and σ_3 are major and minor principal stresses.

The authors also tried to evaluate the reliability of proposed equations, recalculating the value of the principal vertical stress σ_1 and comparing it with that obtained during the measurement of the tests performed, expressing their differentiation through a percentage error called error ratio (Eq.6).

$$\text{Error ratio}(\%) = \left(\frac{\text{derived } \sigma_1 - \text{measured } \sigma_1}{\text{measured } \sigma_1}\right) \cdot 100 \qquad \text{(Eq.6)}$$

As shown in Figure 12*,* using the Hoek & Brown and Mohr-coulomb approaches it was obtained respectively that the 73% and 65% of the data have an error ratio less than 3%. Therefore, Sonmez et al. (2006) affirmed that the empirical approach based on the Hoek & Brown empirical equations provides slightly better results in terms of reliability than the empirical approach based on the Mohr-Coulomb empirical equations.

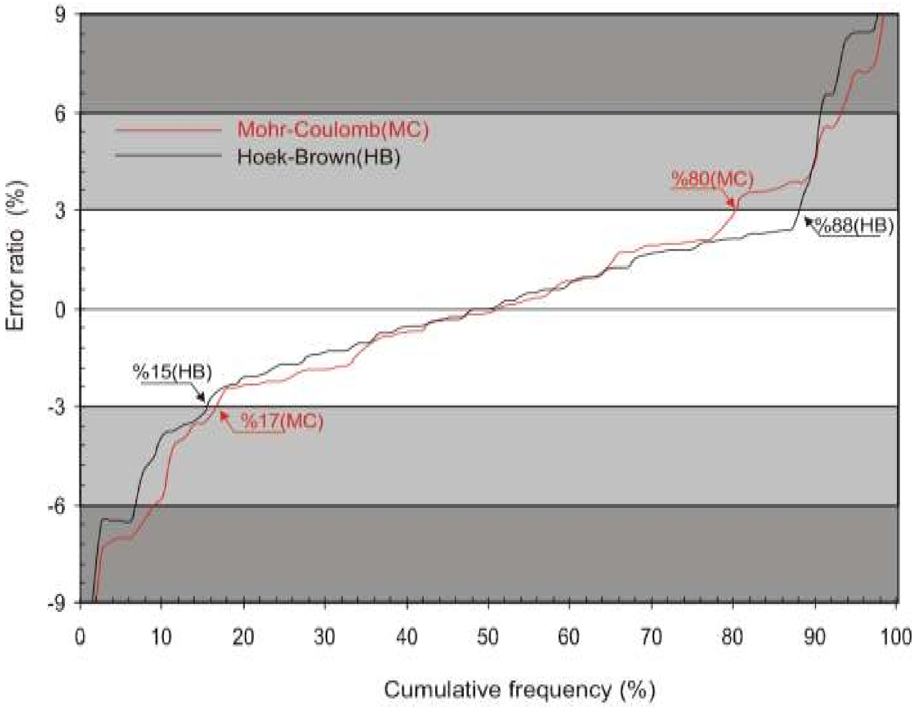

Figure 12: Cumulative frequency of error ratio, obtained using the values of σ_1 evaluated with the empirical solutions found from Mohr-Coulomb and Hoek & Brown equations (Sonmez et al., 2006).

1.4.3 Zhang et al. experimental study (2016)

Zhang et al. (2016) in their study performed a series of triaxial tests on three types of soil-rock mixture (S-RM) remoulded samples with the same rock block content, but different grain size distributions. Moreover, further triaxial tests were carried out on a set of soil samples with grains smaller than 5 mm to clearly highlight their distinct mechanical properties with respect to a soil-rock mixture. A S-RM is composed of large size "rock block" pieces with high strength and small-size "soil" with low strength (Zhang et al., 2016). The physical and mechanical properties of S-RM are affected by the presence of rock blocks, especially when the rock block content is high enough to create many interactions between the rock blocks, which will control the mechanical behaviour of the mixture. In this study, consolidated undrained triaxial tests were performed with the aim to better understand the S-RM meso-mechanical characteristics such as the shape, the distribution, the adjustment of the internal rock blocks and the influence that they have on the S-RM mechanical properties.

In agreement with Medley et al. (1994), the soil/rock threshold used in this study was set at $0.05L_c$, where L_c is the characteristic length of the problem which in this case is the diameter of the triaxial sample. The diameter and the height of the triaxial sample were respectively equal to 100 mm and 200 mm, therefore a soil/rock threshold of 5 mm was selected. This means that any particle greater than 5 mm in size was considered as a "rock block" instead particle less than 5 mm in size was considered as a "soil".

The maximum grain size in two different sets of S-RM samples, called S-RM-2 and S-RM-3, was supposed to be one fifth of the sample diameter, i.e., 20 mm. Furthermore, a set of SR-M unconventional samples, called S-RM-1, containing "oversized rock blocks" were prepared. The size of the maximum grain size of these unconventional samples was fixed at 60 mm to highlight the important role and impact of large rock blocks on the SR-M mechanical properties. In total, one set of soil samples and three sets of SR-M samples were obtained, each of them with the same rock blocks content of 50% but with different grain size distribution (Figure 13).

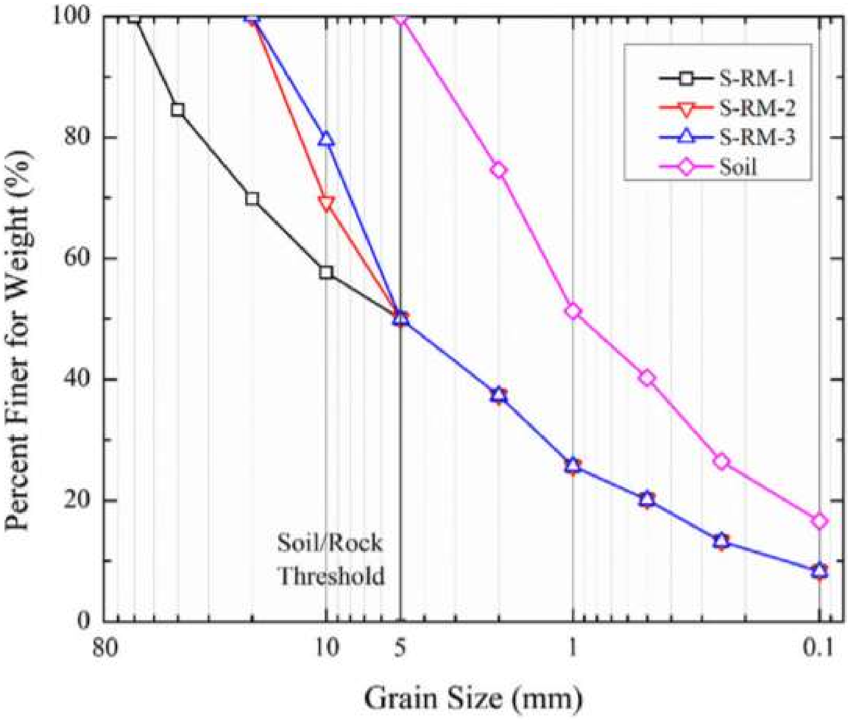

Figure 13: Grading curves of the four types of samples used for the triaxial tests (Zhang et al., 2016).

Based on these triaxial tests, performed with a confining pressure equal to 100 kPa, 300 kPa, 600 kPa, 900 kPa and using the X-ray computed tomography (CT) was possible to evaluate the effect of particle size distribution on the mechanical properties and meso-structural evolution of the S-RMs. The X-ray CT is a non-destructive technique helpful for visualizing and measuring the changes in the internal structure of the sample during the loading phase. All samples were loaded until the axial strain exceeded 20%. Zhang et al. (2016) in their study used a CT triaxial apparatus which has the same working principle of a standard triaxial apparatus, but it lies on the scan bed of the CT machine to enter in the scanning tube (Figure 14).

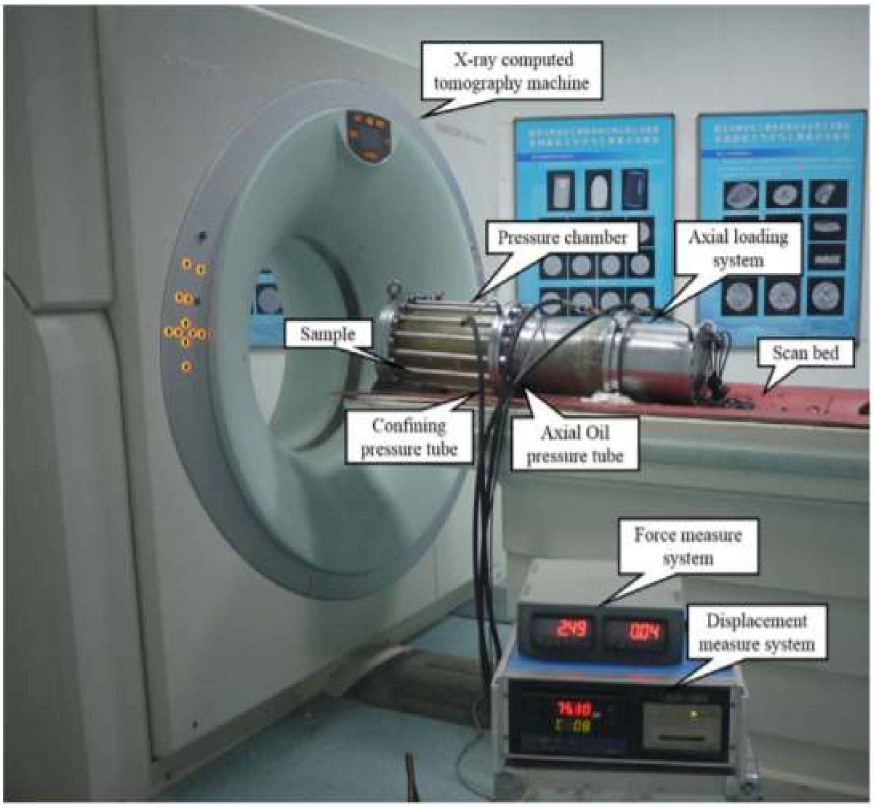

Figure 14: CT triaxial apparatus and workstations (Zhang et al., 2016).

Each sample were scanned before and after the tests. Moreover, some immediate CT scans of the sample at every 5% increase in axial strain, under a confining pressure of 600 kPa for each type of sample, were carried out to obtain the immediate CT images during the triaxial test. Through the analysis of the CT images, it was possible to visualize the 3D structure of the different soil-rock mixtures and the interaction between the internal rock blocks (Figure 15).

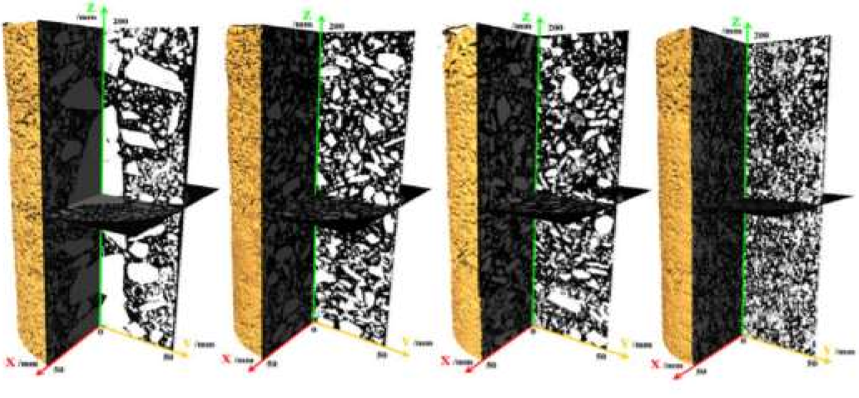

Figure 15: 3D CT images of the four types of samples (Zhang et al., 2016).

On this basis, Zhang et al. (2016) analysed the effect of the grain size distribution on the mechanical properties of the S-RM. They drew the Mohr circles under different confining pressures to obtain the strenght parameters, friction angle and cohesion, of the four types of samples. The results are listed in Figure 16.

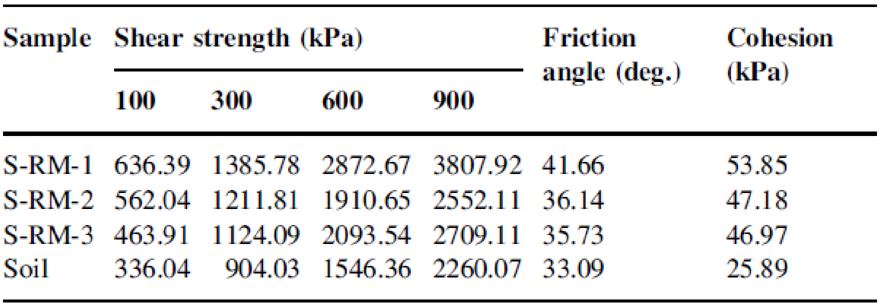

Sample	Shear strength (kPa)				Friction angle (deg.)	Cohesion (kPa)
	100	300	600	900		
S-RM-1	636.39	1385.78	2872.67	3807.92	41.66	53.85
S-RM-2	562.04	1211.81	1910.65	2552.11	36.14	47.18
S-RM-3	463.91	1124.09	2093.54	2709.11	35.73	46.97
Soil	336.04	904.03	1546.36	2260.07	33.09	25.89

Figure 16: Shear strenght parameters of the four types of samples obtained from the triaxial tests at different confining pressures (Zhang et al., 2016).

As can be seen from Figure 16, the sample S-RM-1 has the higher friction angle mainly due to the sliding and interlocking between the particles. Moreover, the occlusion of coarse particles and capillary suction under unsaturated conditions, caused the increase of the cohesion. Therefore, the rock blocks played an important role also in enhancing the cohesion (Zhang et al., 2016). In fact, the test results showed that without the enhancement of the rock blocks, the soil sample had the lowest friction angle and cohesion values. These results allowed the authors to affirm that both the strenght parameters of the three types of S-RM samples increase with the increase in the uniformity coefficient of the grading curve.

2. Tortuous failure surfaces

Because of their peculiarities, bimrocks are characterized by tortuous failure surfaces which strongly influence its mechanical response to different states of stress (Lindquist, 1994). This tortuosity increases as the volume proportion of blocks (VBP) of bimrock increases. Consequently, it is important to analyze both the geometry and characteristics of these surfaces.

2.1 Study on tortuous failure surfaces conducted by Medley (2004)

Medley in 2004 observed that the tortuosity of failure surfaces is more influenced by the shape of the blocks and their orientation. For the slope stability, elliptical blocks have the most harmful effect when the direction of the major axis coincides with the shear. In particular, he focused on the contact between block and matrix because he considers it to be the weakest component of bimrock where the tortuous failure surface might be easier to create.

Medley based his research on experiments conducted by Lindquist (1994), in which it was demonstrated, by cutting some triaxial tested specimens, how in bimrock failure surfaces typically develop around blocks. Lindquist analyzed the failure surfaces of about 60 of these samples. The samples were wrapped in transparent film and the lines of the blocks and failure surfaces were drawn by hand with a marker. The paths were then photocopied as can be seen in the Figure 17. Paths are a 2D projection of cylinders, and as you cansee, there are some horizontal distortions of the blocks (Medley, 2004).

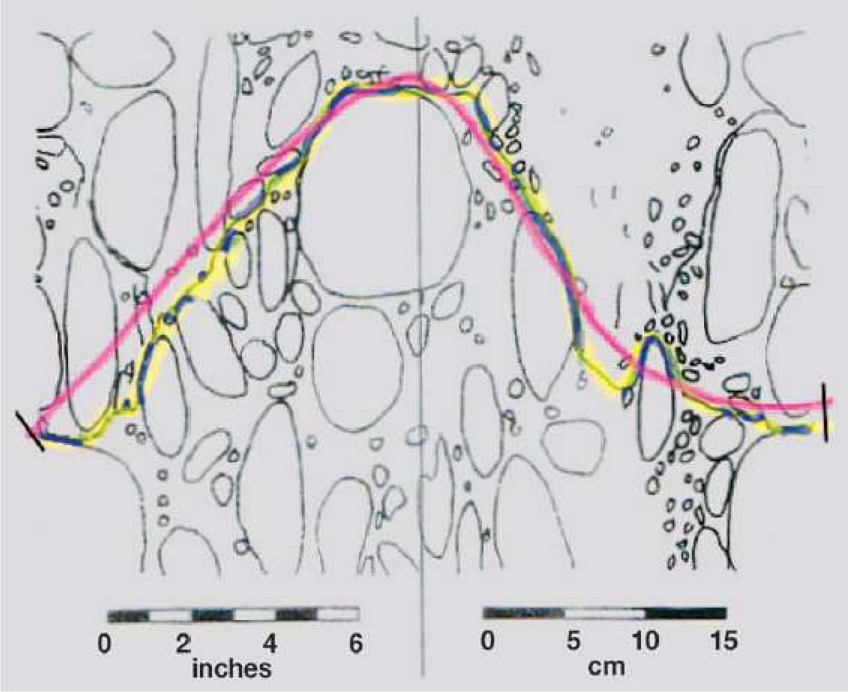

Figure 17: Measurement were made of: a) the length of the breaking tortuous surface (yellow highlighted line), b) the estimated length of the average smooth surface (red line); and c) the total length of the block contacts along the failure surface (Medley, 2004).

Medley (2004) uses the side surface paths of the specimens used by Lindquist in 1994 to study the characteristics of the failure surfaces. The actual failure surface of the specimen is shown in yellow and, to measure it, a flexible chain was placed on the failure line which was later removed, straightened, and measured. The length found was called the *tortuous length L'*, also called *tortuous line*. The red line indicates the failure surface found by Lindquist (1994) on matrix-only specimens. This line was measured manually by the flexible chain and then digitally and was called *smooth line* L_0. Medley (2004), after measuring 73 lines, assumed that the degree of horizontal elongation of the yellow and red lines was the same. In addition, the block/matrix contact lengths (blue lines) along the failure surface were measured and summed to obtain a *total contact length* indicated with *t*. Finally, the samples were grouped by volumetric proportion and block orientation and the tortuous failure lines were drawn manually as shown in Figure 18. It is possible to observe the pronounced irregularity of the trajectories. Medley (2004) has compared six standard enlarged profiles of rock mass joints to these tortuous failure lines. The standard rock mass joints profiles have been enlarged and used to define JRC roughness coefficients from 10 to 20 (Barton et al., 1977). These six standard profiles result less irregular with respect the tortuous failure surfaces.

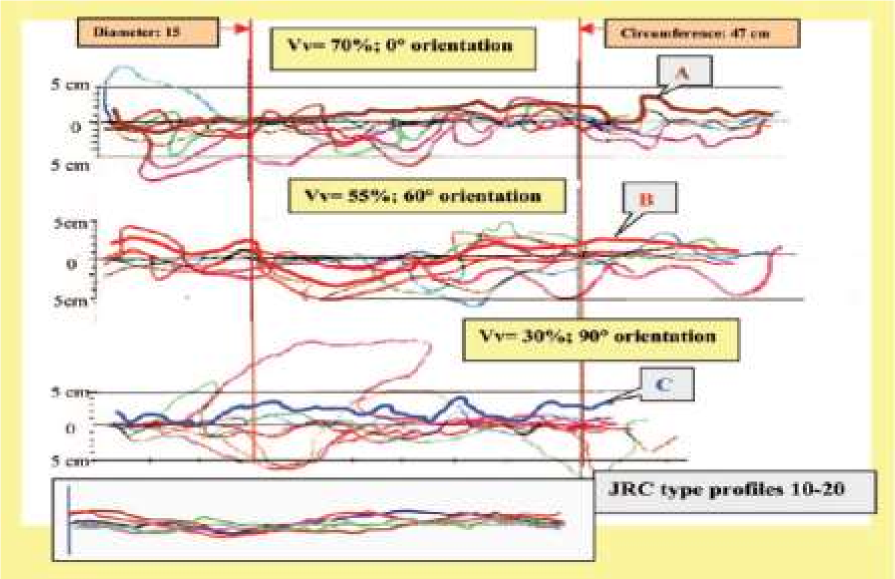

Figure 18: Scans of traced lines of failure surfaces and compared to type profiles for JRC 10 to 20 (Barton et al., 1977).

Medley (2004) defined the ratio between *L',* and L_0 as a measure of tortuosity. This ratio L'/L_0 was called *tortuous length ratio*. The areas A under the irregular tortuous failure lines were measured digitally using an image analysis software called SigmaScanPro (Medley, 2004). In addition, he defined a measure of the potential failure zone as the average width of possible tortuous failure surfaces. The *average tortuous width* or ("superficial roughness") is obtained by dividing the total area *A*, contained between the irregular tortuous line and the smooth line by the length of the smooth line L_0 (Figure 19). L_0 in this case is the one measured digitally and not by hand like the one described above.

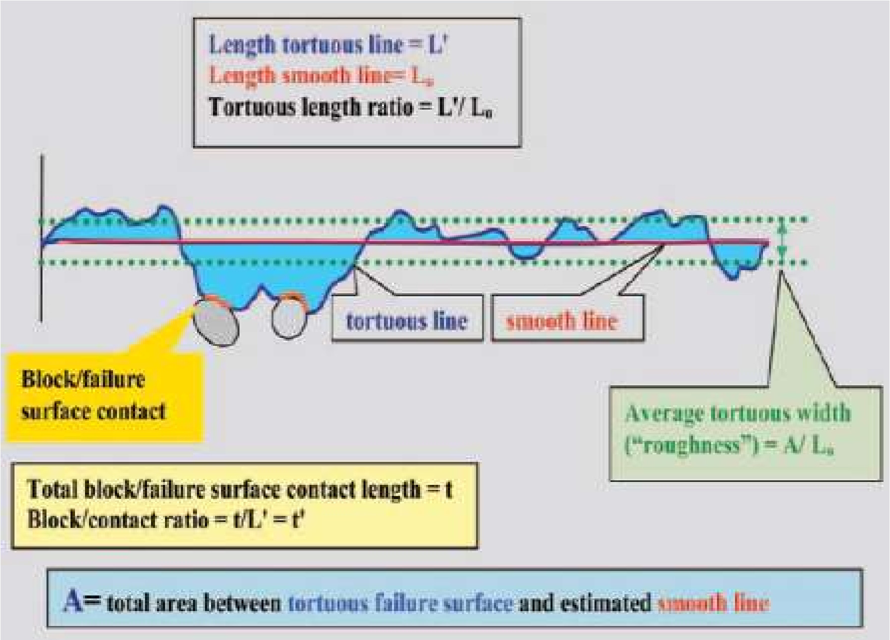

Figure 19: Parameters measured and calculated from traced lines of tortuous failure surfaces (Medley, 2004).

As can be seen in Table 3 the average width value of the 73 tortuous failure surfaces, starting from the samples used by Lindquist (1994), is 1.44 cm with a standard deviation of 0.68 cm. Finally, knowing that the diameter of the samples subjected to triaxial test is 15 cm, the average width of the tortuous failure surface is about 10% of the diameter to which must be added a standard deviation equal to +5% and -5%.

Therefore, by defining as a characteristic engineering dimension (or characteristic length) L_c the diameter of the samples analyzed operating triaxial tests (Medley, 2001; Medley et al., 1994), it can be said that the thickness of the potential failure zone can vary between 5% and 15% of the characteristic length L_c.

Table 3: Summary of the values obtained from Medley's experiments (Medley, 2004).

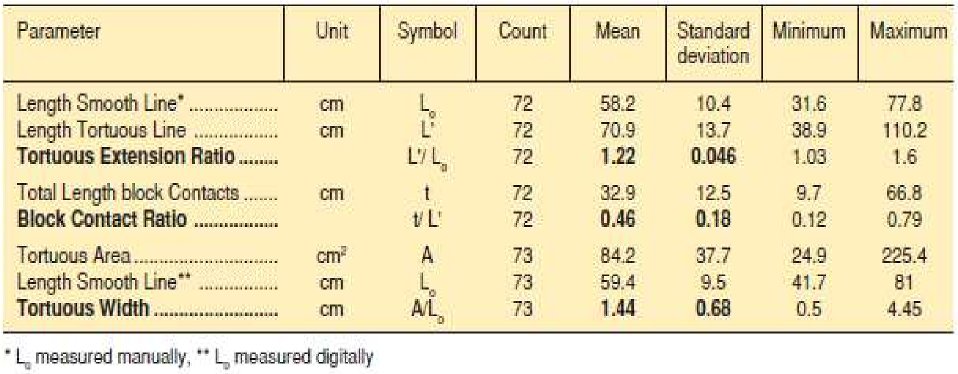

Parameter	Unit	Symbol	Count	Mean	Standard deviation	Minimum	Maximum
Length Smooth Line*	cm	L_o	72	58.2	10.4	31.6	77.8
Length Tortuous Line	cm	L'	72	70.9	13.7	38.9	110.2
Tortuous Extension Ratio		L'/L_o	72	**1.22**	**0.046**	1.03	1.6
Total Length block Contacts	cm	t	72	32.9	12.5	9.7	66.8
Block Contact Ratio		t/L'	72	**0.46**	**0.18**	0.12	0.79
Tortuous Area	cm^2	A	73	84.2	37.7	24.9	225.4
Length Smooth Line**	cm	L_o	73	59.4	9.5	41.7	81
Tortuous Width	cm	A/L_o	73	**1.44**	**0.68**	0.5	4.45

* L_o measured manually, ** L_o measured digitally

2.2 Study on tortuous failure surfaces conducted by Montoya-Araque et al. (2020)

Montoya-Araque et al. (2020) have created a theoretical model to determine the optimal path of the tortuous failure surface (TFS) in a bimslope, which is a slope composed of bimrocks or bimsoils. The theoretical model is based on the use of a grid graph in accordance with the study done by Montoya-Araque et al. in 2019. As can be seen in Figure 20, the bimslope boundary is a polygon with an irregular shape, but its structure is a rectangular arrangement of square cells which are vertically and horizontally aligned. The bimslope matrix is represented by gray cells that contain information about unit weight and strength parameters, instead bimslope blocks are represented by black cells that contain information only about unit weight and not about strength parameters because as defined by Lindquist (1994) the tortuous failure surface in bimrock does not pass through blocks but passes around them. The white cells represent the space outside the slope boundary and contains only information to avoid these cells to be selected during the automatic tortuous failure surface definition. Moreover, it is important to know that the bimslope blocks are randomly distributed with a binomial distribution.

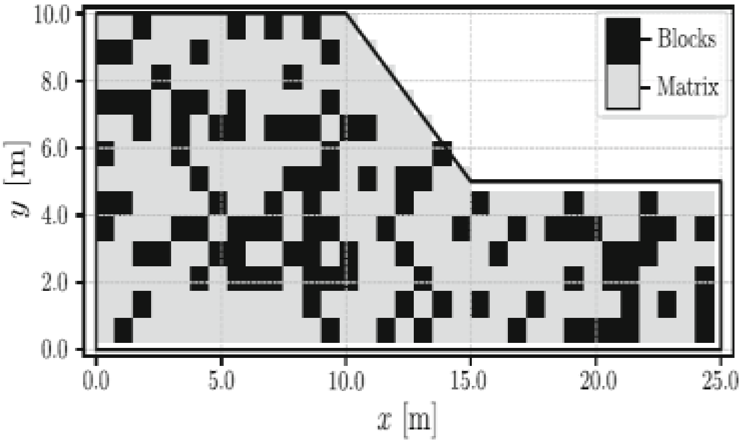

Figure 20: The most basic bimslope model (Montoya-Araque et al., 2020).

The model represented in Figure 20 is used as starting point to create a more sophisticated bimslope model with circular blocks of different sizes. The circular blocks are composed by tiny cells that increase the bimslope resolution making it more accurate. The A* algorithm, described by Montoya-Araque et al. in 2019, generates the circular blocks with different diameters which fill each triangle of the triangular mesh that is contained in the polygon of the bimslope boundary (Figure 21).

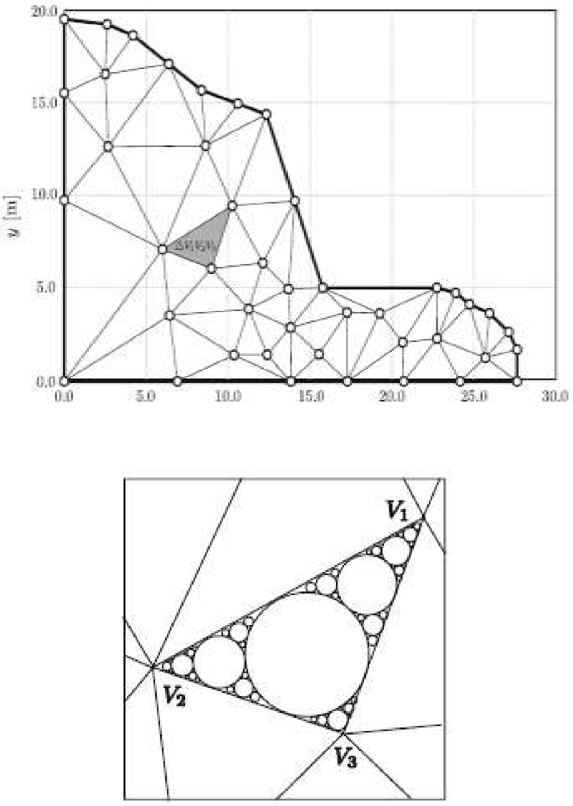

Figure 21: Triangular mesh inside the polygon of the bimslope boundary with each triangle filled with circular blocks of different sizes (Montoya-Araque et al., 2020).

When the circles are all packed in the triangle, a random selection and a shortening of the radii is performed to control the areal block proportion (ABP) assuming equivalence to the volumetric block proportion (VBP) (Montoya-Araque, et al., 2020). In Figure 22 is shown the final bimslope model obtained following the procedure mentioned above.

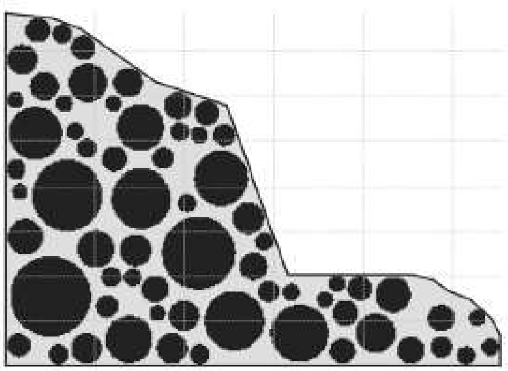

Figure 22: Bimslope model with circular blocks of different sizes (Montoya-Araque et al., 2020).

Montoya and Suarez used pyBIMstab software to perform slope stability analysis evaluating almost one hundred thousand models. This software, developed by them, applies the GLE (General Limit Equilibrium) procedure to any shape of failure surface and automatically generates tortuous failure surfaces (TFS) (Montoya-Araque et al., 2018). It uses the 2D limit equilibrium method (LEM) of Bishop to perform the stability evaluation and to consider the irregular shape of the tortuous failure surface that is created inside the bimslope. The pyBIMstab software uses the optimal path finding algorithm A* that was modified by Montoya-Araque et al. in 2019 to trace optimal paths conditioned to follow a preferred path. This modified A* algorithm can model bimsoils/bimrocks in such a way to develop the optimal path of the tortuous failure surface in the matrix passing around the blocks. The preferred path that the researchers have chosen as input to obtain a more realistic TFS was the matrix-only circular failure surface. This automatic procedure allows to obtain an optimal TFS avoiding the subjectivity problems that appear when the TFSs are traced manually (Montoya-Araque and Suarez-Burgoa, 2018). As we can notice in Figure 23, it' s assumed that the starting and arrival points of the matrix-only circular failure surface coincide with the starting and arrival points of tortuous failure surface of the heterogeneous material.

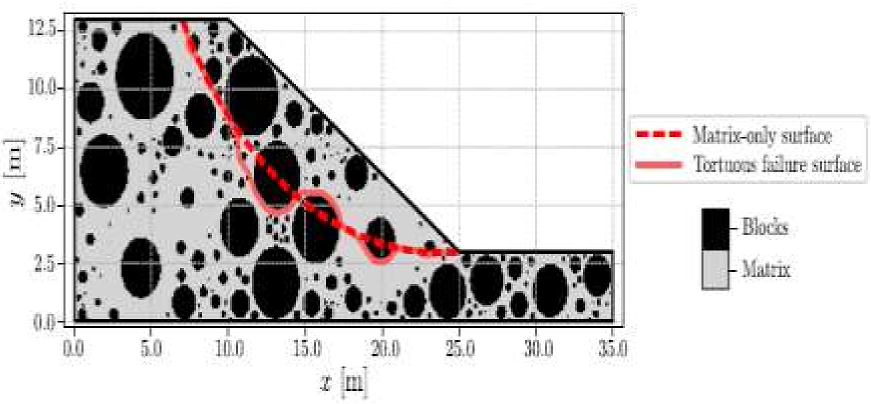

Figure 23: Matrix-only circular failure surface and Tortuous failure surface inside a bimslope (Montoya-Araque et al., 2020).

The TFS found allows to find the parameters already used by Medley (2004) to define the tortuosity. These parameters are the *tortuous length ratio* (TLR), which is the ratio of the length of the tortuous failure surface l_{TFS} to the lenght of the matrix- only failure surface l_{MOS}, and the *average tortuous width* (ATW) which is the light-gray area A_{TFS} in Figure 24 divided by the lenght l_{MOS}. As ATW increases even the tortuosity increases (Montoya-Araque et al., 2020).

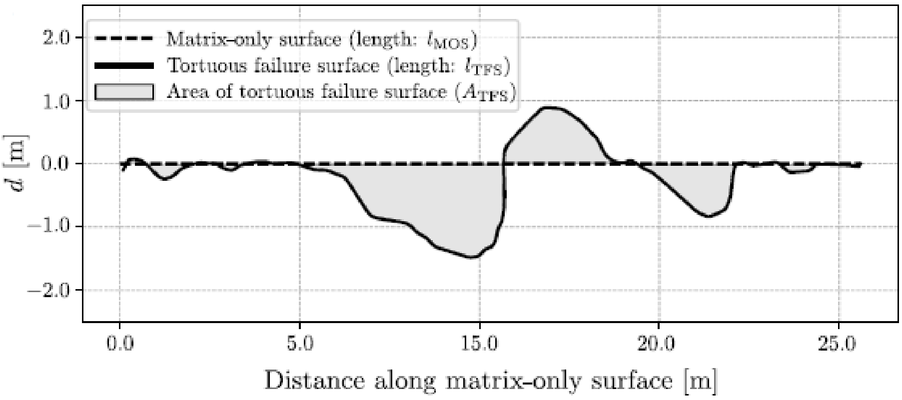

Figure 24: Profile of the Tortuous failure surface lenght along the straightened Matrix-only failure surface length (Montoya-Araque et al., 2020).

As can be seen in Figure 24, the researchers assume also in this representation that the starting and arrival points of the matrix-only circular failure surface coincides with the starting and arrival points of tortuous failure surface of the heterogeneous material.

Moreover, Montoya et al. (2020) as Medley (2004) assessed the *failure zone width* which is the range that contains most of the possible tortuous failure surfaces. They, assuming as characteristic engineering length L_c the height of the slope s_h, have found a failure zone width that is approximately 0.4* s_h because the results of the studies carried out show that most of the possible tortuous failure surfaces are between -2 and 2m deep (Figure 25).

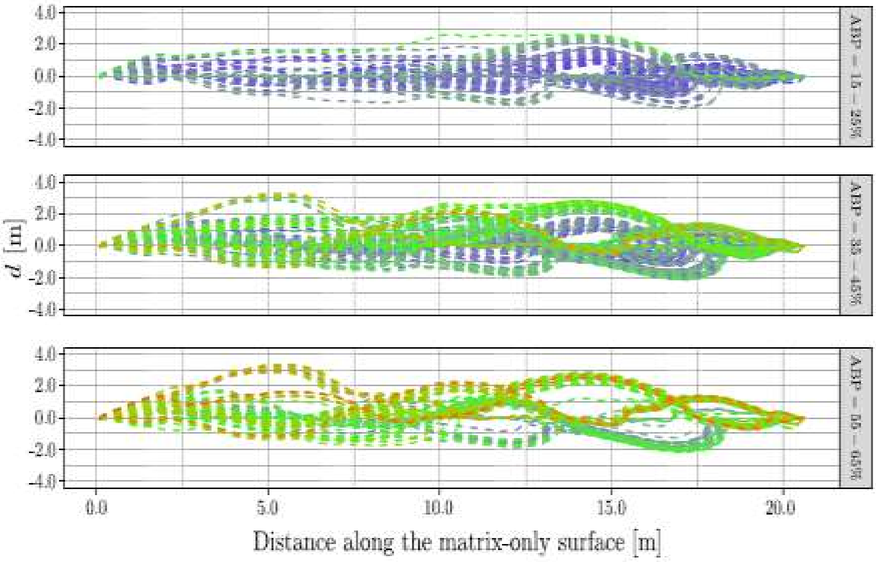

Figure 25: Possible Tortuous failure surfaces profiles for different Areal Block Proportions (ABPs) with respect the perpendicular depth d starting from the slope surface. It's evident that the roughest profiles are traced for the highest ABP (Montoya-Araque et al., 2020).

Knowing that the height of the slope s_h used in Montoya et al. (2020) model was equal to 10 m it turns out that the failure zone width 0.4*s_h is wider than the failure zone width found by Medley (2004) which varies between 0.1*s_h and 0.15*s_h. This underestimation can be attributed to the fact that Medley (2004) did not consider the effect of the uncertainties highlighted by the stochastic analysis carried out by Montoya et al. (2020).

2.2.1 pyBIMstab software and A* algorithm

In past studies (Guerra et al., 2016; Medley et al., 2004), although LEM was used in 2D bimslopes stability analysis, the paths of the tortuous failure surface (TFS) were visually, manually or semi-automatically plotted implying subjectivity problems in the optimal path selection.

Montoya et al. (2018) have developed a software called pyBIMstab that automatically generates the tortuous failure surface within a bimslope and performs a 2D slope stability assessment through the limit equilibrium method (LEM) under the assumption that the 2D projection of tortuous failure surfaces is linked the irregular network of possible paths with a start point and a variety of possible routes to a unique exit. In this case the LEM is applied through the general limit equilibrium (GLE) formulation allowing to do slope stability analysis both in heterogeneous materials such as bimsoils/bimrocks and in homogeneous materials by identifying tortuous circular failure surfaces respectively (Montoya-Araque et al., 2018). The pyBIMstab software is composed by ten modules as we can see in Figure 26.

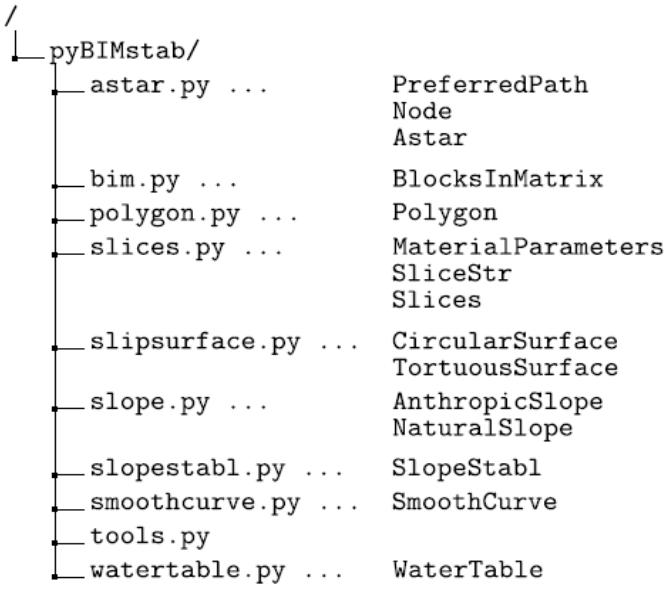

```
/
└─pyBIMstab/
   ├─astar.py ...         PreferredPath
   │                      Node
   │                      Astar
   ├─bim.py ...           BlocksInMatrix
   ├─polygon.py ...       Polygon
   ├─slices.py ...        MaterialParameters
   │                      SliceStr
   │                      Slices
   ├─slipsurface.py ...   CircularSurface
   │                      TortuousSurface
   ├─slope.py ...         AnthropicSlope
   │                      NaturalSlope
   ├─slopestabl.py ...    SlopeStabl
   ├─smoothcurve.py ...   SmoothCurve
   ├─tools.py
   └─watertable.py ...    WaterTable
```

Figure 26: Ten modules with their respective classes (Montoya-Araque et al., 2018).

Some modules have the aim of defining a part of the model geometric structure (e.g. `bim.py`, `slipsurface.py`, `slope.py` and `watertable.py`) instead other modules contain supportive tools (e.g. `polygon.py` and `tools.py`) (Montoya-Araque et al., 2018).

The module `astar.py` is the one that contains the A* pathfinding algorithm that allows to find the optimum tortuous failure surface in a bimslope. Finally, there is the slices.py and slopestabl.py that allow you to carry out the stability analysis of the slope using the GLE procedure. To apply the A* pathfinding algorithm the bimsoil/bimrock structure must be represented as a grid graph in which there are cell arrays that preserve the relational data. Since the algorithm A* has the task of finding the optimal path, in the grid graph there must be hindered cells through which the path cannot pass. This type of information is recorded within the grid graph structure giving the value zero (0) to allowed cells, one (1) to the hindered cells and minus one (-1) to the cells that do not belong to the problem frame (Figure 27).

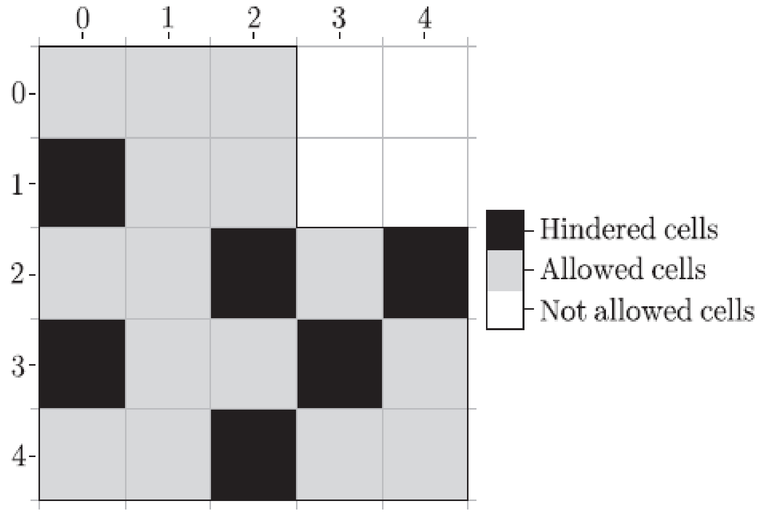

Figure 27: Grid graph representation of a cell array with hindered cells (black cells), allowed cells (grey cells) in which the path can be traced and cells out of the problem frame (white cells) (Montoya-Araque et al., 2019).

Montoya-Araque et al. (2019) for their study modified the classic A* algorithm just explained by making the tortuous path tend to a preferred path to obtain a more curved tortuous failure surface (Figure 28).

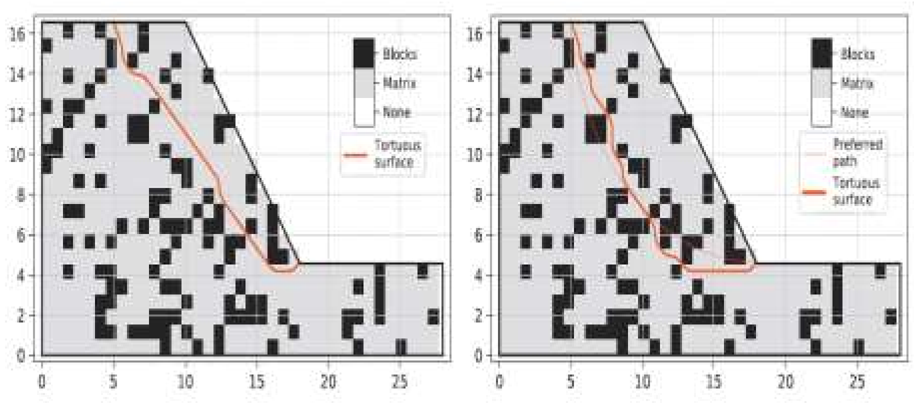

(a) Without a preferred path

(b) Circular surface as preferred path

Figure 28: (a) TFS obtained with the classical A pathfinding algorithm, (b) TFS obtained with the modified A* pathfinding algorithm* (Montoya-Araque et al., 2019).

3. Contribution to the study of tortuous failure surfaces

As already described in Paragraph 2.2, in the studies carried out by Montoya-Araque et al. (2020) a bimslope stability analysis has been carried out using the limit equilibrium method (LEM) which is an approximate method. Furthermore, Montoya-Araque et al. (2019) have developed the modified A* algorithm that in input has a preferred failure surface path which is the matrix-only circular failure surface and, depending on the location and the size of the blocks inside the bimslope, it finds the optimum path of failure. So instead of inventing the position of the failure tortuous surface, they started from a known location of a circular failure surface and automatically the optimum TFS is provided. Once the optimum TFS is known, it is putted in the pyBIMstab software and the factor of safety can be computed to assess the bimslope stability. It is important to observe that all this procedure assumes that the 2D projection of TFSs is compared to the irregular network of possible paths of a “maze” with a starting point and a variety of possible routes to a unique exit (Montoya-Araque, et al., 2020). At the end of their analysis, they provide an indication of the failure zone width found by the numerical analysis they did.

3.1 Study on tortuous failure surfaces conducted by Napoli et al.

Recent studies carried out by Napoli et al. have shown that by doing FEM (Finite Element Method) analysis, the tortuous failure surfaces in bimsoils/bimrocks are absolutely not related to the failure surfaces of the homogeneous material (matrix-only) because performing FEM analysis on heterogeneous material like bimsoils/bimrocks generally very high stresses concentration on the surface of the bimslope have been found and therefore the possible position and the shape of the failure surfaces are completely different each other.

A series of FEM analysis with RS2 software were carried out using a 2D slope model both with homogeneous material, therefore with VBP 0%, and with heterogeneous material with several VBP 25%, 40%, 55% and 70% to consider different position and size of the blocks. In total, 15 models were made for each VBP considered for the heterogeneous material and only one model with VBP 0% for the homogeneous material. The slope height s_h has been set equal to 50m and the slope inclination at 45 °. FEM analysis results of the homogeneous (matrix-only) material with VBP = 0% produced a classic circular failure surface. The blue line was drawn on AutoCAD, it represents the circular failure surface of the homogeneous material (matrix-only) with VBP 0% (Figure 29).

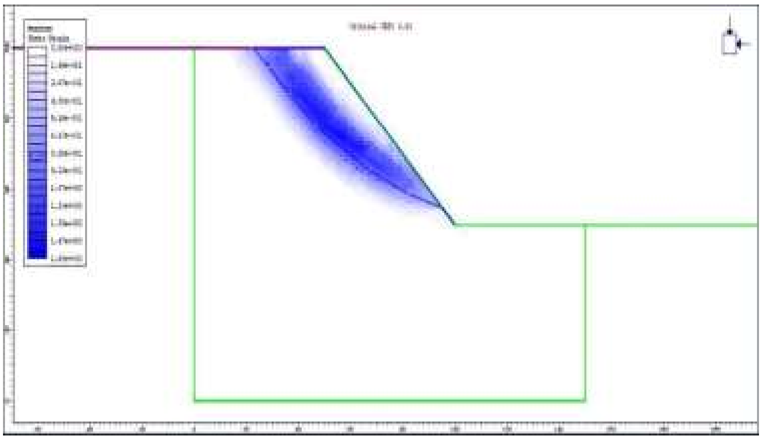

Figure 29: Circular failure surface obtained in the homogeneous material with VBP = 0%.

Instead, the results of the heterogeneous material produced tortuous failure surfaces with different paths and extensions depending on the VBP considered. Even the red line (Figure 30), which indicates the TFS of the heterogeneous material, have been traced on AutoCAD looking at where there are maximum shear deformations. As can be seen there are completely different positions of the tortuous failure surfaces and in some cases, they are very superficial (Figure 31). All these analyses were made with circular blocks of several dimensions to make the results obtained in this thesis comparable with those obtained by Montoya-Araque et al. in 2020.

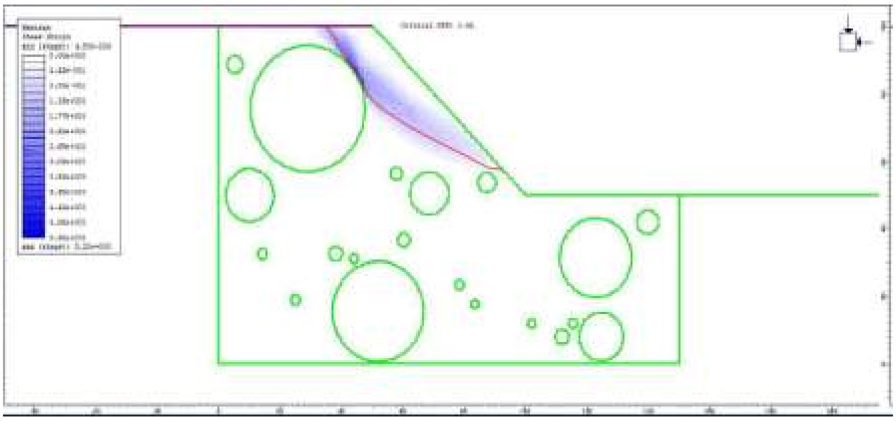

Figure 30: TFS path with VBP = 25%.

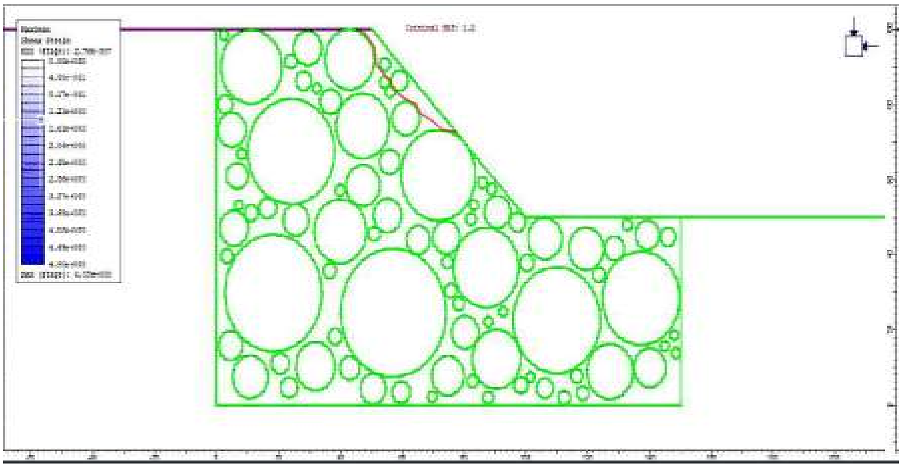

Figure 31: TFS path with VBP = 70%.

An important difference from the Montoya-Araque et al. (2020) model is that for example by overlapping all the TFS of the heterogeneous material of all the 15 models analysed with VBP = 25%, it can be seen that they change between them and that the TFS of the heterogeneous material (red line) almost never starts where the failure surface of the homogeneous material (blue line) starts (Figure 32). This type of result was also achieved, and it is even more evident, for TFS with VBP 40%, 55% and 70% but with different paths shape and length.

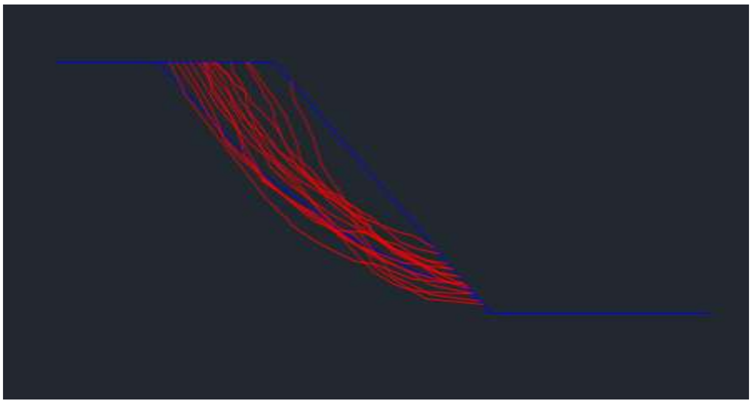

Figure 32: Overlapping of all the 15 TFS obtained from the 15 models with VBP = 25%.

One of the aims of this thesis is to provide a *tortuosity index* of the TFS of the heterogeneous material doing the assumption that the starting and the arrival points of the circular failure surface of the homogeneous material and the TFS of the heterogeneous material don't coincide.

As already highlighted in Paragraph 2.2, Montoya-Araque et al. (2020) have set the circular failure surface of the homogeneous material as preferred path of the modified A* algorithm that starts from a point at the top of the slope and reaches a point at the foot of the slope. Then it automatically found the TFS of the heterogeneous material with the same circular failure surface starting and arrival points. Therefore, with Montoya-Araque et al. (2020) case is quite simple to do image proportions to determine the tortuosity index because the proportions are valid only if the starting and arrival points of the circular failure surface of the homogeneous material and the TFS of the heterogeneous material coincide. If they don't coincide, it isn't possible to do the ratio between the length of the TFS of the heterogeneous material $L_{\_tort}$ and the length of circular failure surface of the homogeneous material $L_{\_arc}$ because we would get a staggered result. Therefore, for Montoya-Araque et al. (2020) case the *tortuosity index* is given by the ratio between the length of the TFS $L_{\_tort}$ to the length of the arc $L_{\_arc}$ which would represent the length of the circular failure surface of the homogeneous material. In this way we can compare two images of different size (Figure 33).

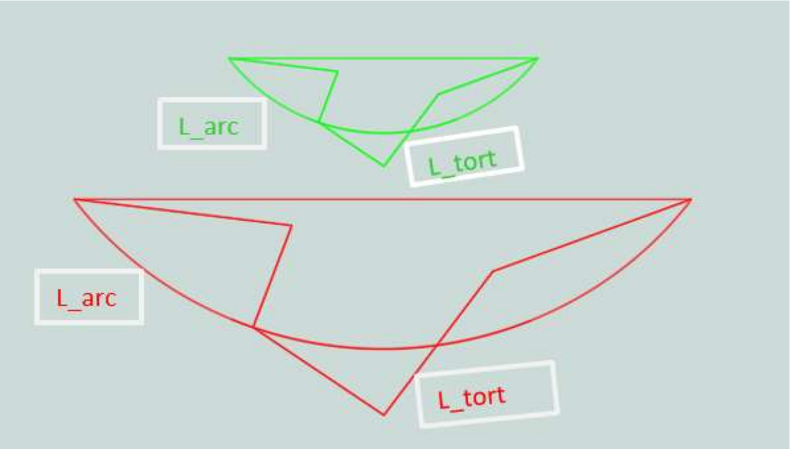

Figure 33: Scheme of the image proportions used to find the tortuosity index in Montoya et al. (2020) research.

Instead, as already said above, in the case covered in this thesis it is considered that the beginning and the end of the circular failure surface of the homogeneous material and the TFS of the heterogeneous material don't coincide. Therefore, to avoid obtaining staggered results with respect to those obtained with Montoya-Araque et al. (2020) case, we must geometrically relate it to the thesis case through the *proportionality ratios between images* as shown in Figure 34.

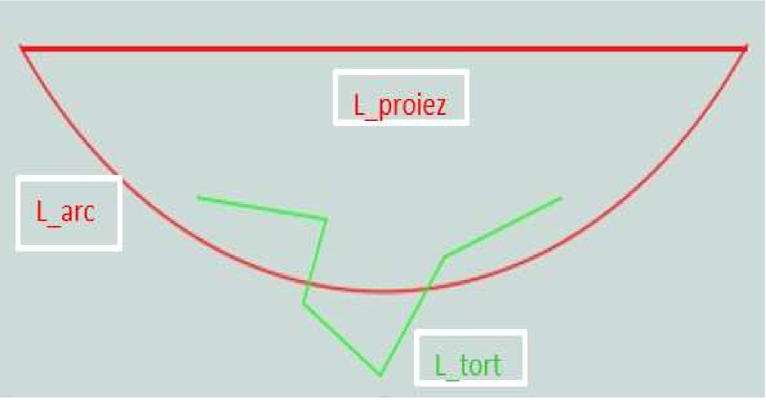

Figure 34: Scheme of the image proportions used to find the tortuosity index in this thesis.

The proportionality ratio between the images is done to say that the length of the TFS $L_{\_tort}$ divided by the length of the projection of the circular failure surface of the homogeneous material $L_{\_proiez}$ is equal to parameter A and the length of the arc $L_{\_arc}$, which would represent the length of the circular failure surface of the homogeneous material, divided by the length of the projection of the circular failure surface of the homogeneous material $L_{\_proiez}$ is equal to parameter B. The parameter B is calculated only one time with reference to the model with VBP 0%. By doing the ratio of A to B the *tortuosity index* of the TFS surface of the heterogeneous material is computed.

3.2 Average tortuosity index and standard deviation as VBP varies

As explained in Paragraph 3.1, to geometrically relate our case to the case of Montoya-Araque et al. (2020), we must use the proportionality ratios between the images. The results obtained from FEM analysis through RS2 software have been reported on AutoCAD to better highlight the tortuous failure surfaces obtained from the models with VBP 0%, 25%, 40%, 55% and 70%.

From the FEM analysis on the heterogeneous materials 15 tortuous failure surfaces were obtained for each VBP equal to 25%, 40%, 55% and 70%, instead only one circular failure surface was obtained for the case with VBP equal to 0% since it is only taken as a reference for the calculation of the parameter B. All the models obtained from the RS2 have been imported on AutoCAD in order to better highlight the tortuous failure surfaces obtained as result of the FEM analysis and then to measure the $L_{\_arc}$, $L_{\_proiez}$, $L_{\_tort}$ lengths of each model necessary to calculate proportionality ratios (Figure 35).

Figure 35: Models obtained on RS2 and imported on AutoCAD.

First, after measuring lengths $L_{\_arc}$, $L_{\_proiez}$, $L_{\_tort}$ for all models with different VBP, parameter B was calculated by referring only to the VBP 0% model. It is calculated only once through the Eq.7.

$$B = \frac{L_{\_arc}}{L_{\_proiez}} \tag{Eq.7}$$

B was found to be equal to 1.01. Next, parameter A was calculated for all models with VBP 25%, 40%, 55% and 70% using the Eq.8.

$$A = \frac{L_{\_tort}}{L_{\_proiez}} \tag{Eq.8}$$

At this point doing the A/B ratio the *tortuosity indexes* for all models with VBP 25%, 40%, 55% and 70% was computed.

In conclusion, for each VBP an average of the tortuosity indexes found was made obtaining the following *average tortuosity indexes* and their *standard deviations* (Table 4).

Table 4: Average tortuosity index and Standard deviation values obtained for each VBP.

VBP [%]	Average tortuosity index	Standard Deviation
25	1.032	0.018
40	1.036	0.023
55	1.050	0.029
70	1.086	0.052

The following diagram (Figure 36) shows the trend of the average tortuosity indexes and their standard deviations as a function of VBP.

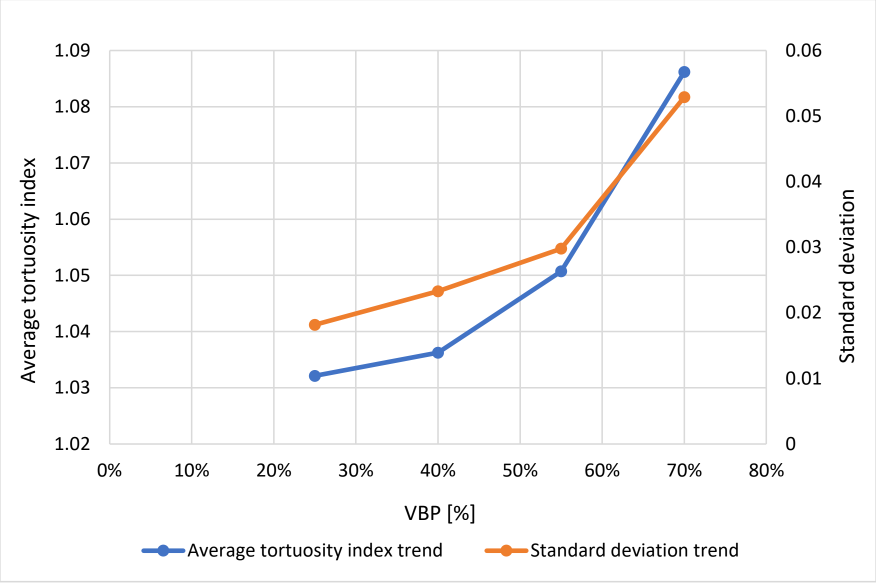

Figure 36: Average tortuosity index and Standard deviation trends as a function of VBP.

As can be seen from the Figure 36, the average tortuosity index increases as the VBP increases. It is also evident that the variability within the set of 15 tortuous failure surfaces for VBP 25%, 40%, 55% and 70% increases as VBP increases.

In this way we can quantify the variability of the failure behaviour of the tortuous surfaces, which changes as the VBP increases. This also makes us claim that the tortuous failure surfaces are not only more tortuous as the VBP increases, but also more irregular. So, if a potential band of instability within a bimslope is considered knowing its VBP, it’ s possible to understand how to proceed in the design phase of the work that needs to be realized.

3.3 Bimslopes stability analysis: failure zone width

Once the tortuous failure surfaces (red lines) of each model obtained from the FEM analysis have been traced more clearly on AutoCAD, they were superimposed to obtain a band of potential tortuous failure surfaces with different trends. In Figure 37, Figure 38, Figure 39 and Figure 40 are shown the results obtained after superimposing all the tortuous failure surfaces for all the VBP considered.

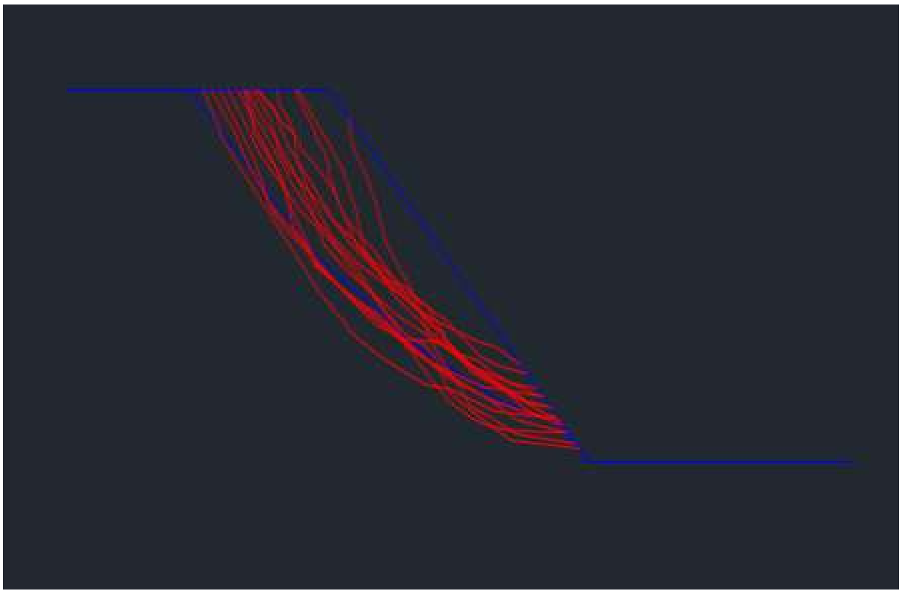

Figure 37: Band of potential tortuous failure surfaces obtained overlapping the tortuous failure surfaces obtained from the 15 models with VBP = 25%.

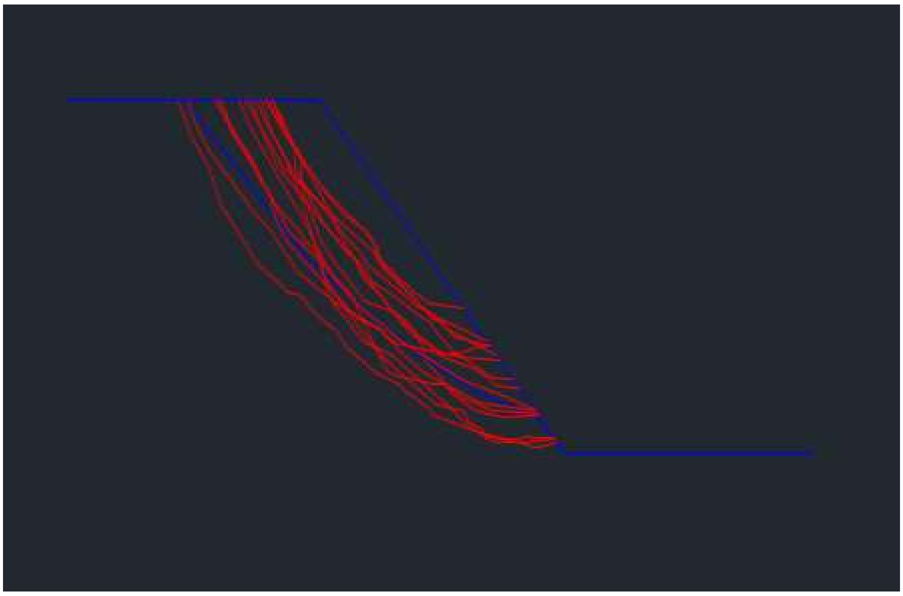

Figure 38: Band of potential tortuous failure surfaces obtained overlapping the tortuous failure surfaces obtained from the 15 models with VBP = 40%.

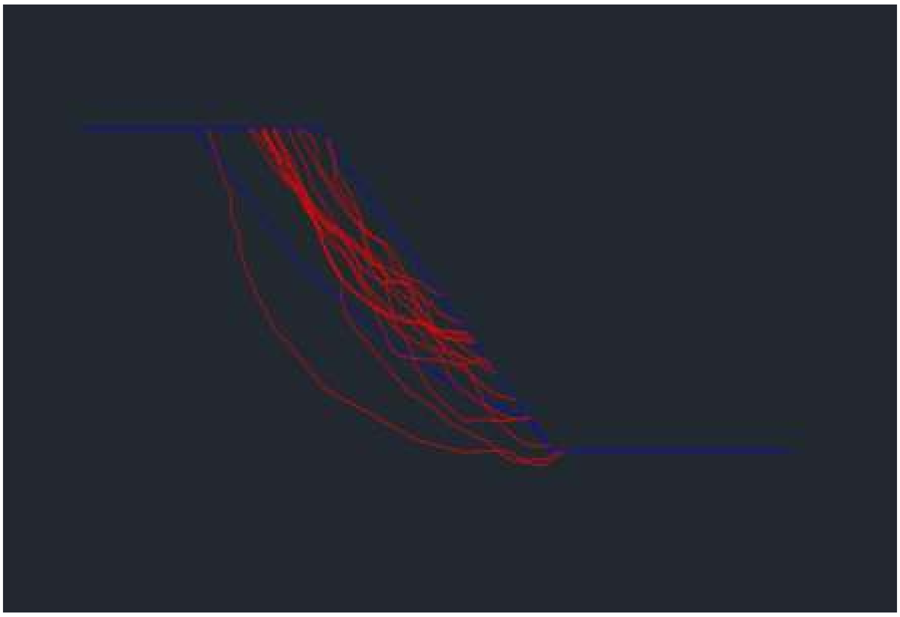

Figure 39: Band of potential tortuous failure surfaces obtained overlapping the tortuous failure surfaces obtained from the 15 models with VBP = 55%.

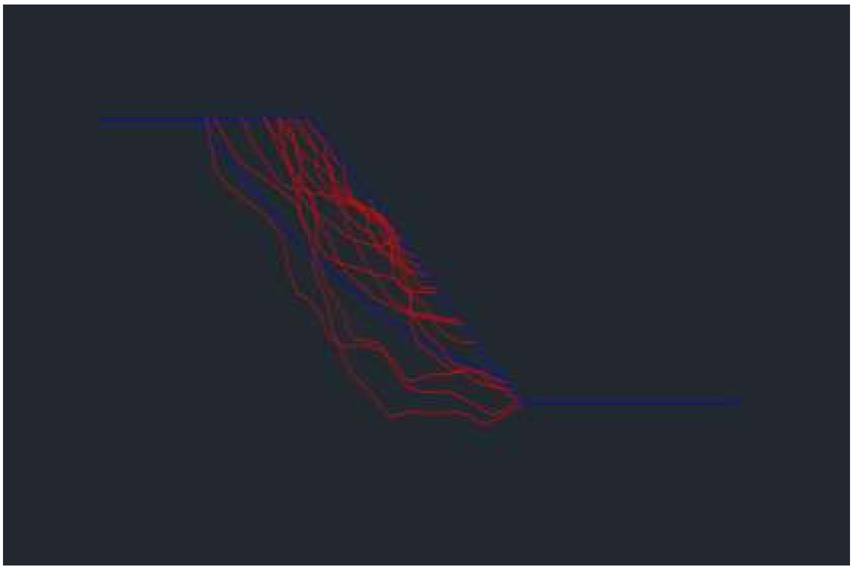

Figure 40: Band of potential tortuous failure surfaces obtained overlapping the tortuous failure surfaces obtained from the 15 models with VBP = 70%.

After overlapping all the tortuous failure surfaces of each model for each VBP the identification of the respective failure zone widths was carried out. To do this, polylines (green lines) composed of various pieces of different tortuous failure surfaces were created to take all the tortuous failure surfaces within a certain band called *failure zone width*. In this way we create for the different VBPs a *minimum fictitious tortuous failure surface* which is located more superficially and a *maximum fictitious tortuous failure surface* which is located deeper. The failure zone widths identified for each VBP by their maximum and minimum fictitious tortuous failure surfaces (green lines) are as illustrated in Figure 41, Figure 42, Figure 43, Figure 44 and Figure 45.

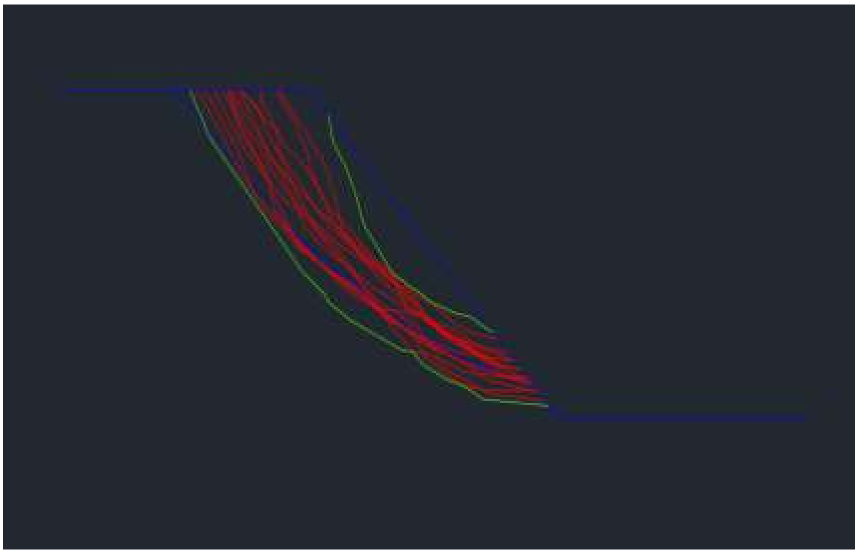

Figure 41: Failure zone width identified in case of VBP = 25%.

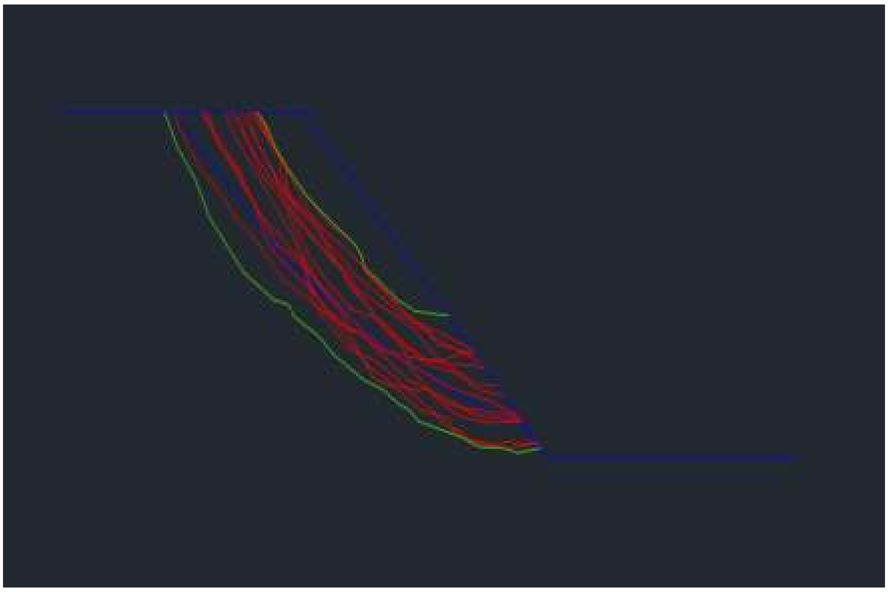

Figure 42: Failure zone width identified in case of VBP = 40%.

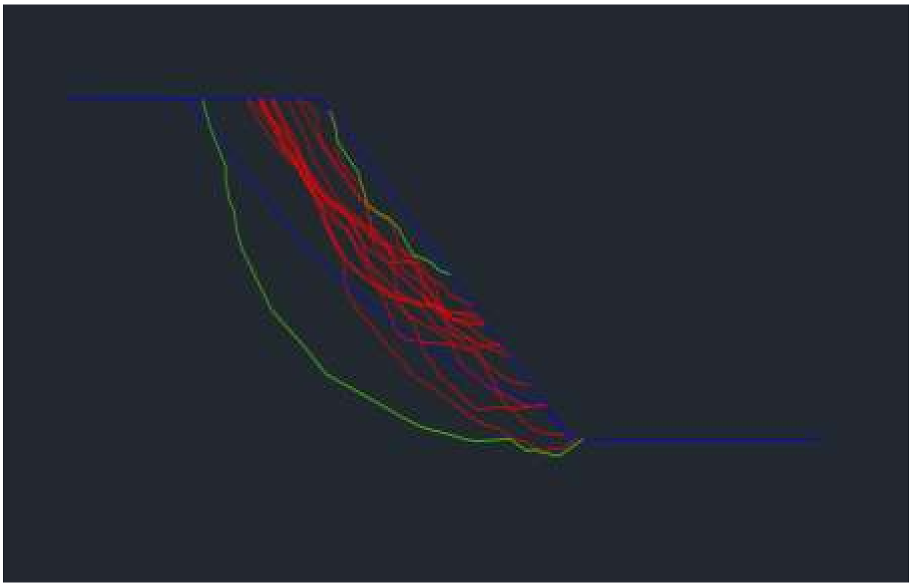

Figure 43: Failure zone width identified in case of VBP = 55%.

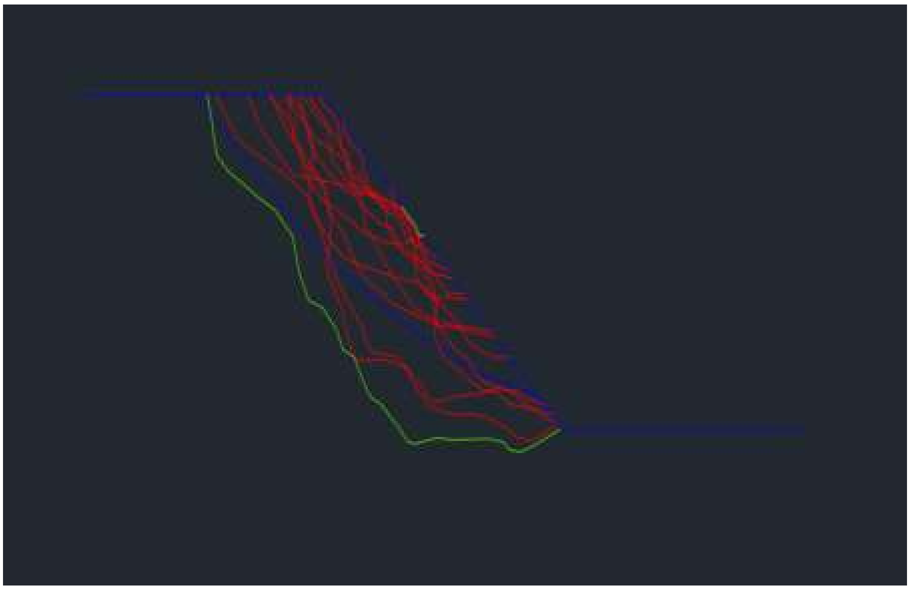

Figure 44: Failure zone width identified in case of VBP = 70%. The minimum fictitious tortuous failure surface in this case is very superficial.

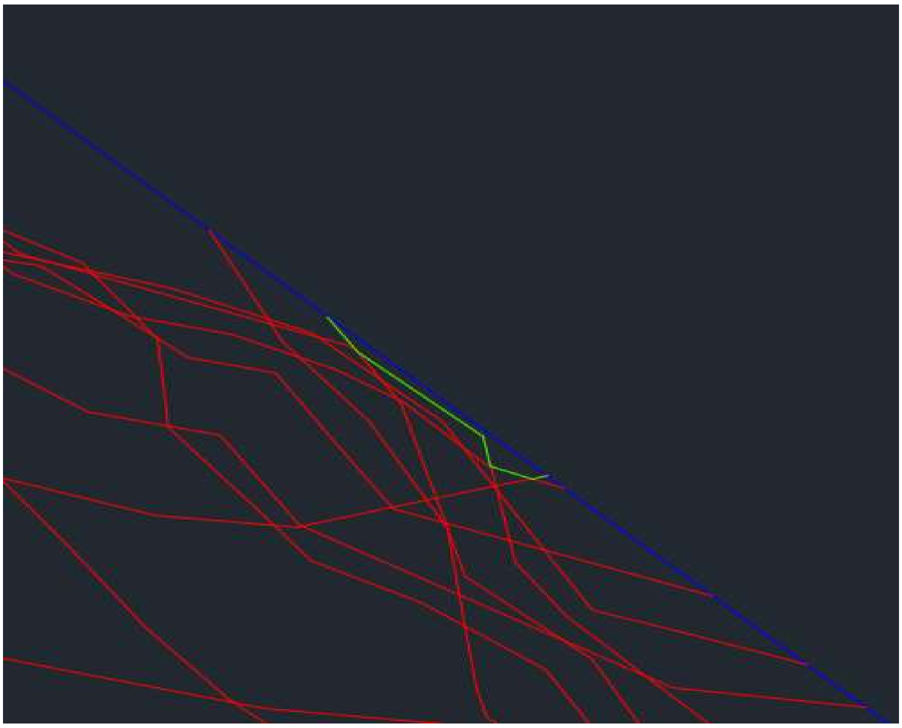

Figure 45: Minimum fictitious tortuous failure surface in case of VBP = 70%.

3.4 Failure zone width estimation as VBP varies

After creating maximum and minimum fictitious tortuous failure surfaces (green lines) the width of the failure zone must be quantified as the VBP varies. As can be seen in Figure 46, Figure 47, Figure 48, Figure 49 and Figure 50, the maximum points of the maximum and minimum fictitious tortuous failure surfaces are identified by shifting the slope, tilted to 45°, to the left until the maximum point of the green curves is found. Therefore, knowing the position of these points it is possible to measure how far these points are from the slope tilted to 45° (blue line) and in this way the maximum depths (light blue lines) of the maximum and minimum fictitious tortuous failure surfaces can be defined.

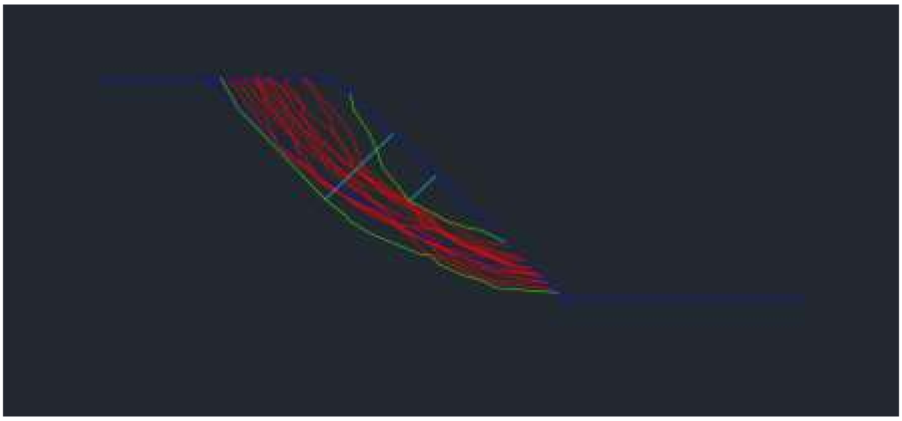

Figure 46: Maximum depths of the maximum and minimum fictitious tortuous failure surfaces in case of VBP = 25%.

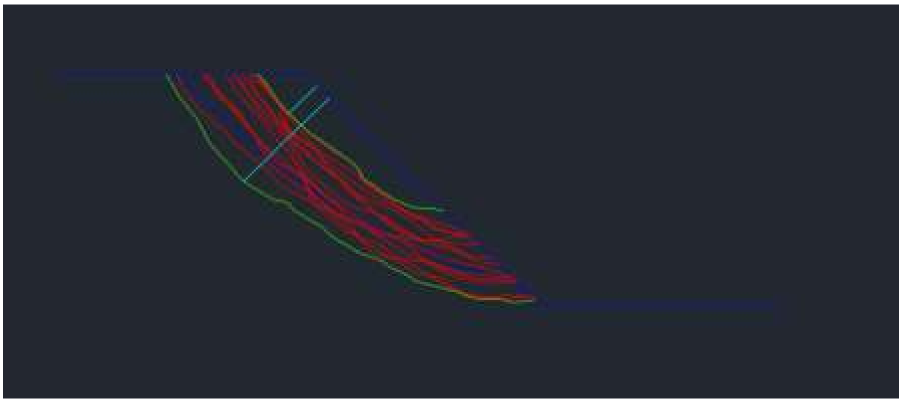

Figure 47: Maximum depths of the maximum and minimum fictitious tortuous failure surfaces in case of VBP = 40%.

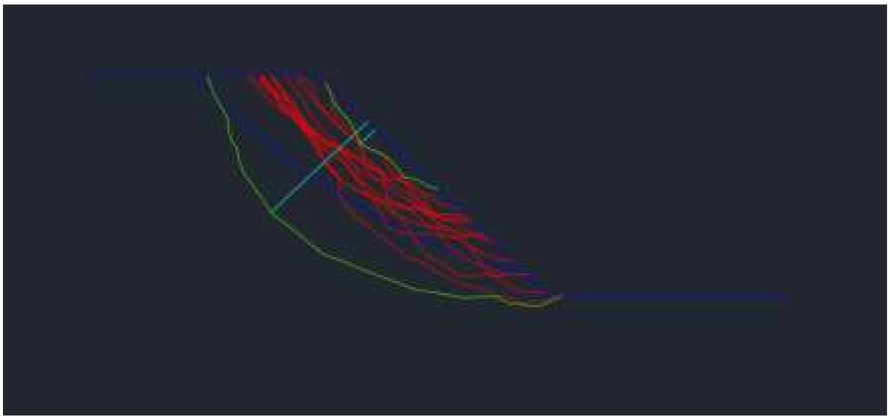

Figure 48: Maximum depths of the maximum and minimum fictitious tortuous failure surfaces in case of VBP = 55%.

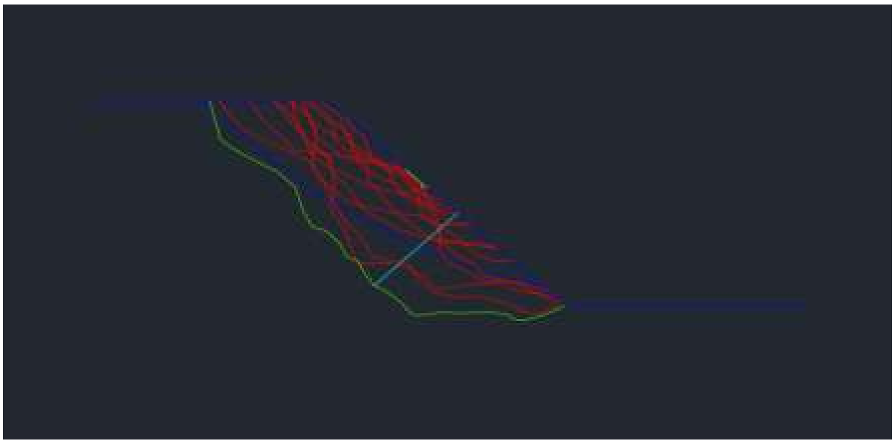

Figure 49: Maximum depths of the maximum and minimum fictitious tortuous failure surfaces in case of VBP = 70%.

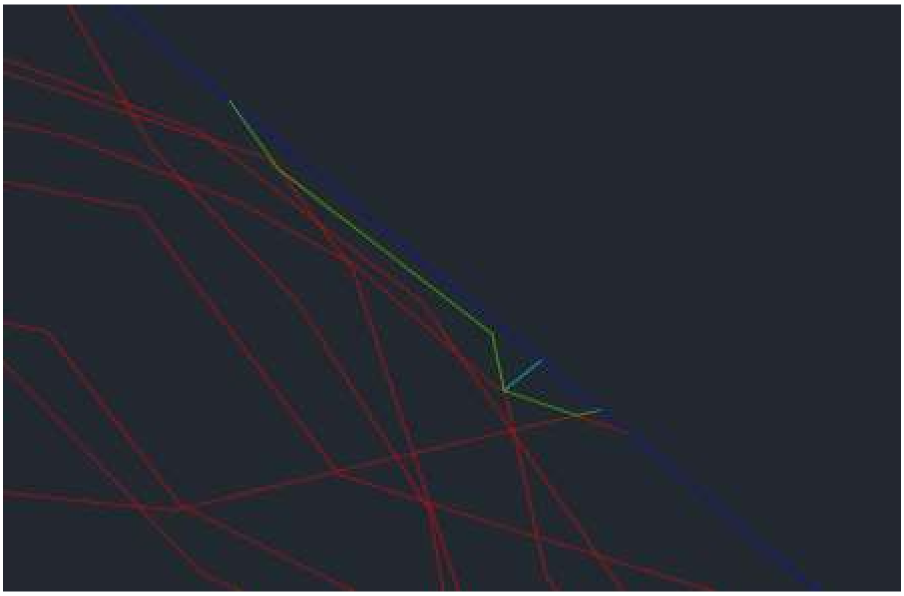

Figure 50: Maximum depth of the minimum fictitious tortuous failure surface in case of VBP = 70%.

The values of the maximum depths d_{min} and d_{max}, respectively of the minimum and maximum fictitious tortuous failure surfaces, perpendicular to the slope tilted to 45° for each VBP are shown in Table 5.

Table 5: d_{min} and d_{max} values for each VBP.

VBP [%]	d_{min} [m]	d_{max} [m]
25	8	21
40	8	25
55	4	29
70	1	25

These maximum depths d_{min} and d_{max} values should be related to the characteristic engineering dimension (or characteristic lenght) L_c which in the case of slopes is the slope height s_h. As was said at the beginning the slope height in the FEM models is equal to 50m. The results for each VBP are listed in Table 6.

Table 6: d_{min} /L_c and d_{max}/L_c values for each VBP.

VBP [%]	d_{min} /L_c	d_{max} /L_c
25	0.16	0.41
40	0.16	0.50
55	0.09	0.58
70	0.01	0.50

From these values the following graph (Figure 51) has been plotted.

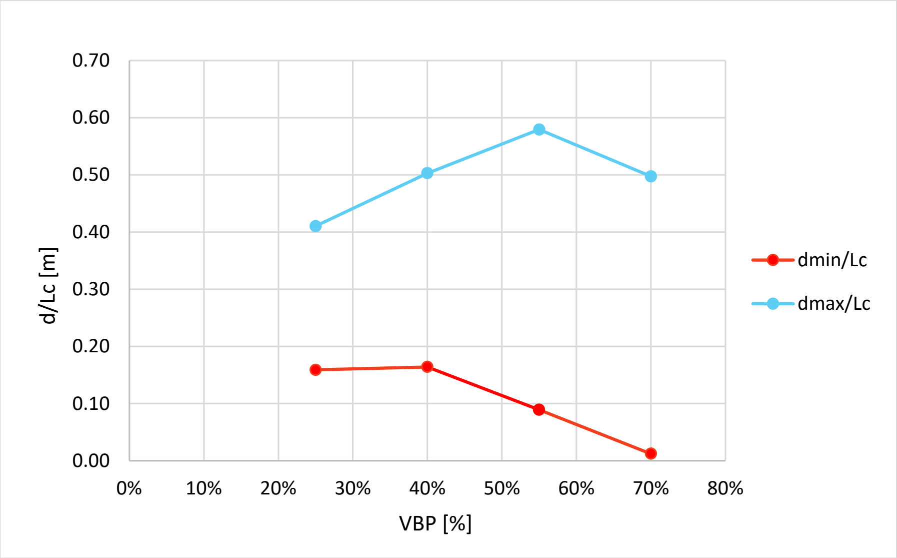

Figure 51: dmin /L_c and dmax /L_c trends as a function of VBP.

In conclusion, to quantify the generic *failure zone width* that contains the multitude of potential tortuous failure surfaces, the average of the dmin/L_c and of dmax/L_c values was calculated, obtaining respectively the values 0.1 and 0.5. In conclusion it is possible to say that the failure zone width is between 0.1*L_c and 0.5*L_c. Therefore, having L_c = 50m, the failure zone width will be between 5 and 25m deep from the surface of the slope.

3.5 Results comparison and considerations

The lower limit of the failure zone width obtained from the analysis performed in the Paragraph 3.4 is equal to 0.1*L_c which coincides with the lower limit of the failure zone obtained by Medley (2004). Instead, the upper limit of the failure zone width 0.5*L_c is far above the upper limit of the failure zone width obtained by Medley (2004) which is equal to 0.15*L_c. Also analysing the results obtained from Montoya-Araque et al. (2020), it can be noted that the lower limit of the failure zone width found is equal to 0.4*L_c and it does not match the one obtained with the result obtained before, instead the higher limit 0.5*L_c coincides.

Medley's results are different mainly because in the FEM analysis made by Napoli et al. circular blocks with variable diameters were used, instead Medley used blocks of variable shape, the tortuous failure surfaces were drawn by hand and the analysis was not done on slopes but on samples tested in triaxial cell. Montoya-Araque et al. (2020) also uses circular blocks of variable diameter in his analysis, but it is likely that the results obtained in this thesis are different from their results because a preferred path wasn't considered and the beginning and end of the circular failure surface of the homogeneous material with VBP = 0% wasn't coincident with the beginning and end of the tortuous failure surface of the heterogeneous material because in reality it is not always true that the points coincide, sometimes they may not even coincide. In conclusion, it can be said that Montoya-Araque et al. (2020) have made too simplifying assumptions which may lead to overestimate the real problem.

4. Triaxial tests on laboratory reconstituted material

This study is part of an unconventional experimentation campaign already started in a previous thesis work (Milan, 2020) and therefore its aim is to integrate the results already obtained to increase knowledge about the effect of VBP on the mechanical behaviour of heterogeneous reconstituted material. To assess the effect of the volumetric percentage of the blocks VBP on the mechanical behaviour of this material, three triaxial tests were carried out. The presence of the clay matrix did not allow the extraction of samples with the most classic core techniques: the use of water could have destroyed the matrix tissue (Cerise, 2019). Due to the impossibility of creating undisturbed and representative samples of the natural material under consideration to carry out triaxial tests, it was decided to reproduce specimens of reconstituted material containing different volumetric block proportions and to analyse the differences between their mechanical responses.

4.1 Triaxial test overview

The purpose of the triaxial tests is to determine the evolution of the stress and deformative state within a specimen loaded in confined compression until failure to be able to evaluate the shear strenght of soils or rocks.

The material fails when the shear stress acting inside the material exceeds the shear strenght τ_R. This shear strenght can be defined, according to the Mohr-Coulomb, criterion as (Eq.9):

$$\tau_R = c' + \sigma' \cdot tg(\varphi') \qquad \text{(Eq.9)}$$

where:

- τ_R is the shear strenght;
- c' there is effective cohesion;
- φ' is the friction angle of the material;
- σ' is the effective stress normal to the sliding plane.

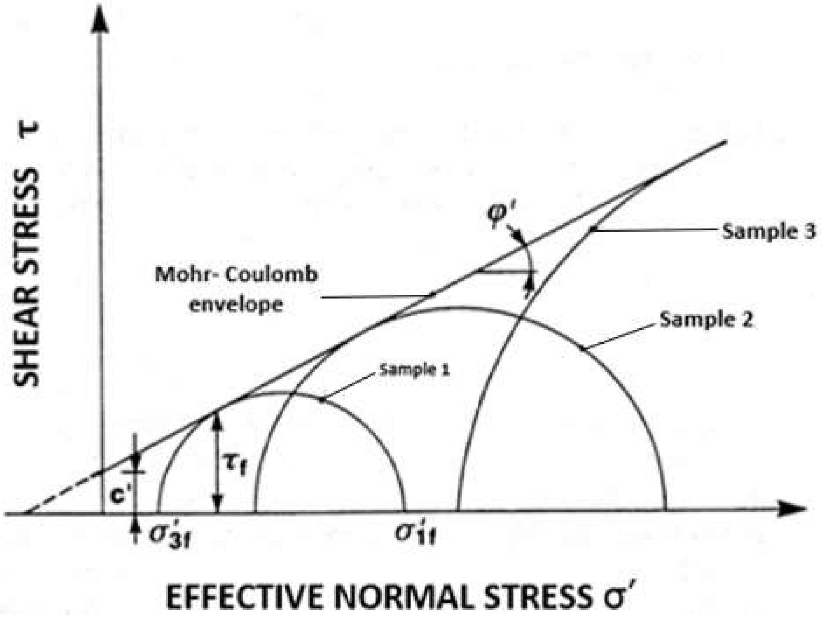

Figure 52: Mohr – Coulomb circles at failure and strenght characteristics in effective stresses (AGI, 1994).

In Figure 52 the linear envelope of the stress states at failure on the Mohr plane is shown. It is described by the parameters c′ and φ′, which vary according to the material under consideration. The shear stress parameters c′ and φ′ are not physical soil characteristics, but are a function of many factors, including stress history, voids index, stress and deformation level, type of structure and particle size composition. Failure occurs in the condition where the effective stress state applied to the specimen corresponds to a Mohr circle tangent to the envelope itself. This condition can be achieved by means of triaxial tests in two different ways, which refer to the extreme drainage conditions of the pore water contained within the specimen:

- undrained conditions, in which locally the volume of the tested sample does not exchange mass of water with the outside and therefore this means that the pore water is supposed to be firm in the pores. If the material is saturated and the hypothesis that the solid particles and the pore water can be considered incompressible is introduced, the definition just given above coincides with that of absence of volume variations (Lancellotta, 2012). The absence of volume variation constitutes an internal constraint within specimen, and as a reaction to this constraint, an excess pore pressure is generated, which makes the effective stresses no longer coincident with the total stresses. Therefore, in undrained conditions the change in the volume of the specimen is prevented, completely preventing the drainage of the pore pressure: changes in effective stress depend on the excess pore pressure spawned and are accompanied only by shear deformations;

- drained conditions, in which at each point in the volume of the specimen the variation in effective stresses coincides with the variation in total stresses (Lancellotta, 2012). In coarse-grained soils, such as sand and gravel, with high hydraulic conductivity ($K \geq 10^{-6}$ m/s), the drained conditions are usually always satisfied in static problems, because an eventual transient motion of the water, caused by any disturbance, takes place in short times and therefore it can be neglected. The pore water is constantly in quiet or stationary motion and its pressure depends only on the boundary conditions. Instead, in fine-grained materials, given their very low hydraulic conductivity ($K < 10^{-7}$ m/s), only if the application speed of the loads is extremely slow it can be thought that the requirements expressed by the definition of drainage condition are met (Lancellotta, 2012). Therefore, for any material in drained conditions there is the cancellation of the excess pore pressure induced by the load application, and therefore both volume deformations and shear deformations occur.

Triaxial test consists of three phases: saturation, consolidation, and shear. To perform the test, a degree of saturation S_r of the specimen, which is the fraction of the volume of voids V_v occupied by volume of water V_w, close to 100% should be ensured. For this reason, the specimen may be subjected to a saturation process. Saturation is achieved by imposing on the tested sample, immersed in distilled water in the triaxial cell, an isotropic *cell pressure* in successive load steps: this pressure acts on the outside of the specimen. The cell pressure is contrasted with a pressure that acts internally to the specimen, called *back pressure*, which is less than cell pressure. The back pressure is also set in successive load steps. The combined action of the two pressures under open drainage conditions progressively saturates the specimens. Guaranteed a degree of saturation of at least 92%, the specimen can be subjected to consolidation(Cianci et al., 2016). The final cell pressure obtained at the end of the saturation process, with relative back pressure, is imposed leaving the drainage open. Since the cell pressure acts evenly throughout the tested sample, an isotropic consolidation is achieved. At the end of the consolidation phase, it is possible to start with the shear phase, in which the speed with which apply the deformation to the specimen is defined. It is generally carried out under compression conditions: the pressure in the cell is kept constant, while the specimen usually is compressed axially from the bottom to top at constant deformation speed. In the Paragraph 4.2.4 the three phases of the triaxial test will be discussed in more detail.

Depending on the drainage conditions imposed during the execution of the consolidation and shear phases, the triaxial tests are divided into:

- Unconsolidated - Undrained tests (UU tests), during which drainage is prevented both in the consolidation phase and in that of application of the axial load;

- Consolidated - Undrained tests (CU tests), during which drainage is fully permitted during the consolidation phase but prevented during the application of the axial load;

- Consolidated - Drained tests (CD tests), during which drainage is fully permitted at both stages of execution.

The three types of triaxial test differ in the information they can provide about the mechanical behaviour of the soils and the execution costs, dictated by the timing required for their execution. CU and CD tests require lower load application speeds than UU tests, as it is necessary to respect the rate of water filtration inside the material to avoid the onset of excess pore pressure. In general, in the UU test the load is applied at speeds comprised between 0.7 and 1.1 mm/min (Cianci et al., 2016), while in the CU and CD tests the load application speed is comprised between 0.010 mm/min, for sandy silt with plasticity index under 10, and 0.001 mm/min for clays with plasticity index over 50 (AGI, 1994).

The evaluation of the parameters obtained from the triaxial tests is therefore of major importance for the solution of most geotechnical problems, where it is necessary to know the soil shear stress.

4.1.1 UU test

In UU tests, drainage is prevented both in the consolidation and in application of the axial load phases. In this way, assuming that the specimen is saturated, the water

content, the void index, and the effective stresses σ′ remain constant throughout the duration of the test (Lancellotta, 2012).

The shear stress in this case is expressed in terms of total stresses σ as the pore pressure is not measured and represents the stress of the soil on site when there have not yet been any changes in the void index and water content. The results are good if they are made on undisturbed samples of good quality.

The UU test shall be carried out on at least three test samples at different total cell pressures to be able to define a minimum parameterization on a statistical basis (Cianci et al., 2016). Since the effective pressure of consolidation of the three specimens is the same, the Mohr circles at failure of the three test samples in the plane of the total stresses will have the same diameter and therefore they will be enveloped by a horizontal line described by Eq.10.

$$\tau = c_u \qquad \text{(Eq.10)}$$

In the case of saturated specimens, the failure envelope expressed in terms of total stresses is taken horizontally and the intercept with the axis of the ordinates represents the shear strenght to undrained shear stress indicated with c_u (Figure 53).

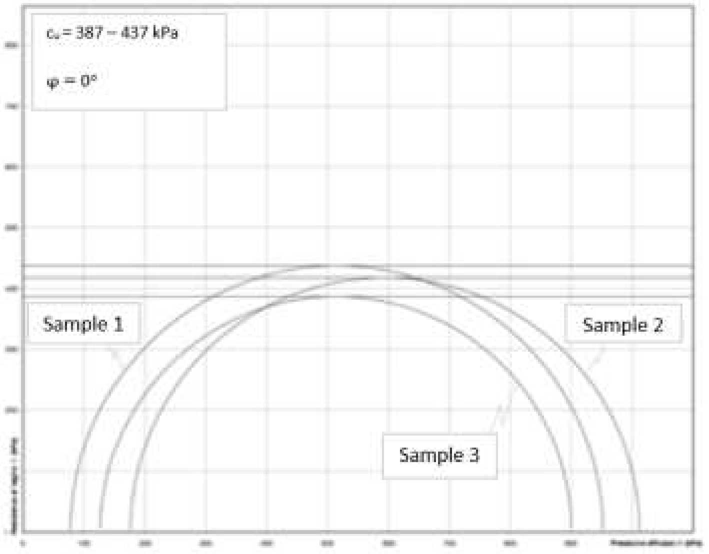

Figure 53: Failure envelopes of three samples in terms of total stresses (Cianci et al., 2016).

The UU test, however, has some limitations because:

- the measured shear stress is only useful for analysis in terms of total stresses;
- the application of an isotropic pressure during the test does not allow the geostatic conditions to be reproduced appropriately. The c_u values obtained are influenced by this limit.

4.1.2 CD and CU tests

The CD and CU tests have the same saturation and consolidation procedure, but they differ in the shear phase.

In the shear phase, a constant speed of deformation is imposed up to the maximum shear strenght of the specimen.

- in the case of CU tests this phase is carried out with the drainage closed, so there is no change in volume and the excess pore pressures generated are measured;

- in the case of CD tests, the shear phase is conducted with the drainage opened to allow the dissipation of the excess pore pressures, measuring the change in the volume of the specimen.

By repeating the tests on different specimens with various stress states it is possible to draw the failure envelope that allows to define the parameters c′ and φ′ respectively called effective cohesion and friction angle.

4.2 Triaxial CIU test

Consolidated - Undrained tests (CU) were carried out at the laboratory of the Department of Structural, Geotechnical and Building Engineering of Polytechnic of Turin. Due to the reduced hydraulic conductivity of the material analysed, they would have constituted a good compromise between the quality of the information obtainable about the mechanical behaviour of the specimens and the timing of execution. In addition, the same procedures and equipment were used to remain consistent with the tests carried out previously (Milan, 2020). The consolidation phase was carried out in an isotropic way, which is why the test abbreviation also has the letter "I". During the execution of this type of tests, the shear phase is conducted with the drainage closed, so there is no change in volume and the generated pore pressures are measured. By repeating the tests on several specimens, consolidated at different loads, it is possible to determine the Mohr-Coulomb failure envelope and obtain the shear strenght parameters: effective cohesion c′ and friction angle φ′.

4.2.1 Skempton’s coefficient A and B

The analysis of the pore pressure variations measured during the triaxial test shear phase also allows to determine the Skempton’s coefficients A and B. In the case of undrained consolidated triaxial tests carried out on saturated specimens, it is possible to measure them using the theory developed by Skempton in 1954. He considered a poorly permeable, saturated soil element under the groundwater table within a homogeneous deposit with a horizontal ground level. For cylindrical symmetry, vertical and horizontal geostatic stresses are main stresses, and the main horizontal stresses are equal to each other (axial-symmetric stress state). It is assumed that the vertical stress corresponds to the greater main stress σ_1 and the horizontal stress corresponds to the lower main stress σ_3. As can be seen in Figure 54, by definition in a piezometric tube placed at the depth of the element the water would go up to the depth of groundwater table (Lancellotta, 2012).

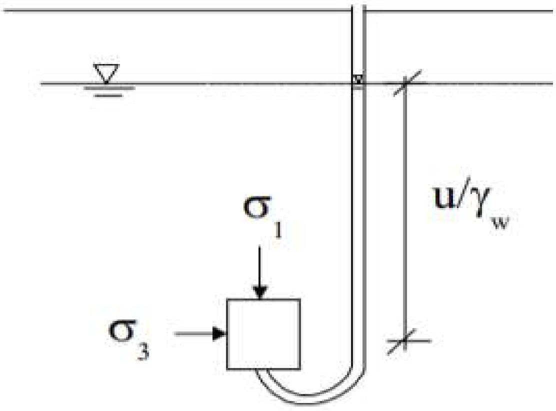

Figure 54: Initial state (Whitlow, 1996).

Moreover, it is supposed that a load applied instantaneously to the surface produces instantaneously, in the element of soil considered, an axial symmetrical increment of the total stress state. Therefore, there will be a $\Delta\sigma_1$ increase in the main vertical stress, a $\Delta\sigma_3$ increase in the main horizontal stress and, consequently, a Δu increase in the pore pressure witnessed by a rise in water level in the piezometer of the amount $\Delta u/\gamma_w$ (Figure 55).

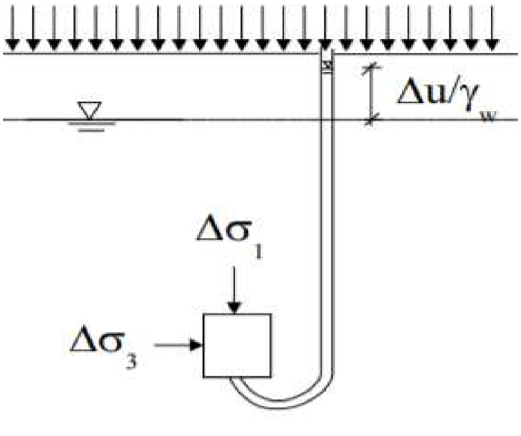

Figure 55: Instantaneous increase of the total stress state (Whitlow, 1996).

At this point it is possible to think of decomposing the increase of the total stress state into two parts (Figure 56):

- a first part in which there is an initial isotropic increase in total stresses of intensity $\Delta\sigma_3$;
- a second part in which there is a deviatoric stress increment of intensity $(\sigma_1 - \sigma_3)$ acting only in vertical direction.

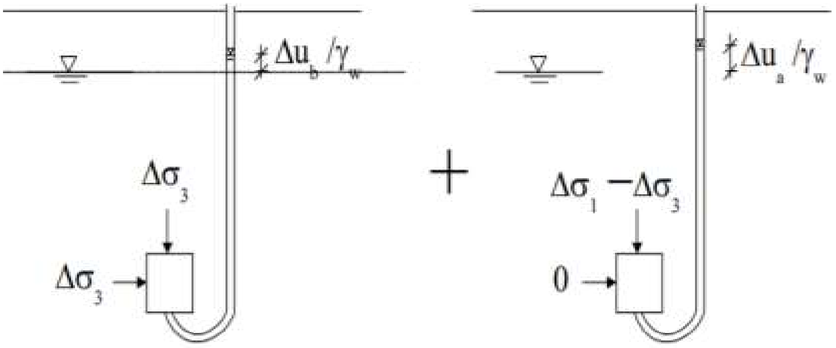

Figure 56: Decomposition of the increase of the total stress state (Whitlow, 1996).

With Δu_b is indicated the increase of pore pressure caused by the increase of total isotropic stress $\Delta\sigma_3$, and with Δu_a the increase of pore pressure caused by the increase of total deviatoric stress $(\Delta\sigma_1 - \Delta\sigma_3)$. Of course, Δu must be equal to the sum of Δu_b and Δu_a (Eq.11).

$$\Delta u = \Delta u_b + \Delta u_a \qquad \text{(Eq.11)}$$

Therefore, with B is indicated the relationship between the increase of pore pressure Δu_b and the increase in total isotropic stress $\Delta\sigma_3$ (Eq.12).

$$B = \frac{\Delta u_b}{\Delta\sigma_3} \qquad \text{(Eq.12)}$$

Similarly, with Ā is indicated the relationship between the increase of pore pressure Δu_a and the increase in total isotropic stress ($\Delta\sigma_1$-$\Delta\sigma_3$) (Eq.13).

$$\bar{A} = \frac{\Delta u_a}{(\Delta\sigma_1 - \Delta\sigma_3)} \qquad \text{(Eq.13)}$$

As a result, the excess pore pressure Δu can be calculated, known parameters B and Ā, with the relation Eq.14.

$$\Delta u = B \cdot \Delta\sigma_3 + \bar{A} \cdot (\Delta\sigma_1 - \Delta\sigma_3) \qquad \text{(Eq.14)}$$

Substituting A = Ā/B the following relation Eq.15 is obtained.

$$\Delta u = B \cdot \Delta\sigma_3 + A \cdot (\Delta\sigma_1 - \Delta\sigma_3) \qquad \text{(Eq.15)}$$

Parameters B, A (and Ā) are called pore pressure parameters or Skempton's coefficients and they can be determined in laboratory with undrained consolidated triaxial tests (Skempton, 1954).

4.2.1.1 Coefficient B

First, it is important to restate the definition of degree of soil saturation S_r (Eq.16) already seen above, which is the fraction of the volume of voids V_v occupied by volume of water V_w (Lancellotta, 2012).

$$S_r = \frac{V_w}{V_v} \qquad \text{(Eq.16)}$$

If the soil element is saturated ($S_r = 1$), assuming negligible compressibility of water, the application of a total isotropic stress increment $\Delta\sigma$ under undrained conditions does not produce any deformation (neither volumetric nor distortion) and therefore, according to the principle of effective stresses (Lancellotta, 2012), does not even produce variations in effective stress ($\Delta\sigma' = 0$). Therefore, for a saturated soil, it is possible to obtain the Eq.17 and Eq.18:

$$\Delta\sigma = \Delta\sigma' + \Delta u = \Delta u; \qquad \text{(Eq.17)}$$

i.e.:

$$B = \frac{\Delta u}{\Delta\sigma} = 1. \qquad \text{(Eq.18)}$$

If, on the other hand, the ground element was completely unsaturated ($S_r = 0$), the application of a total isotropic stress increment $\Delta\sigma$ would produce a volumetric deformation (isotropic if the solid skeleton is isotropic) and an equal increment in effective stress ($\Delta\sigma' = \Delta\sigma$).

Therefore, for dry soil, the Eq.19 and Eq.20 are given:

$$\Delta\sigma = \Delta\sigma' + \Delta u = \Delta\sigma' \qquad \text{and so } \Delta u = 0; \qquad \text{(Eq.19)}$$

i.e.:

$$B = \frac{\Delta u}{\Delta \sigma} = 0. \quad \text{(Eq.20)}$$

In intermediate cases, therefore for partially saturated soils, the following Eq.21 and Eq.22 can be considered:

$$\Delta\sigma = \Delta\sigma' + \Delta u \qquad \text{with } \Delta\sigma' > 0,\ \Delta u > 0; \quad \text{(Eq.21)}$$

i.e.:

$$0 < B = \frac{\Delta u}{\Delta \sigma} < 1. \quad \text{(Eq.22)}$$

Parameter B depends on the degree of soil saturation S_r, with a non-linear law (Whitlow, 1996). From the measurement of the pore pressure, it is therefore possible to calculate the degree of saturation of the specimen which in saturated conditions is equal to 1 (Figure 57).

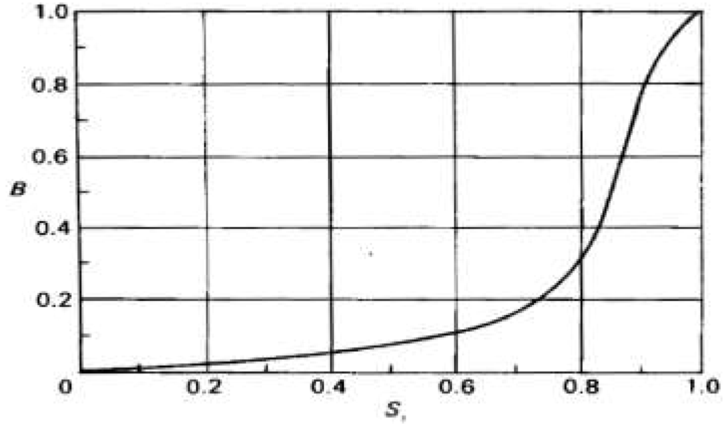

Figure 57: Typical relationship between Skempton's coefficient B and degree of saturation S_r (Whitlow, 1996).

4.2.1.2 Coefficient A

As seen in the previous paragraph, if the soil element is saturated it means that B=1, and so parameters A and $\bar{A}=A \cdot B$ coincide. For a given soil, their value is not unique, as for parameter B, but depends on the level of applied stress and strain. In addition, both the drainage conditions and stress history influence A value (Whitlow, 1996). A material in which the maximum effective vertical stress to which each element of the material has been subjected coincides with the actual effective vertical stress is defined as normally consolidated (NC). Instead, a material is defined as over-consolidated (OC) if the actual effective vertical stress is lower than the value reached during its history. For clays the A value varies differently if they are normally consolidated or over-consolidated. In the case of NC clay, A always assumes positive values, while in the case of OC clay it varies between positive and negative values (Cianci et al., 2016). For these reasons, it is fundamental to relate a measured value of A to a stress-strain parameter, such as the deviatoric stress or the overconsolidation ratio OCR. The OCR allows characterising the stress history of soils (Lancellotta, 2012). It is given by the ratio between the maximum effective vertical stress that the soil had in its history, σ'_p, and the actual vertical stress, σ'_{v0} (Eq.23).

$$\mathrm{OCR} = \frac{\sigma'_p}{\sigma'_{v0}} \qquad \text{(Eq.23)}$$

The values of A can be established by using data collected during a triaxial test. The value assumed by the parameter A at the time of the specimen shear failure is indicated by A_f, which therefore represents the ratio of the excess pore pressure in undrained condition at failure Δu_f, and the corresponding value of the total deviatoric stress increase $(\sigma_1 - \sigma_3)_f$. The value of A_f depends on many factors, the main of which is stress history, i.e., the overconsolidation ratio OCR. For normally consolidated clays (OCR = 1) A_f has values usually between 0.5 and 1, while for strongly over-consolidated clays (OCR > 4) A_f takes on negative values (Whitlow, 1996). It is important to underline the physical meaning of A and reflect on its consequences in the mechanical behaviour of geotechnical works: a positive value of A means that the pore pressure in the soil grows with the total deviatoric stress. On the other hand, if A is negative, the pore pressure decreases. However, it should be noted that A_f values, generally reported in literature and in geotechnical laboratory reports, cannot be used to assess excess in pore pressure under operating conditions, since they refer to different stress conditions.

4.2.2 Equipment

The main part of the equipment consists of the cell which is a cylindrical chamber whose bases are two circular flanges, base plate and upper plate, spaced with three pillars, while the side surface is bounded by a cylindrical plexiglass container. The confinement pressure is supplied to the sample by filling the cell with pressurised distilled water.

The sample, a cylinder 38.1mm in diameter and 76.2 in height, is mounted inside the cell between two load plates which have the same diameter of the sample. One of these two load plates, the lower, is integral to the cell structure. It can slide vertically and is connected externally to the load piston. Above the upper load plate there is the load cell which is a transducer for axial load measurement.

Generally, both the upper and lower load plates are equipped with two holes which allow the passage of pore water from the tested sample to the drainage circuits to allow the expulsion of water and the measurement of volume variations in the drained tests, as well as the measure of the pore pressure. In other types of triaxial cell these measurements are carried out only from the hole in the lower load plate. To facilitate the transfer of interstitial fluids from the sample to the fluid control/measurement system, two porous stones with greater permeability than the tested soil are added between the two load plates and the specimen. Porous stone disk must have a higher permeability K than soil. In cohesive soils K values between 10^{-6} and 10^{-7} m/s are recommended (AGI, 1994). The insulation of the sample from the cell fluid is achieved by means of a latex membrane that is fitted around the sample and hermetically sealed with rubber gaskets (O-Ring) fixed around the latex membrane and the load plates. The scheme of the triaxial cell is shown in Figure 58.

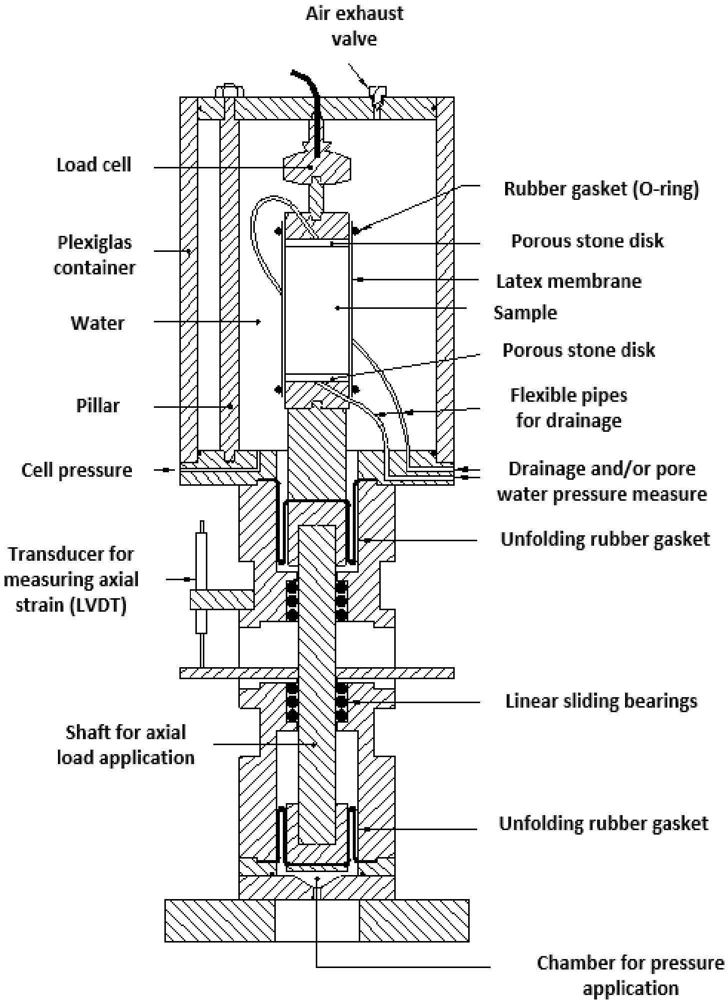

Figure 58: Triaxial test equipment cross section (Lancellotta, 2012).

Moreover, in Figure 59 is shown the triaxial cell used to conduct the experimental tests under discussion.

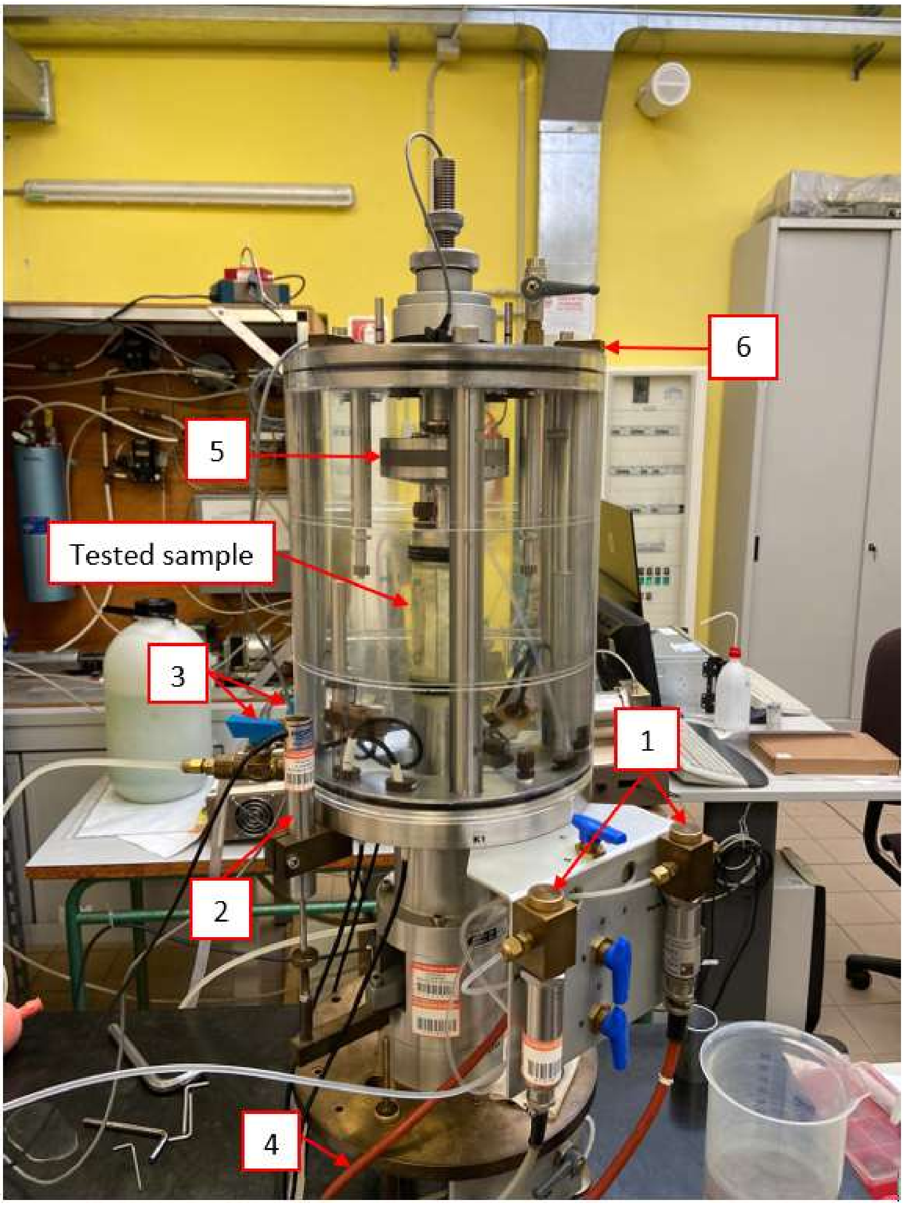

Figure 59: Triaxial cell in the geotechnical laboratory of the Polytechnic of Turin. It is possible to observe the tested sample wrapped by the latex membrane, the transducers for measuring pore pressure at the top and at the bottom of the specimen (1), the transducer for measuring vertical displacements (LVDT) (2), the connecting valves to cell pressure control system and filling tank (3), the transducer for measuring cell pressure (4), the load cell for axial load measurement (5), the anchor pin for securing the cylindrical plexiglass container (6).

4.2.2.1 System for regulation and measurement of pressure in cells

An *“air-water” pressure transmission system* (Figure 60) is used to provide the pressure in the cell. A tank containing air and water is connected externally to the compressed air circuit. The variation of air pressure inside the tank is transmitted instantly to the fluid and consequently to the cell to which the tank is connected by a special tube. The pressure inside the tank is regulated by an electro-pneumatic transducer that can be driven through the test management software.

The system is servoassisted because the software of management monitors in continuous the value of the pressure of the water measured from the transducer of cell pressure (4) placed on the inferior flange of the cell (Figure 59) and sends an electrical signal to the electro-pneumatic transducer that like a tap opens or closes maintaining the set pressure with an error of ±0.5 kPa.

Figure 60: "Air-water" pressure transmission system.

4.2.2.2 System for axial load control

The application of the axial load is guaranteed by a pneumatic system. A shaft, connected to the lower load plate, moves inside a linear sliding bearing system under the pressure of a fluid contained in a chamber at the base of the shaft (Figure 58). The devices that manage the pressure of the fluid inside the chamber differ depending on whether you want to conduct the test under load control or at the speed of deformation imposed. If the movement of the piston is managed in load control the pneumatic system used is similar to that for the regulation of pressure in the cell. In a tank, completely saturated with water, a latex lung connected externally to the compressed air circuit is immersed. The variation in air pressure within the lung is transmitted instantaneously to the fluid and consequently to the piston. The measurement of the axial load applied to the tested sample is guaranteed by the load cell (5) (Figure 59).

Instead in the case of deformation-controlled tests, the equipment is composed by a pump driven by a stepper motor. The piston of the pump advancing with controlled speed, injects water into the chamber placed at the base of the shaft allowing a movement in vertical direction.

The characteristics of the pump used in the laboratory of the Polytechnic of Turin are:

- the maximum value of the pump is 2 MPa, but the maximum pressure of the unfolding rubber gasket (Figure 58) is 1 Mpa. When the deflection control test is conducted, the maximum limit is constrained by the pressure limit reached in the chamber at the base of the shaft (1Mpa);
- the maximum travel of the load shaft is 25 mm, corresponding to a deformation on the tested sample of about 30%.

4.2.2.3 System for the control and measurement of pore water pressure

The presence of air in the drainage circuits or in the sample causes considerable disturbance in the measurement of pore pressure. Furthermore, if the specimen was unsaturated, it would fall back into the unsaturated field, which has a completely different theory than the saturated one. For these reasons, in the saturation phase, and in the drained tests, it is customary to provide a pressure to the water contained in the drainage circuits to expel the air in excess. The pressure thus set to the pore water of a sample is called *back pressure*.

The measurement of the pore water pressure (or of the back pressure) is guaranteed by the presence of two pressure transducers (1) placed at the base of the drainage circuit (Figure 59). One measures the pressure at the top of the sample and the other at the bottom. In other types of triaxial cell it's possible to find only one pressure transducer that measure only the pressure at the bottom of the sample.

The system used for the measurement of volume variations in the sample and for the back pressure control is the *volumometer* (Figure 61).

The volumometer consists of a closed cylinder containing two chambers separated by a piston that can flow freely. The complete separation of the two chambers is guaranteed by the presence of two elastic membranes. Both chambers are filled with water; the lower chamber is connected to an air-to-water pressure control system similar to the one already described for the cell pressure control, while the upper chamber is connected to the cell drainage circuit.

Using an electro-pneumatic regulator driven by PC, you can set the pressure in the air-water lung and then in the lower chamber of the volumometer. The pressure is transferred, through the piston, to the upper chamber and then to the test piece. If the pressure inside the tested sample increases, the system, to maintain constant pressure, tends to decrease the pressure in the lower chamber of the volumometer with the consequence that in the upper chamber there is a pressure greater than the lower one and then the piston tends to lower. By measuring the relative displacement of the piston with a LVDT displacement transducer it is possible to determine the measurement of the ΔV.

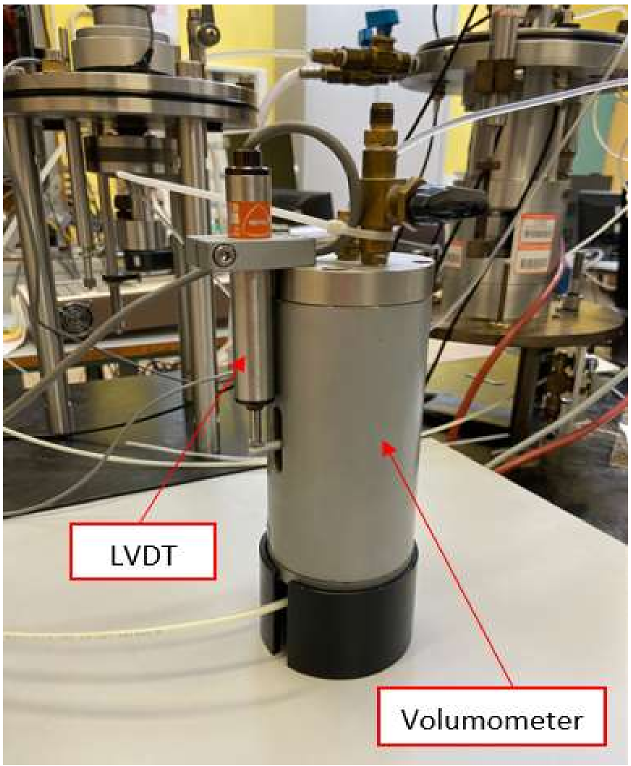

Figure 61: Volumometer and LVDT displacement transducer.

Through a control panel consisting of three three-way taps, it is possible to manage the flow of water from the sample to the volumometer and vice versa.

4.2.2.4 Accessories for mounting the tested sample

The accessories necessary for the correct assembly of the soil sample within the triaxial cell (Figure 62) are:

- A: membrane stretcher;
- B: filter paper for lateral drainage;
- C: vacuum pump to stretch the membrane;
- D: latex membrane for 38 mm test-sample;
- E: O-Rings for hermetic membrane closure on load plates;
- F: O-Rings tool;
- G: porous stone disks.

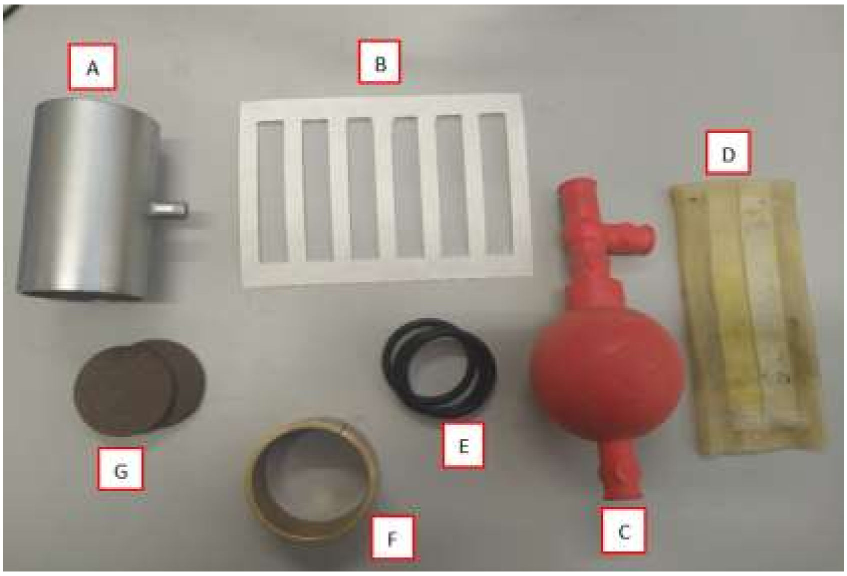

Figure 62: Sample preparation equipment.

To facilitate the drainage of water from the sample to the drainage circuit, porous stones disks are placed between the sample and the loading plates. In general, porous stone disks must have the same diameter as the sample, they must be very resistant to be able to withstand even very high stress without deformation and must have a higher permeability than that of the soil tested. The permeability of porous stones depends on how fine the material used for their realization is.

Latex membranes for triaxial testing are used to isolate the test specimen from the cell fluid.

Since the specimen is surrounded by an impermeable membrane, the flow of water that occurs during consolidation or shear phase in drained condition occurs only in the vertical direction. To accelerate the test time, it is necessary to facilitate this flow so that it occurs in all directions and especially in the radial direction which is the shortest route that water can take. For this reason, especially for poorly permeable soils, strips of filter paper are added along the side walls of the tested sample. The most used filter paper is Whatman N° 54 because it is a paper that does not deteriorate even for long periods of stay in the water.

4.2.3 Installation and assembly

The following are the preliminary operations to be performed before starting the TX CIU test:

1. Before mounting the sample make sure that the volumometer is full of water and saturate the drainage circuits. The water within the volumometer and in the drainage circuits must be distilled and deareata.
2. Close the volumometer valve and, acting on the control panel of the drainage circuit, properly open the valves in order to release water from the drainage holes of the upper and lower base, saturating all the circuits.
3. Using the dedicated software take the reference zero of the pore water pressure.
4. Mount the porous stone disk and filter paper on the loading base.
5. Place the soil sample on the porous stone disk, add the filter paper and the upper porous stone disk.
6. Moisten the side filter paper and place it around the tested sample.
7. With the use of the membrane sock, cover the sample with the appropriate latex membrane.
8. Seal the membrane to the walls of the lower loading plate with three O-Rings. To improve the sealing, it is advisable to dirty the part of steel where it will adhere to the membrane with silicone grease.
9. Using the axial pressure increment commands from the software, increase the axial pressure until the load shaft is lifted by about 1 cm from the lower stroke bottom position. Close the connection valve between the load shaft and the vertical pressure control system to hold the load shaft in a fixed position.
10. Place the upper flange and the three pillars on the lower flange (base plate) by tightening it with the appropriate bolts.

11. Using the dedicated software take the reference zero of the load cell.

12. By moving the ring screw in the upper end of the cell, lower the rod connected to the load cell until contact with the specimen is obtained. The contact is considered complete when the load cell records a value of some kPa.

13. Re-turn and seal the membrane to the walls of the upper load plate as in point 8.

14. Clean and grease the O-Rings along the circumference of the upper and lower flange.

15. Clean the plexiglass cylinder and insert it between the two flanges.

16. Fix the fixing pins of the cylindrical plexiglass container (6) (Figure 59).

17. With the air discharge valve on the upper cell flange open, fill with the water of the cell. When the water level has reached half of the tested sample take the reference zero of the radial pressure transducer. Continue with the complete filling of the cell and close the drain valve.

18. Open the connection valve between the cell and the pressure control system in the cell and by means of the software apply a pressure of about 5 kPa.

19. Slowly open the connection valve between the load shaft and the vertical pressure control system to reach an axial pressure of approximately 5 kPa or equal to the pressure in the cell.

20. Set the automatic control of the pressure in the cell and axial pressure to about 10/15 kPa.

21. Take the reference zeros of the volumometer, vertical displacement, and local transducers.

22. Proceed with the various test steps as described by the (AGI, 1994) reference standards according to the type of test to be performed.

4.2.4 Saturation, Consolidation and Shear phases

As has already been said, the TX CIU test is conducted in three phases:

- Saturation;
- Consolidation ;
- Shear.

The first two phases bring the specimen, completely saturated, to the state of effective stresses established for the shear phase. The stress state to which a specimen is subjected during a triaxial CIU test is axialsymmetric, so the principal stresses always act along the axial and radial directions of the specimen.

4.2.4.1 Saturation

To find the most accurate effective stresses and excess pore pressures, a basic condition of TX CIU test is that the sample must be correctly saturated (Lancellotta, 2012). To verify this, a saturation phase of the specimen shall be performed prior to the triaxial test. The saturation phase consists in the application of a back pressure high enough to saturate all the interstices of the material to produce the total solution of the air bubbles in the fluid. To verify that saturation has occurred, a verification of the Skempton parameter B is performed, which in saturated material conditions is equal to 1. This parameter is estimated by increasing the pressure $\Delta\sigma_c$ in the cell under undrained conditions and measuring the variation of the pore water pressures Δu. The ratio between the two increments is equal to the Skempton parameter B (Eq.24).

$$B = \frac{\Delta u}{\Delta\sigma_c} \qquad \text{(Eq.24)}$$

The control systems of the cell pressure, i.e., the total isotropic stress σ_c applied outside the specimen, and of the back pressure u_0 are typically carried out by pressure fluid lines. Alternatively increments $\Delta\sigma_c$, with drainage closed, and Δu_0, with drainage opened and σ_c constant, are applied. In each phase of increase in cell pressure, the corresponding increase Δu, induced on the pore water pressure u, is measured recording the value of coefficient B.

Saturation is deemed to be achieved when $B \geq 0.95$ is found. Until this condition is not reached, it is appropriate to increase the back pressure u_0 from time to time. It can be calibrated in relation to the degree of saturation S_r of the specimen as shown in Table 7.

Table 7: Relationship between the degree of saturation of the tested sample and the applicable back pressure according to AGI (1994).

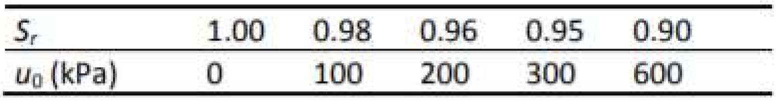

S_r	1.00	0.98	0.96	0.95	0.90
u_0 (kPa)	0	100	200	300	600

The sample is finally left to saturate at the u_0 reached, making sure that $\sigma'_{sat} \leq \sigma'_c$, being σ'_c the effective stress of pre-consolidation planned for testing.

4.2.4.2 Consolidation

The consolidation phase purpose is to bring the specimen to the state of effective stress required for starting the shear phase. After bringing the cell pressure to the value $\sigma'_c + u_0$ and opening the drainage taps the consolidation starts. In this phase, the relationship between changes in volume ΔV_c and time t is recorded; this is then interpreted in the plan $(V,\sqrt{t})$ obtaining the value of the consolidation time t_{100} and the final volume change V_c as indicated in (Figure 63).

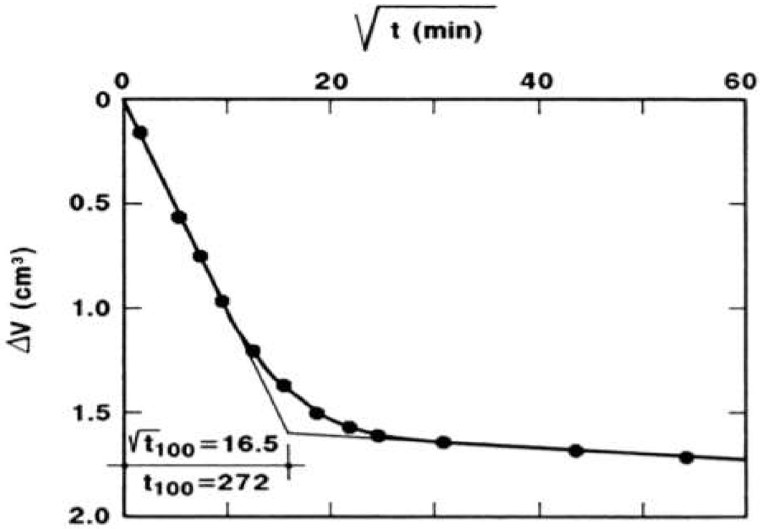

Figure 63: Consolidation curve in isotropic compression phase (AGI, 1994).

The final volume strain, ε_{vc}, can be computed with Eq.25.

$$\varepsilon_{vc} = \frac{\Delta V_c}{V_0} \qquad \text{(Eq.25)}$$

The final dimensions of the specimen, height H_c and area A_c, can be computed with the following Eq.26 and Eq.27.

$$H_c = H_0 \cdot \left(1 - \frac{\varepsilon_{vc}}{3}\right) \qquad \text{(Eq.26)}$$

$$A_c = \frac{V_0 \cdot (1 - \varepsilon_{vc})}{H_c} \qquad \text{(Eq.27)}$$

Where:

- V_0 = initial volume of the specimen;
- H_0 = initial length of the specimen.

4.2.4.3 Shear

When the consolidation phase is finished, the shear phase can start. It is generally carried out under compression conditions: the pressure in the cell is kept constant, while the specimen usually is compressed axially at constant deformation speed. In the case of TX CIU tests, the drainage valves are kept closed throughout the test to prevent volume variation and measure the variation in pore water pressure for the calculation of effective stresses.

As the test goes on with a constant axial deformation speed provided by a pump driven by a stepper motor, the following measurements are recorded:

- the LVDT transducer records the vertical displacements, and the axial strains are automatically computed by a software measurement system, which is connected to it;
- the axial load is measured by an immersion load cell capable of measuring a deviatoric force exerted by the sample by measuring the variation of an electrical signal induced by the deformation of an internal component;
- the measurement of the pore water pressure is guaranteed by the presence of two pressure transducers placed at the base of the drainage circuit. One measures the pressure at the top of the sample and the other at the bottom. In other types of triaxial cell it' s possible to find only one pressure transducer that measure only the pressure at the bottom of the sample.

In this thesis the values have been registered until an axial strain value of 22% is reached.

At the end of the TX CIU test these operations must be carried out:

- stop the press;
- close the cell pressure valve and the pore water pressure valve connected to the transducer to lower the press plate to eliminate axial load;
- bring the pressure to zero in the triaxial cell and empty it;
- open the triaxial cell and with some caution remove the upper drainage head;
- take the sample from the triaxial cell and remove the porous stone disks, latex membrane and lateral drainage filter paper strips from it;
- measure the final water content of the sample by weighing it first under wet conditions and then under dry conditions after drying it in the oven.

4.3 Reconstituted samples preparation

Before describing the operational stages of reconstituted sample preparation used to perform triaxial tests in laboratory, it is important to make a distinction between undisturbed samples and disturbed samples. The undisturbed samples are samples which retain the structure, water content and chemical composition of the soil on site, thus being representative for the determination of shear strength, compressibility, deformability, and permeability parameters (Lancellotta, 2012). Therefore, the main characteristics of the soil remain unchanged, such as density, void index, water content, degree of overconsolidation for clays, relative density for sands. Sophisticated technologies that minimize disturbances are used to extract these kinds of samples. To maintain their unchanged state the samples are sealed directly in the cutting die hermetically with paraffin and transported to the laboratory. Instead, the disturbed samples present themselves like a non-consistent soil that is usually contained in a special box. In this case less refined techniques can be used, which might alter the characteristics of the sample that is taken. The final result is a material with different mechanical characteristics compared to the condition of the site.

In this thesis, according to the procedure used by Milan (2020), the natural material extracted from the Oltrepò Pavese area was chosen in order to realize exclusively the matrix of the reconstituted material. Therefore, starting from samples of heterogeneous material taken from the site, smallest pieces of material were obtained from the latter and then were dissolved in water to separate the marly matrix from the limestone blocks (Figure 64).

Figure 64: Pieces of sedimentary mélange of the Oltrepò Pavese area dissolved in water.

The resulting liquid mixture has been filtered through a 75 µm sieve (ASTM E-11) to obtain as passing only fine material (Figure 65). Then it was subjected to drying cycles in the oven and spatulated to obtain a homogeneous clay mixture with a water content equal to 80% (Figure 66).

Figure 65: Liquid mixture filtered through a 75 µm sieve (ASTM E-11).

Figure 66: Mixture dried in the oven and spatulated.

Then, to produce the heterogeneous reconstituted samples, fine gravel well sieved with a granulometric fuse comprised between 2 mm and 4.75 mm (ASTM E-11) was added to the marly mixture before consolidation (Figure 67).

Figure 67: Weighed fine gravel with sizes comprised between 2 mm and 4.75 mm.

Since the effect of the presence of blocks in the homogeneous matrix is relevant in terms of strength and deformability with percentages greater than 25% (Napoli et al., 2018), it was chosen to reproduce samples with VBP equal to about 25% and 45%. To do this, the amount of gravel needed to reach the desired volumetric percentages within the final specimens was computed. The VBP was evaluated on the final volume of the material at the end of the consolidation, considering for this operation the same loading steps, the same timing and the same final settlement that have been already used by Milan (2020) in his thesis.

Furthermore, in order to limit the consolidation time of the heterogeneous reconstituted material, it was chosen to consolidate a single sample divided into two equal parts having the two different VBP required (Figure 68).

Figure 68: Filling of the consolidometer steel cylinder. One half is filled with material with VBP = 25% and the other half with VBP = 45%.

More details in order to obtain from the heterogeneous consolidated material three samples with VBP equal to 25% and three with 45% VBP are described in the following procedure:

- an initial mixture has been created with VBP equal to 25%, then used for filling the steel cylinder of the consolidometer (Figure 69) proceeding in layers bottom up;
- the thickness of each layer and the number of layers needed for complete filling of the consolidometer were defined;
- the consolidometer cylinder has been virtually divided into two half-cylinders, one containing a mixture with VBP = 25% and another with VBP = 45%;
- the amount of gravel needed to reach a VBP = 45% in half cylinder has been calculated and, from it, the amount of gravel to be added in the VBP = 45% half cylinder for each filling layer;
- gravel has been added, in the quantities calculated in the previous point, for each filling layer;
- in conclusion when the steel cylinder was completely full and closed, the consolidation started.

The operations described above, in fact, have completely eliminated the stress history of the natural material and cancelled the high overconsolidation that characterized it. For this reason, the heterogeneous reconstituted material was subjected to a process of consolidation within a consolidometer, following a set of successive load steps up to an effective vertical stress of 500 kPa. The consolidation thus obtained does not equal that experienced by the natural material on site, but represents the maximum limit reached by the instrumentation of the laboratory used for the preparation of the samples.

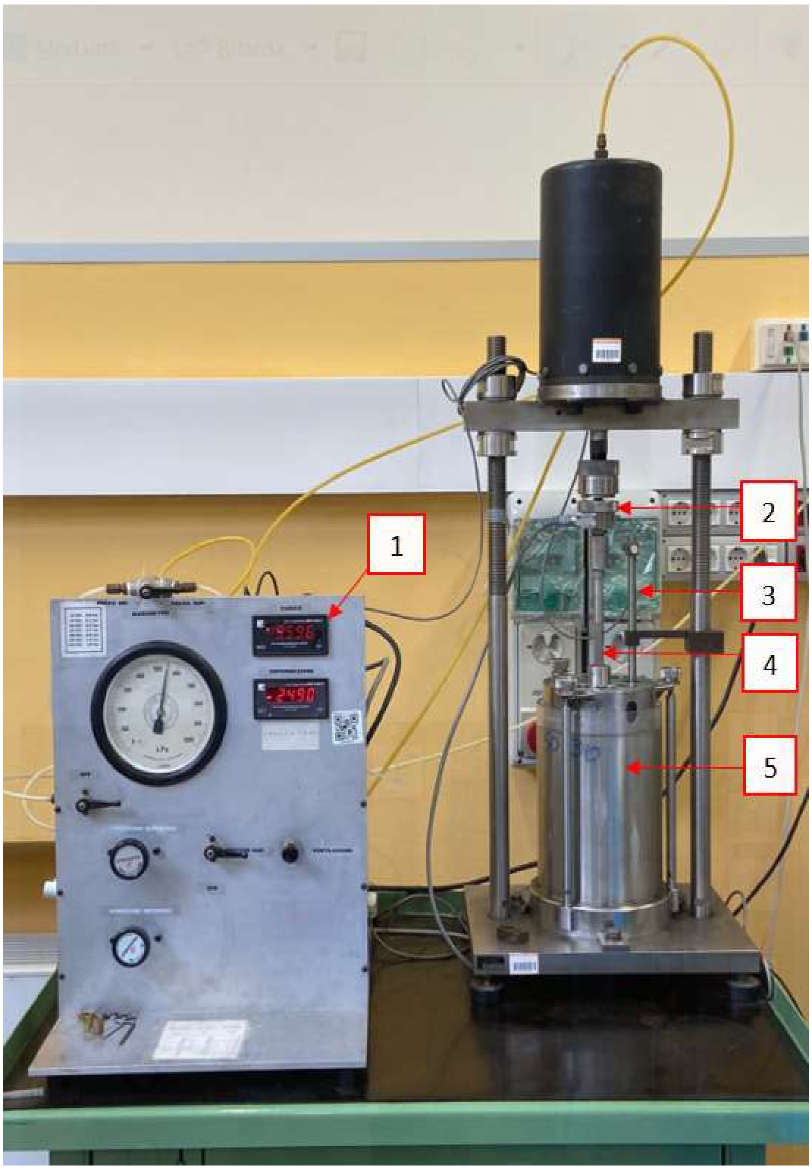

Figure 69: Consolidometer in the Laboratory of Geotechnics of the Polytechnic of Turin used to consolidate the material. It's possible to observe the load cell display (1), the load cell (2), the LVDT transducer to measure the vertical displacements (3), the piston for axial load application (4) and the steel cylinder containing the material (5).

The consolidometer of the Laboratory of Geotechnics of the Polytechnic of Turin used, shown in Figure 69, allows to induce consolidation of a saturated ground by the application of a series of loading steps. The ground is inserted inside a hollow steel cylinder with diameter equal to 155 mm and height equal to 235 mm, at the ends of which two porous stones are placed to decrease the consolidation time and increase drainage. The upper base of the cylinder is free to move in the vertical direction due to a load applied by an air piston and the whole system is constantly immersed in distilled water.

Consolidation takes place by imposing an axial load on the sample in the form of load steps by measuring the vertical lowering over time. When the sample no longer has vertical lowering, the consolidation of the material shall be considered to have been completed. By determining the duration of the load steps in such a way as to allow excess pore pressure to dissipate and to completely transfer the stresses to the solid phase, the soil undergoes a vertical settlement induced by the drainage of pore water.

The definition of the duration of each load step is carried out by analyzing the vertical displacements-time graph and observe that the behaviour shows an asymptotic pattern, which corresponds to the complete dissipation of excess pore pressure, before applying the next load increase.

At the end of the consolidation phase, which took place by imposing on the material 6 steps of vertical load (25, 50, 100, 200, 300 and 500 kPa) for a duration of 44 days, it is possible to extract the consolidated sample (Figure 70).

Figure 70: Sample of consolidated material extracted from the consolidometer.

Starting from the consolidated sample, the cylindrical specimens have been extruded. Given the large size of the consolidometer, 6 cylindrical specimens of heterogeneous reconstituted material were produced respectively divided into 3 specimens with VBP equal to about 25% and 3 specimens with VBP equal to about 45%. The 6 cylindrical specimens had standard dimensions (diameter=38.1 mm and height=76.2 mm) to be tested in triaxial tests. The methodology used to produce them consists in cutting the consolidated sample into 6 wedges with larger dimensions than those of the specimen used in the triaxial test. In each wedge a controlled penetration was performed with a cutting die machine which had the task of cutting the wedge of consolidated sample to obtain a cylindrical specimen with the right size to be tested in the triaxial cell. The 6 wedges obtained from the consolidated sample were paraffinized before being shaped and cut in order to keep their humidity unaltered (Figure 71).

Figure 71: Six wedges of paraffinized consolidated material, three wedges with VBP = 25% and other three with VBP = 45%.

The creation of the cylindrical specimens resulted tricky due to the presence of the large number of blocks inside the consolidated sample which complicate the initial cutting operations and the penetration of the die. During the penetration there was a problem of interaction between the cutting die and the blocks which involves a further alteration of the sample. The blocks along the projection of the cutting die circumference were dragged during the penetration creating holes within the matrix and a surface disturbance effect (Figure 72).

Figure 72: Sample of heterogeneous material after cutting.

This problem leads to more compact areas and highly disturbed areas. The outer surface is therefore uneven and very rough. This characteristic could lead to the rupture of the protective membrane of the sample used in the triaxial test. A further problem, related to the surface cavities of the material, is to create weaknesses of the sample in which the rupture could arise. To overcome this problem, it was therefore decided to manually fill all the cavities with the matrix scraps obtained from the cutting of the specimens (Figure 73).

Figure 73: Final reconstituted specimen of heterogeneous material.

The 6 reconstituted specimens produced were then paraffinized to be able to store them in a wet room until the day of the triaxial test keeping their humidity unaltered (Figure 74).

Figure 74: Paraffinized samples.

4.3.1 Settlement under one-dimensional conditions

In the description of the compression processes, it is considered legitimate to introduce the assumption that they are one-dimensional processes, and it results effective to describe them using as state variables the effective vertical stress σ'_v and the void index e (Eq.28), which is the ratio between the void volume V_v, obtained adding the air volume V_a and water volume V_w, and the solid particles volume V_s (Figure 75*)* (Lancellotta, 2012).

$$e = \frac{V_v}{V_s} \qquad \text{(Eq.28)}$$

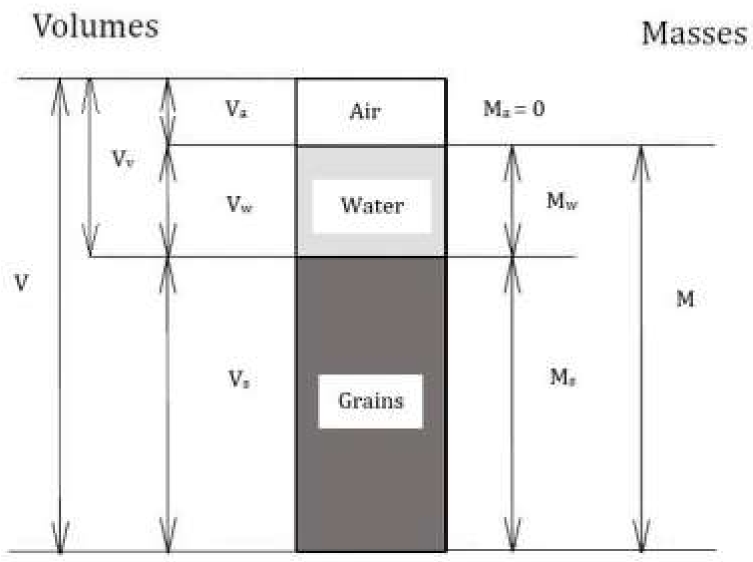

Figure 75: The three separated phases of an equivalent volume of a generic soil sample (Lancellotta, 2012).

The same approximation is considered lawful to represent the process of compression of the material that takes place inside the consolidometer. In this case, settlement can be calculated using the *hedometric method* proposed by Terzaghi in 1943.

In this thesis the material in the consolidometer is consolidated following 6 different load steps increasing up to 500 kPa which is the maximum limit reached by the equipment present in the laboratory. Therefore, the material always remains on the compression branch of the sedimentation compression line (SCL) on the void index-effective stress plan defined by Terzaghi in 1941 and in the end of the consolidation process in laboratory it has an overconsolidation stress σ'_p equal to 500 kPa.

Here the hedometric method is not fully described but as follows only some of its fundamental and useful equations are reported. It is important to introduce two important indexes that play an important role in the settlement computation. The first is the compression index C_c which is the change in the void index for each logarithmic cycle of the vertical effective stress applied (Eq.29).

$$C_c = -\frac{\Delta e}{\Delta \log \sigma'_v} \qquad \text{(Eq.29)}$$

The same definition is applied to the recompression index C_r with reference to the branch of recompression of the SCL. This last index isn't of our interest because as already said above the material always remains on the branch of compression during all the consolidation process.

Assuming as initial conditions the initial height of the generic soil layer H_0, the void index e_0, the effective vertical stress σ'_{v0} and as final conditions the effective vertical stress σ'_{vf} it can be said that in the hypothesis of incompressibility of the particles the following relation is obtained (Eq.30).

$$\frac{\Delta H}{H_0} = \frac{-\Delta e}{1 + e_0} \qquad \text{(Eq.30)}$$

The settlement of the layer ΔH is obtained from the Eq.31.

$$\Delta H = \frac{H_0}{1 + e_0} \cdot \left(C_r \log \frac{\sigma'_p}{\sigma'_{v0}} + C_c \log \frac{\sigma'_{vf}}{\sigma'_p} \right) \qquad \text{(Eq.31)}$$

In the case of this thesis the load path affects only the compression branch therefore the (Eq.32) is obtained.

$$\Delta H = \frac{H_0}{1 + e_0} \cdot \left(C_c \log \frac{\sigma'_{vf}}{\sigma'_p} \right) \qquad \text{(Eq.32)}$$

4.3.2 One-dimensional consolidation theory

As seen in the previous paragraph it is possible to calculate the settlement of a material by assimilating the deformative process to a one-dimensional case. In addition, it is also important to describe the evolution of the settlement over time, which in this thesis it lasted 44 days. In the case of coarse-grained material, characterised by high conductivity, it may be assumed that the settlement occurs at the same time as the application of the load. On the other hand, in the case of fine-grained materials characterized by very low hydraulic conductivity of the order of 10^{-8} m/s, the time required to reach the final settlement can be extremely long. Therefore, a model capable of describing the transient phenomenon that sees the flow of water and the deformation of the solid phase coupled must be built. This phenomenon is called consolidation process and the mathematical model that describes it is indicated, in soil mechanics, as consolidation theory.

The *one-dimensional theory of consolidation*, which was proposed by Terzaghi in 1923, is based on the following assumptions:

- the porous medium is saturated;
- water and soil particles are incompressible;
- the deformations are infinitesimal;
- the flow of water and the displacement of the ground take place only in a vertical direction, which is assumed to be the z direction;
- the solid skeleton behaviour is expressed by the Eq.33

$$\delta\varepsilon_{zz} = m_v \delta\sigma'_{zz} \qquad \text{(Eq.33)}$$

and, within the stress range of interest, the compressibility coefficient m_v, which express the soil compressibility (Lancellotta 2012), is assumed to be constant. ε_{zz} and σ'_{zz} are respectively the strain and the effective stress in z direction.

- the hydraulic conductivity K of the porous medium is also assumed to be constant within the same stress range.

With such assumptions, the mass conservation equations for the solid phase (Eq.34) and the liquid phase (Eq.35) are considered:

$$\frac{\partial}{\partial t}[\rho_s(1-n)]+\frac{\partial}{\partial z}[(1-n)\rho_s v_s]=0 \qquad \text{(Eq.34)}$$

$$\frac{\partial}{\partial t}(n\rho_w)+\frac{\partial}{\partial z}(n\rho_w v_w)=0 \qquad \text{(Eq.35)}$$

where v_s and v_w are respectively the average speed of the water and the average speed of the solid particles, and n is the porosity of the porous medium which is given by the ratio between the void volume V_v and the total volume V.

The solid particles density ρ_s and the water density ρ_w are constant, due to the supposed incompressibility of the water and of the single particles, and they can be eliminated from Eq.34 and Eq.35. Moreover, adding member to member to delete the term $\partial n/\partial t$, Eq.36 is obtained.

$$\frac{\partial v_s}{\partial z}+\frac{\partial}{\partial z}[n(v_w-v_s)]=0 \qquad \text{(Eq.36)}$$

Given the relative motion between fluid and solid phase, Darcy’s law takes the following form (Eq.37).

$$n(v_w-v_s)=-K\frac{\partial h}{\partial z} \qquad \text{(Eq.37)}$$

The hydraulic head h is expressed as follows (Eq.38):

$$h=z+\frac{u_{st}}{\gamma_w}+\frac{u}{\gamma_w} \qquad \text{(Eq.38)}$$

indicating with z the elevation of the point considered with respect a reference plane, γ_w the weight of water in unit volume, u_{st} the initial stationary value of the pore water pressure in steady state, which varies linearly with the depth, and with u the excess pore pressure linked to the perturbation induced by the loads, it is possible to obtain (Eq.39).

$$\frac{\partial}{\partial z}[n(v_w - v_s)] = -K\frac{\partial^2 h}{\partial z^2} = -K\frac{\partial^2 u}{\partial z^2} \qquad \text{(Eq.39)}$$

Substituting the Eq.39 in the Eq.36, the following continuity equation Eq.40 is obtained, in which the velocity of deformation of the solid skeleton appears through the velocity gradient of the solid phase.

$$\frac{\partial^2 u}{\partial z^2} - \frac{\gamma_w}{K}\frac{\partial v_s}{\partial z} = 0 \qquad \text{(Eq.40)}$$

The term $\partial v^s/\partial z$ can be expressed in terms of speed of deformation (Eq.41):

$$\frac{\partial v_s}{\partial z} = -\frac{\partial \varepsilon_{zz}}{\partial t} \qquad \text{(Eq.41)}$$

and introducing the constitutive law of the solid phase (Eq.42)

$$\delta\varepsilon_{zz} = m_v \delta\sigma'_{zz} \qquad \text{(Eq.42)}$$

the Eq.43 is obtained.

$$\frac{\partial^2 u}{\partial z^2} + \frac{\gamma_w}{K} m_v \frac{\partial \sigma'_{zz}}{\partial t} = 0 \qquad \text{(Eq.43)}$$

If the load applied to the surface does not change over time, compliance with the equilibrium conditions in the vertical direction must be (Eq.44):

$$\frac{\partial \sigma_{zz}}{\partial t} = 0 \qquad \forall z \tag{Eq.44}$$

therefore, recalling the definition of effective stress, it must result (Eq.45):

$$\frac{\partial u}{\partial t} = -\frac{\partial \sigma'_{zz}}{\partial t} \tag{Eq.45}$$

and by substituting the latter in Eq.42, the *equation of consolidation* is finally obtained (Eq.46).

$$\frac{\partial u}{\partial t} = c_v \frac{\partial^2 u}{\partial z^2} \tag{Eq.46}$$

The coefficient c_v, which combines the parameters of the porous medium and fluid, is defined as consolidation coefficient (Eq.47):

$$c_v = \frac{K}{m_v g \rho_w} \tag{Eq.47}$$

where g is the gravitational acceleration.

The Eq.46 is a partial differential equation (PDE) and therefore to obtain its solution an initial condition and two boundary conditions, which depend on the case study, must be considered.

5. Test results

In this paragraph the results obtained from TX CIU tests are processed and discussed also in relation to the results obtained in the previous thesis work carried out by Milan in 2020. With this type of study, it is possible to describe the mechanical behaviour of homogeneous and heterogeneous reconstituted material and to analyse the influence of the presence of blocks. In Table 8 all the characteristics of all the TX CIU tests discussed in this thesis are shown.

Table 8: Characteristics of the specimens used to perform triaxial tests. The specimens highlighted in orange were tested and elaborated by Milan in 2020. The specimens highlighted in blue were tested and elaborated in this thesis.

Specimen	VBP	Height	Diameter	Speed of deformation	Effective confinement
-	[%]	[mm]	[mm]	[mm/min]	[kPa]
TX 315	0	76.2	38.1	0.016	25
TX 304	0	76.2	38.1	0.016	50
TX 302	0	76.2	38.1	0.016	100
TX 303	0	76.2	38.1	0.016	200
TX 317	25	76.2	38.1	0.005	25
TX 319	25	76.2	38.1	0.005	50
TX 312	25	76.2	38.1	0.016	100
TX 318	25	76.2	38.1	0.005	200
TX 320	45	76.2	38.1	0.005	25
TX 310	45	76.2	38.1	0.016	50
TX 313	45	76.2	38.1	0.016	100
TX 321	45	76.2	38.1	0.005	200

5.1 Triaxial tests on homogeneous material

The effective confinement values applied to the homogeneous reconstituted samples have been defined in such a way to obtain four failure points on the stress invariants plane, composed by the average total stress p (Eq.48) or the average effective stress p′ (Eq.49) and the deviatoric stress q (Eq.50), that cover a sufficiently broad stress interval.

$$\mathrm{p} = \frac{\sigma_\mathrm{a} + 2\sigma_\mathrm{r}}{3} \tag{Eq.48}$$

$$\mathrm{p}' = \frac{\sigma'_\mathrm{a} + 2\sigma'_\mathrm{r}}{3} = \mathrm{p} - \mathrm{u} \tag{Eq.49}$$

$$\mathrm{q} = \sigma_\mathrm{a} - \sigma_\mathrm{r} \tag{Eq.50}$$

Where:

- σ_a is the total axial stress;
- σ_r is the total radial stress;
- σ'_a is the effective axial stress;
- σ'_r is the effective radial stress;
- u is the pore water pressure.

These four points represent the stress states at failure of the homogeneous material. The equation of the latter, obtained by using the trend line on Excel passing through the four points, allowed to assess the shear strenght parameters, effective friction angle φ′ and effective cohesion c′, of the material. The triaxial test performed using the homogeneous reconstituted sample TX 315 was carried out using an effective confinement of 25 kPa and its results were integrated with those obtained previously by Milan in 2020. In Figure 76 it is possible to observe all the total stress paths (TSP) and effective stress paths (ESP) on the stress invariants plane obtained from the triaxial tests performed on the homogeneous reconstituted samples with different effective confinements.

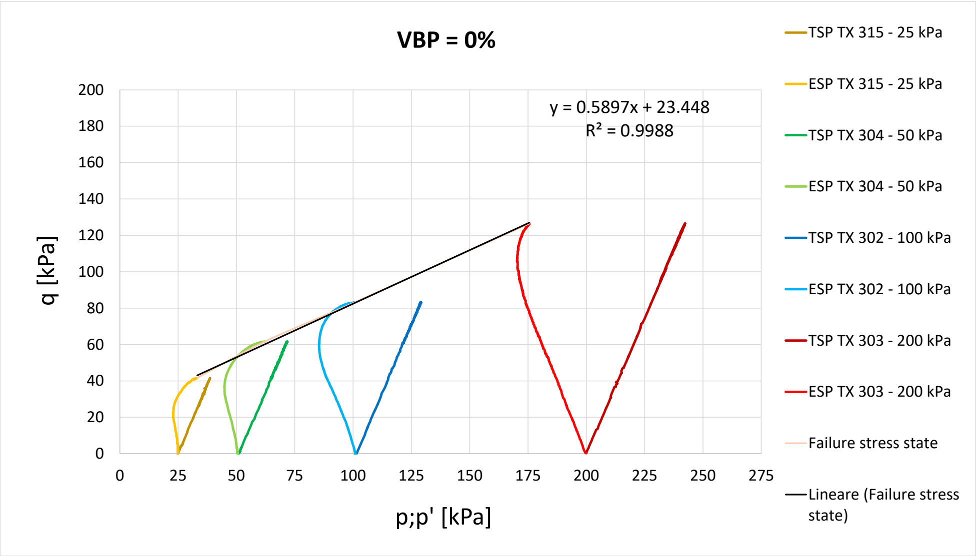

Figure 76: Total and effective stress paths obtained from the four triaxial tests carried out on the homogeneous reconstituted samples with VBP = 0%.

As was already observed by Milan in 2020, also in this case it has been observed that the failure stress states of the four specimens, which correspond to the peaks of the effective stress paths, are almost perfectly aligned on a straight line. The trend line which passes through these four points has an $R^2 = 0.9988$, therefore almost equal to 1. This condition validates the use of the Mohr - Coulomb failure criterion (Eq.51).

$$\tau = c' + \sigma' \cdot \mathrm{tg}(\varphi') \tag{Eq.51}$$

A linear failure envelope in terms of stress invariants on the stress invariants plane (p;p′,q) is considered (Eq.52).

$$q = \bar{q} + m \cdot p' \tag{Eq.52}$$

Knowing the coefficients $m = 0.5897$ and $\bar{q} = 23.488$ of the trend line, it was possible to determine the strength parameters effective cohesion c’ and effective friction angle φ’ on the Mohr plane (σ′,τ) using the following Eq.53 and Eq.54.

$$m = \frac{6 \cdot \sin(\varphi')}{3 - \sin(\varphi')} \tag{Eq.53}$$

$$q' = \frac{6 \cdot c' \cdot \cos(\varphi')}{3 - \sin(\varphi')} \tag{Eq.54}$$

In Table 9 the results of the shear strenght parameters φ′ and c′ obtained are shown.

Table 9: Shear strenght parameters c' and φ' obtained from the homogeneous reconstituted tested samples with VBP = 0%.

VBP	φ'	c'
[%]	[°]	[kPa]
0%	15.6	10.3

It has been observed that both for the consolidated specimen at 25 kPa (Figure 77) and the consolidated specimens at 50 kPa and 100 kPa (Figure 78), there is an obvious failure surface, along which the rupture and the relative motion of the upper and lower portions of the specimen took place. This surface, in accordance with the Mohr - Coulomb failure criterion, represents the plane of maximum ubiquity of the stress. Along this plane the material is subjected to a stress state which, if represented on a Mohr plane, is tangent to the linear failure envelope.

Figure 77: Failure surface of the specimen obtained from the TX 315 test having VBP = 0% after a consolidation of 25 kPa.

Figure 78: In the image on the left the failure surface of the specimen obtained from the TX 304 test having VBP = 0% after a consolidation of 50 kPa is represented. Instead in the image on right the failure surface of the specimen obtained from the TX 302 test having VBP = 0% after a consolidation of 100 kPa is represented (Milan, 2020).

Analysing the TX 315 test results it is possible to affirm the same considerations already done for the TX 304 and TX 302 test results found by Milan in 2020. It was observed that the shear failure surface shows an almost linear shape. On the other hand, as can be seen in Figure 79, the TX 303 test consolidated at 200 kPa showed a failure with barrel deformation, in which the failure surface is not well defined as it is for the shear band found in TX 315, TX 304 and TX 302 tests.

Figure 79: Barrel deformation of the TX 303 test specimen (Milan, 2020).

This difference is explained by the fact that high radial confinements do not allow the union of the microfractures that form inside the material, so the location of the shear band is prevented, and the specimen undergoes a diffuse failure. In the case of lower confinements (25 kPa, 50 kPa, 100 kPa), instead, the shear band is well located and divides the specimen into two portions, which, after failure, move with relative motion. During this phase the decay of the material strength, which induces softening behaviour, and the pore water drainage along the failure surface are triggered. The non-localization of the shear band for high confinement 200 kPa, therefore, is generally associated with the absence of local dissipation of excess pore pressures and decay of deviatoric stress in the post-failure phase. In fact, the specimens tested with high confinements generally show an elastic - perfectly plastic behaviour, as confirmed by the results of the tests carried out. The Figure 80 and Figure 81 show the trends of deviatoric stress q and excess pore pressures Δu as a function of the axial strain ε_a during the four TX CIU tests:

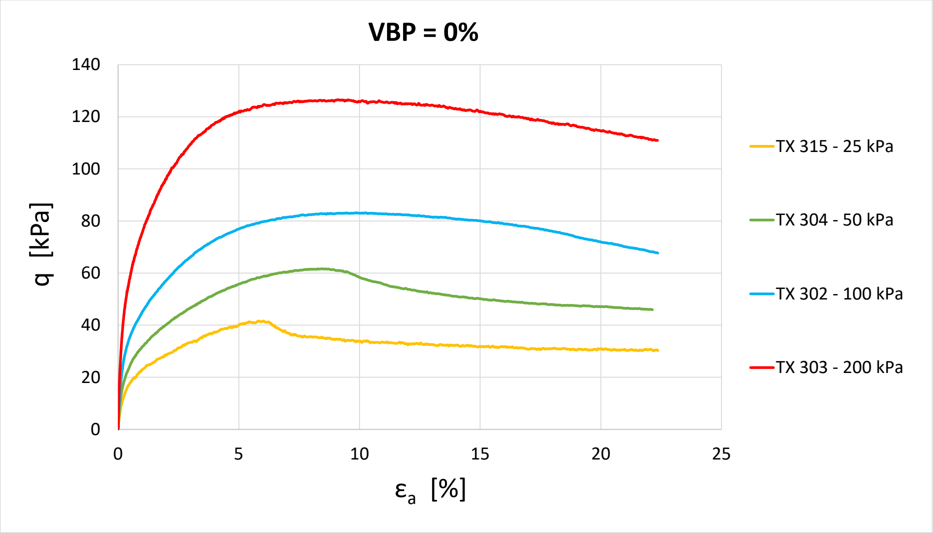

Figure 80: Deviatoric stress trends as a function of axial strain during the four triaxial tests on homogeneous reconstituted samples with VBP = 0%.

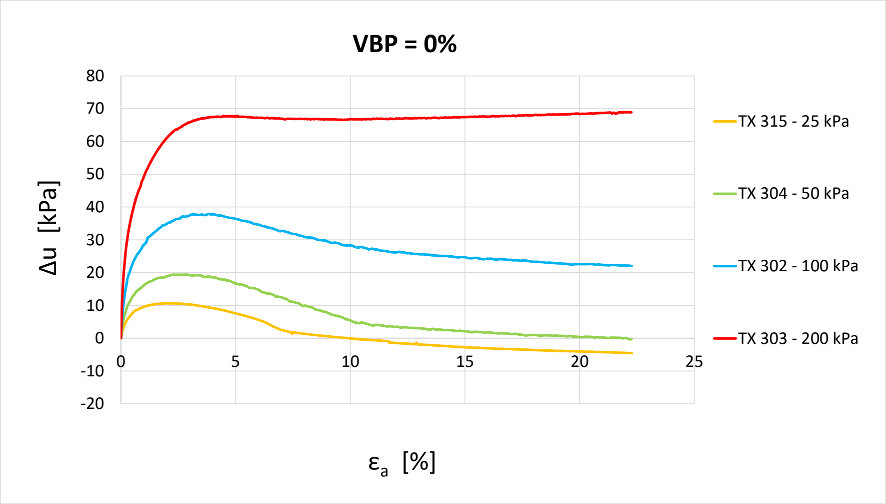

Figure 81: Excess pore pressure trends as a function of axial strain during the four triaxial tests on homogeneous reconstituted samples with VBP = 0%.

By analysing these graphs, it is possible to observe the effects of the radial confinement variation on the strength, deformability, and dilation of the tested samples. In particular, the latter parameter is described by the evolution of the excess pore pressure within the specimen. As expected, the samples consolidated at 25 and 50 kPa showed a more dilating behaviour than the other two.

It is necessary to observe that the measurements at high deformation levels must be treated critically, because their values can be influenced by phenomena that occur within the tested samples which are difficult to assess.

First, the axial stress values acting on the specimen are assessed by the data acquisition equipment as a function of time, dividing the force recorded by the load cell for the surface of the current cross-section. However, this area is assessed on the assumption that the shape of the specimen remains perfectly cylindrical during the test and imposing the volume conservation condition to assess the radius equivalent to the variation in axial strain. This assumption may produce significant errors because of the localization of the shear band or "barrel" deformation of the tested sample.

Secondly, it should also be noted that after the localization of the shear band the internal stress state of the specimen cannot be assumed to be uniform. Finally, it is important to consider that the shear band localization induces a local drainage inside the tested sample, making it locally drained; for this reason, it is wrong to assume that the excess pore pressure assessed by the triaxial equipment are exactly correct and representative of the entire test.

Considering the criticisms described above, it has been observed that the deviatoric stress after rupture shown by the specimens TX 302 and TX 303 respectively confined to 100 and 200 kPa is not descriptive of the mechanical behaviour of the material. In fact, assessing the deviatoric force Q trend recorded by the load cell as a function of the axial strain ε_a of the samples, a significantly less marked and comparable decay was observed with the measurement accuracy of the cell itself which is equal to 0.1% with a full-scale of 5 kN. In particular, the triaxial cell is equipped with an immersion load cell, capable of measure a deviatoric force Q exerted by the specimen by measuring the variation of an electrical signal induced by the deformation of an internal component. Based on the results obtained, it is considered that the behaviour of these specimens is elastic - perfectly plastic. Instead, for the samples TX 315 and TX 304 respectively confined to 25 kPa and 50 kPa, it is possible to confirm the softening behaviour, which is considered to be less marked than that described by the trend of the deviatoric stress q. In Figure 82 the deviatoric force trends described above are shown.

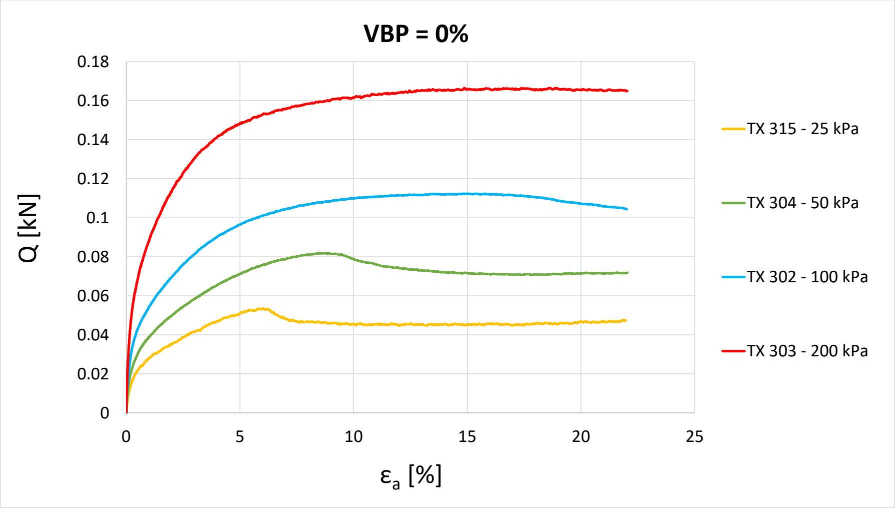

Figure 82: Deviatoric force trends during triaxial tests on homogeneous reconstituted samples with VBP = 0%.

Regarding the deformability of the homogeneous material, it has been observed that it decreases as radial confinement increases. Moreover, the q-ε_a curves show a markedly non-linear pattern in the pre-peak branch, which indicates the variability of the elastic stiffness of the material depending on the strain state. As will be seen in the next paragraph, it has been an important benchmark for comparing the mechanical behaviour of homogeneous and heterogeneous reconstituted material. In Table 10 there are the axial strain values at failure obtained from the four homogeneous reconstituted samples.

Table 10: Axial strain values at failure for each radial confinement σ'_r with VBP = 0%.

Sample	σ'_r	ε_f
-	[kPa]	[%]
TX 315	25	6.0
TX 304	50	8.4
TX 302	100	9.8
TX 303	200	9.1

The TX CIU test allows the determination of the undrained deformability modulus E_u as a slope of the q-ε_a curve; this parameter can then be converted into the drained deformability modulus E as a function of the Poisson's coefficient ν, exploiting the theory of elasticity and using Eq.55 and Eq.56.

$$E_u = \frac{q}{\varepsilon_a} \tag{Eq.55}$$

$$E = \frac{2}{3} \cdot E_u \cdot (1 + \nu) \tag{Eq.56}$$

As mentioned above, the deformability modulus of the four homogenous specimens is variable in function of the strain state. For this reason, the values of the secant deformability modulus relative to the axial strain range [0%; 0.1%] and to a deviatoric stress value equal to half of the deviatoric stress value at failure were computed. Moreover, to be coherent with the procedure applied by Milan in 2020, the secant deformability modulus in correspondence of an axial strain of 9% were evaluated also for the sample TX 315. The Poisson's coefficient ν was assumed equal to 0.25 as done by Milan in 2020. From Figure 80 it has also been observed that for small deformations, which are in the first section of the curves q-ε_a, the stiffness increases as the radial confinement σ'_r increases. This observation, as can be seen in Table 11, is consistent with the values of secant Young's modulus evaluated at half of the deviatoric stress value at failure ($E_{0.5}$) and at different strain levels ($E_{0.1\%}$ and $E_{9\%}$) found by Milan in 2020 and with the sample TX 315 results. Moreover, it is clear that the curves reported in Figure 80 do not show the expected theoretical trend, in which the elastic branches overlap, but the stiffness of the material is affected by the confinement.

Table 11: Values of the secant modulus corresponding to the range of axial strain [0%; 0.1%] $E_{0.1\%}$, to a deviatoric stress equal to half of the deviatoric stress at failure $E_{0.5}$ and to an axial strain of 9% (value of the axial strain at failure) $E_{9\%}$ of the homogeneous reconstituted samples with VBP = 0%.

Sample	σ'_r	$E_{0.1\%}$	$E_{0.5}$	$E_{9\%}$
-	[kPa]	[MPa]	[MPa]	[MPa]
TX 315	25	6.1	2.1	0.3
TX 304	50	9.8	2.8	0.6
TX 302	100	14.5	4.4	0.7
TX 303	200	22.4	8.8	1.2

5.2 Triaxial tests on heterogeneous material

The triaxial tests on the heterogeneous reconstituted specimens with VBP = 25% and VBP = 45% were also conducted considering the same effective confinement values applied to the homogeneous reconstituted samples in such a way to obtain four failure points on each stress invariants plane and to make an overall comparison. In Figure 83 and in Figure 84 it is possible to observe all the total stress paths (TSP) and effective stress paths (ESP) on the stress invariants plane obtained from the triaxial tests performed on the heterogeneous reconstituted samples with VBP = 25% and VBP = 45% and with four different effective confinements 25 kPa, 50 kPa, 100 kPa and 200 kPa.

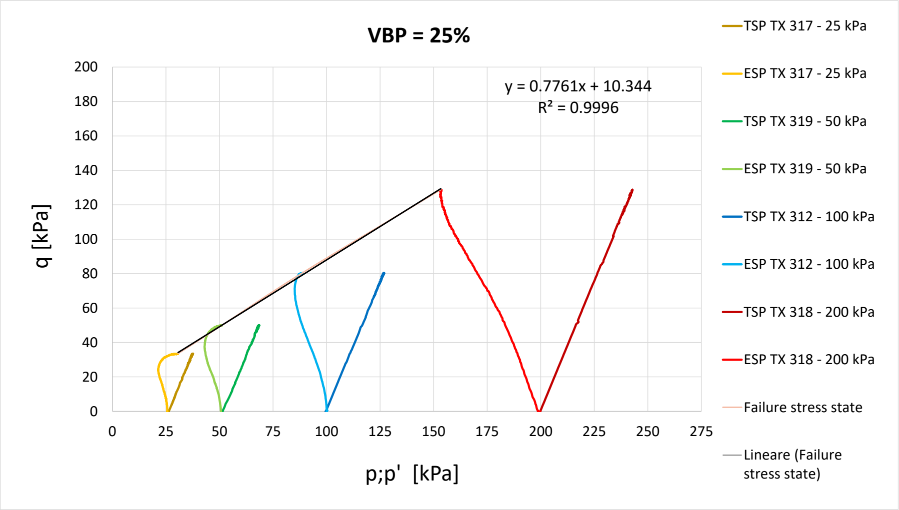

Figure 83: Total and effective stress paths obtained from the four triaxial tests carried out on the heterogeneous reconstituted samples with VBP = 25%.

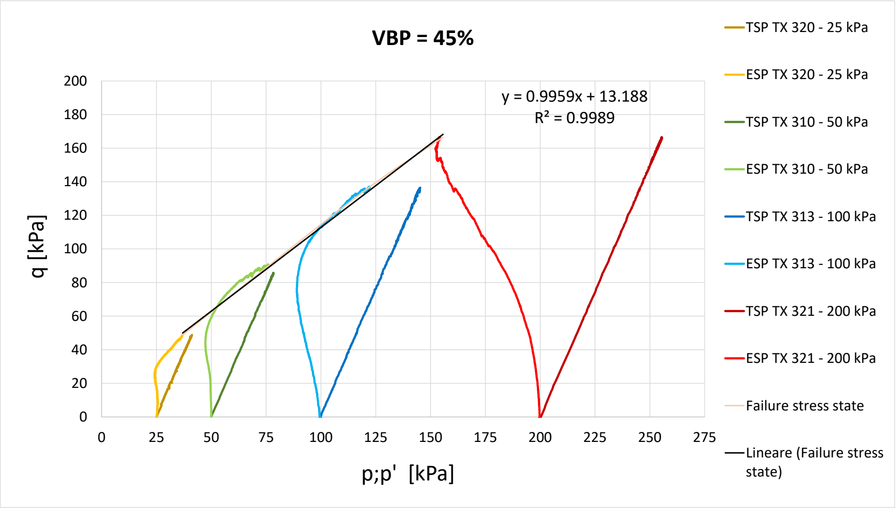

Figure 84: Total and effective stress paths obtained from the four triaxial tests carried out on the heterogeneous reconstituted samples with VBP = 45%.

It has been observed that the four failure stress states points of the four specimens with VBP = 25% and VBP = 45%, which correspond to the peaks of the effective stress paths, are almost perfectly aligned on a straight line. The trend line which passes through the four failure stress state points has respectively an $R^2 = 0.9996$ and $R^2 = 0.9989$, therefore almost equal to 1. This condition validates the use of the Mohr - Coulomb failure criterion (Eq.51). Knowing the coefficients m and $\bar{q}$ of the interpolating lines, it was possible to determine the shear strenght parameters which are the effective cohesion c’ and the effective friction angle φ’ on the Mohr plane (σ′;τ) always using the Eq.53 and Eq.54. In Table 12 are listed the coefficients m and $\bar{q}$ obtained from the trend lines and the shear strenght parameters c’ and φ’ for both cases.

Table 12: Coefficients m and $\bar{q}$ obtained from the interpolating lines and shear strenght parameters c’ and φ’ for the cases with VBP = 25% and VBP = 45%.

VBP	m	$\bar{q}$	φ’	c’
[%]	[-]	[-]	[°]	[kPa]
25%	0.7761	0.9959	20.1	4.9
45%	10.344	13.188	25.3	5.1

As can be seen in Annex 1, it has been observed that all the tested samples with VBP = 25% and VBP = 45% at different effective confinements showed a failure with barrel deformation without any planar shear band localization. The presence of blocks has increased the strength in terms of effective friction angle, allowing the material to retain a residual post-peak deviatoric stress almost equal to that of peak. The overall deformation of the tested samples, in fact, are not characterized by a rigid motion of their upper and lower portions because of the failure, as has been observed in the case of the homogeneous material, but it happened in a diffused way throughout the specimens. In Figure 85 and Figure 86 the trends of the deviatoric stress q as a function of the axial strain ε_a of all the tested specimens with VBP = 25% and VBP = 45% with four effective confinements equal to 25 kPa, 50 kPa, 100 kPa, 200 kPa are shown.

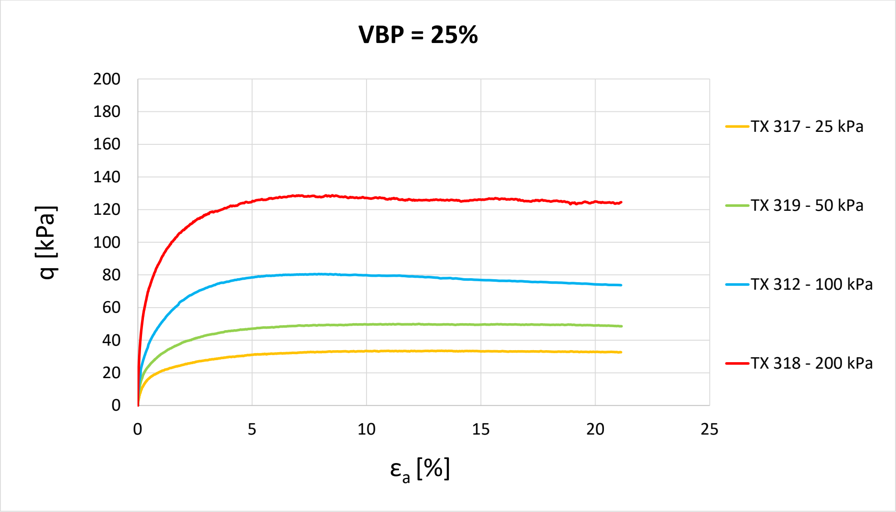

Figure 85: Deviatoric stress trend as a function of axial strain during the four triaxial tests on heterogeneous reconstituted samples with VBP = 25%.

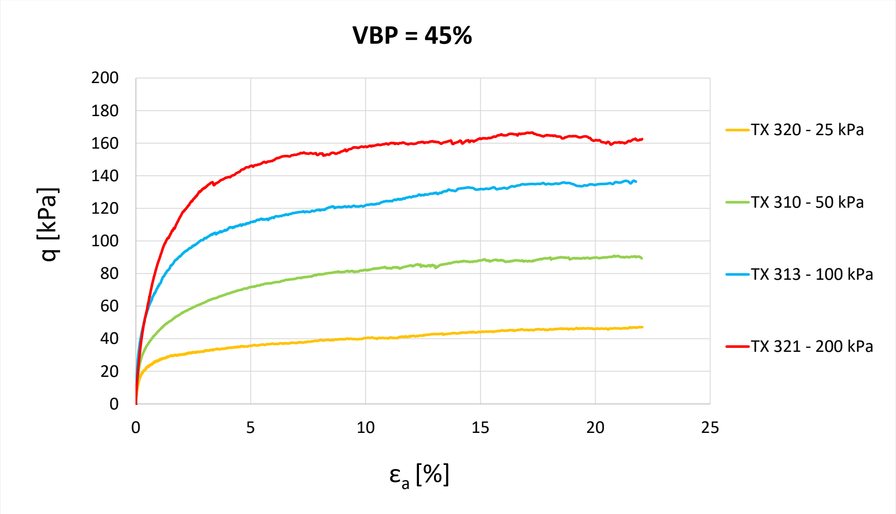

Figure 86: Deviatoric stress trend as a function of axial strain during the four triaxial tests on heterogeneous reconstituted samples with VBP = 45%.

As can be seen from the graphs in Figure 85 and Figure 86, it has been observed that the deformability decreases as radial confinement increases. The q-ε_a curves show a non-linear pattern in the pre-peak branch, which indicates the variability of the elastic stiffness of the material depending on the strain state. In the graph in Figure 85 the elasto - plastic branch of the TX 318 and TX 312 starts from higher deformations than that of TX 317 and 319. Moreover, in the graph in Figure 86 the q-ε_a curves show a more pronounced variation in the post-peak behaviour showing a hardening trend with a more marked stiffness. Also in this case, as can be seen in Table 13 and Table 14, the values of the secant deformability modulus relative to the axial strain range [0%; 0.1%] $E_{0.1\%}$, to the half of the deviatoric stress value at failure $E_{0.5}$ and ,to remain coherent with the procedure applied by Milan in 2020, to the axial strain of 9%, for each tested sample with VBP = 25% and VBP = 45% were evaluated. The Poisson's coefficient ν was again assumed equal to 0.25.

Table 13: Values of the secant modulus corresponding to the range of axial strain [0%; 0.1%] $E_{0.1\%}$, to a deviatoric stress equal to half of the deviatoric stress at failure $E_{0.5}$ and to an axial strain of 9% $E_{9\%}$ of the heterogeneous reconstituted samples with VBP = 25%.

Sample	σ'_r	$E_{0.1\%}$	$E_{0.5}$	$E_{9\%}$
-	[kPa]	[MPa]	[MPa]	[MPa]
TX 317	25	6.5	2.8	0.3
TX 319	50	10.7	3.9	0.5
TX 312	100	13	5.2	0.7
TX 318	200	30.8	14.9	1.2

Table 14: Values of the secant modulus corresponding to the range of axial strain [0%; 0.1%] $E_{0.1\%}$, to a deviatoric stress equal to half of the deviatoric stress at failure $E_{0.5}$ and to an axial strain of 9% $E_{9\%}$ of the heterogeneous reconstituted samples with VBP = 45%.

Sample	σ′$_r$	E $_{0.1\%}$	E $_{0.5}$	E $_{9\%}$
-	[kPa]	[MPa]	[MPa]	[MPa]
TX 320	25	10.2	2.9	0.4
TX 310	50	14.3	3.7	0.8
TX 313	100	23.8	6.5	1.1
TX 321	200	17.9	7.8	1.4

Regarding the excess pore pressures in Figure 87 and Figure 88 obtained respectively from the tested samples with VBP = 25% and VBP = 45%, it can be said that even if they are highly overconsolidated, they do not assume negative values. However, as was expected the maximum excess pore pressures correspond in both cases to the specimens subjected to an effective confinement of 200 kPa, instead the minimum excess pore pressures correspond to those samples subjected to an effective confinement of 25 kPa. The samples consolidated at 200 kPa show a purely contracting behaviour, for which the excess pore pressure increase to stabilize on an asymptotic value. The slight growth shown by the graph in Figure 88 for high axial strain levels is to be considered an instrumental drift.

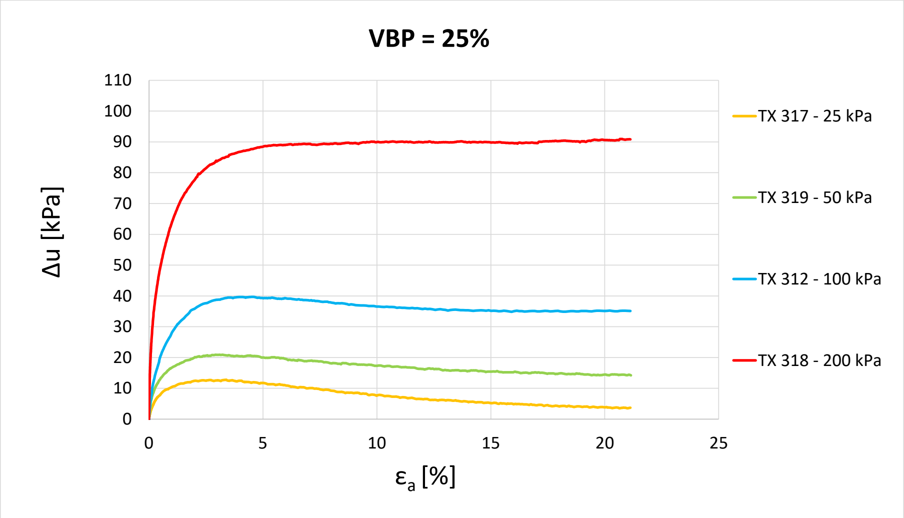

Figure 87: Excess pore pressure trends as a function of axial strain during the four triaxial tests on heterogeneous reconstituted samples with VBP = 25%.

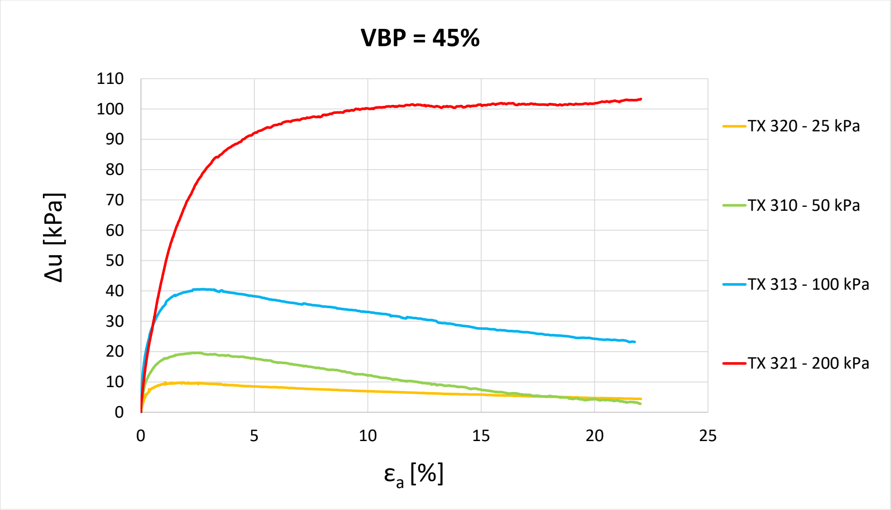

Figure 88: Excess pore pressure trends as a function of axial strain during the four triaxial tests on heterogeneous reconstituted samples with VBP = 45%.

5.3 Test results interpretation

In this paragraph, the results obtained from triaxial tests described above on homogeneous reconstituted samples with VBP = 0% and on heterogeneous reconstituted samples with VBP = 25% and VBP = 45% for each effective confinement applied are compared to state important considerations about the influence of the blocks on the mechanical behaviour of the material under examination.

All the comparison between stress paths of all the tested samples fixing the effective confinement and varying the VBP are reported in Annex 2. As can be observed from the stress paths of the samples with effective confinement equal to 25 kPa and 50 kPa with VBP = 25%, the blocks did not determine increments of the deviatoric stress at failure compared to the homogeneous reconstituted sample with VBP = 0%. On the other hand, in both cases the sample with VBP = 45% has shown significant increments in terms of deviatoric stress. From the comparison between the stress paths of the samples with VBP = 0% and VBP = 25% confined at 100 kPa can be noticed that the deviatoric stress at failure is almost equivalent and in this case the sample with VBP = 45% has shown significant increases in terms of deviatoric stress with respect to the case with VBP = 0% and VBP = 25%. The stress paths of the three samples confined at 200 kPa were characterized by a contracting behaviour. However, also in this case the deviatoric stress values at failure of the specimens with VBP = 0% and VBP = 25 % were almost equivalent and the sample with VBP = 45% has shown significant increases in terms of deviatoric stress with respect to the other two.

In Figure 89 and Figure 90 the q-εa curves of the specimens confined at 25 kPa and 50 kPa with different VBP are shown. It is possible to notice that the three specimens confined at 25 kPa have almost the same trend of the three specimens confined at 50 kPa. However, in both cases there are substantial differences between the mechanical behaviour of the three samples with different VBP. The samples confined at 25 kPa and 50 kPa with VBP = 0% have reached failure at an axial strain of 6% and 8.4% with a deviatoric stress respectively of 41.6 kPa and 61.6 kPa. Instead, in both cases the samples with VBP = 25% have reached failure at higher values of axial strain and deviatoric stress, respectively 13.3% and 12.3% with a correspondent deviatoric stress of 33.5 kPa and 50 kPa. The main differences in mechanical response between the samples confined at 25 kPa and 50 kPa with VBP = 0% and VBP = 25% are represented in the second case by the greater stiffness under pre-failure conditions and no decrease in deviatoric stress after failure with respect the first case. The presence of rock blocks, therefore, has led to a reduction in softening behaviour of the matrix. The overall deformation of the samples with VBP = 25%, in fact, are not characterized by a rigid motion of their upper and lower portions due to failure, as observed in the case of homogeneous reconstituted material with VBP = 0%. This condition appears consistent with the observations concerning the influence of VBP on the development of the failure surfaces in samples of heterogeneous material. The samples with VBP = 25%, in fact, has shown a shear band less net compared to the homogeneous case and not perfectly planar: the presence of rock blocks induced curvature and increased shear strenght along it, allowing the material to retain a residual deviatoric stress post-peak almost equal to the peak. The samples confined at 25 kPa and 50 kPa with VBP = 45% showed a significant increase in ultimate deviatoric stress, which has reached respectively 47.1 kPa and 91 kPa at an axial strain at failure approximately of 21.9% and 20.8%. The trend of the deviatoric stress is therefore almost increased for almost all the duration of the test, in the same way as for hardened materials. This behaviour is consistent with the failure observed, which was not characterised by the localization of a shear band, but it has taken place in a diffused manner inside the samples. In terms of stiffness, as can be seen both in Figure 89 and in Figure 90, the samples with VBP = 0% have higher stiffnesses with respect the samples with VBP = 25%. This peculiar behaviour could be due to the fact that the consolidometer was carried out with two different VBP at the same time. It could also be due to the fact that the samples after extrusion had lateral holes which affected the general behaviour of the test. This last problem, however, is seen more in samples with VBP = 25% compared to those with VBP = 45% because in samples with VBP = 45% there are so many blocks that allow to reach anyway a higher stiffness than the case with VBP = 25%. In addition, it should also be said that the material tested is comparable to a bimsoil and therefore the presence of blocks at certain axial strain levels could also be a factor that for low quantities of blocks, in this case for VBP = 25%, worsens some of the mechanical characteristics of the specimens. In fact, the block-matrix contact is a point of weakness and therefore when there are few blocks in the specimen there is not the resistance effect that the blocks provide but on the contrary, there is the block-matrix contact component that in the case with VBP = 25% goes to accentuate the elements of weakness so the sample resists less.

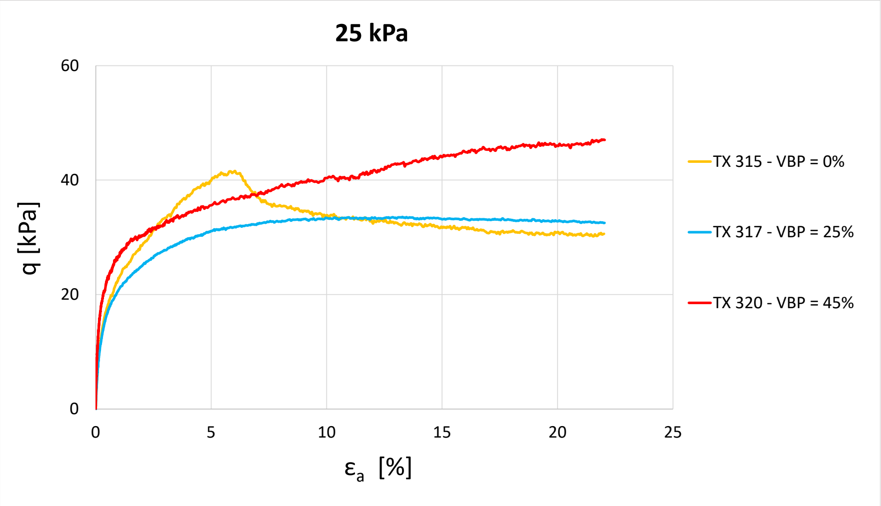

Figure 89: Deviatoric stress trends obtained from triaxial tests confined at 25 kPa as a function of axial strain varying the VBP.

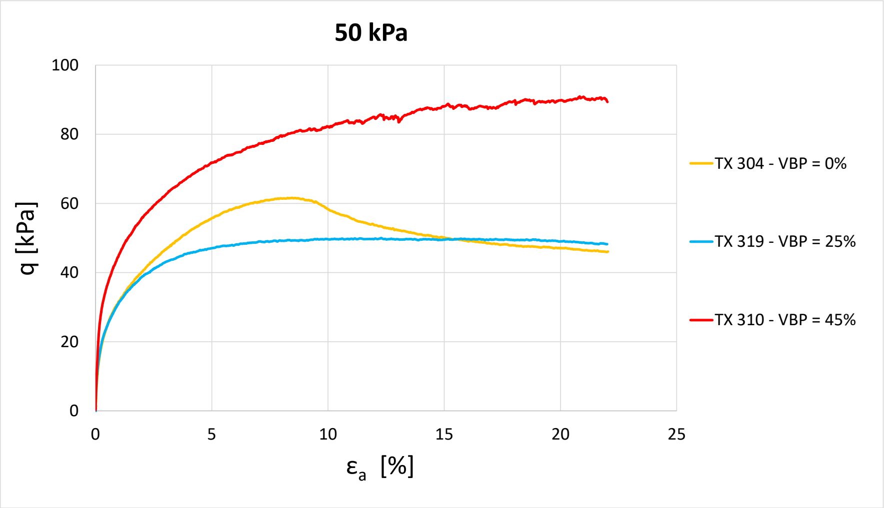

Figure 90: Deviatoric stress trends obtained from triaxial tests confined at 50 kPa as a function of axial strain varying the VBP.

In Figure 91 the q-εa curves of the specimens confined at 100 kPa with different VBP are shown. As can be observed the sample with VBP = 45% shows a higher stiffness with respect the samples with VBP = 0% and VBP =25%. The post-peak behaviour for high confinements with VBP = 45% tends to a hardening behaviour instead in the case of VBP = 0% and VBP = 25% remains substantially the same as in the case of the effective confinements at 25 kPa and 50 kPa with VBP = 25% but reaching higher deviatoric stress values.

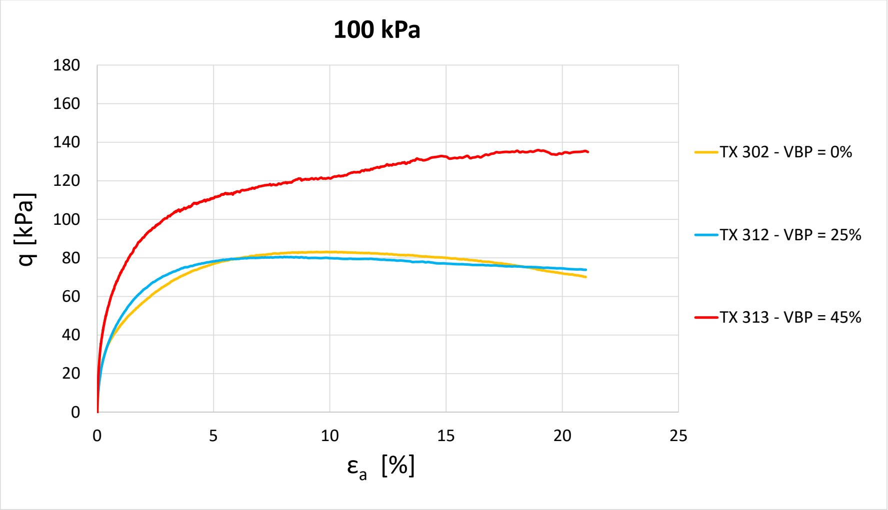

Figure 91: Deviatoric stress trends obtained from triaxial tests confined at 100 kPa as a function of axial strain varying the VBP.

Moreover, the q-ε_a curves of the specimens confined at 200 kPa (Figure 92) have shown very similar trends to those just described for 100 kPa effective confinement. The only differences in this case are that the post-peak behaviour of the sample with VBP = 45% has a less pronounced hardening and in general for all three VBP considered, higher values of deviatoric stress are achieved. Furthermore, the stiffness of all the samples confined at 200 kPa is increased with respect all the previous cases.

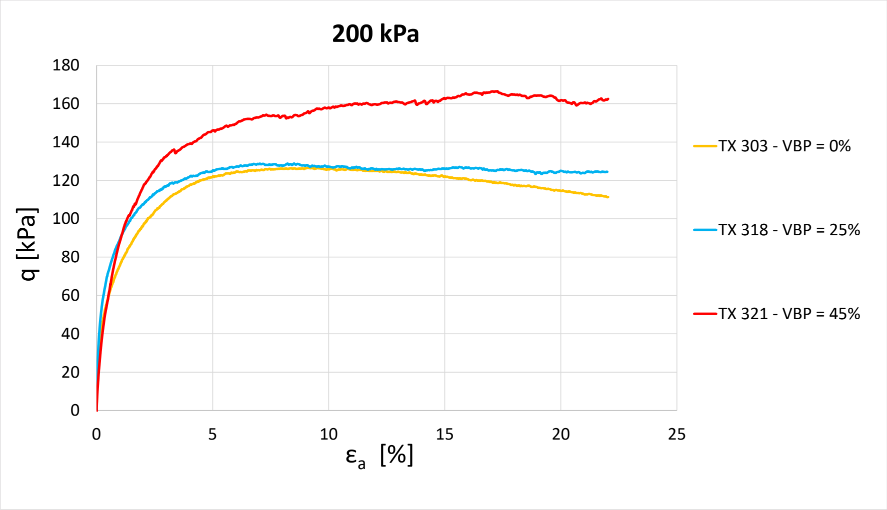

Figure 92: Deviatoric stress trends obtained from triaxial tests confined at 200 kPa as a function of axial strain varying the VBP.

In Table 15 are listed the axial strain values at failure obtained from all the tested samples for each effective confinement in function of VBP. The presence of the blocks led to an increase in deformation at failure.

Table 15: Axial strain values at failure of each tested sample for different effective confinement in function of VBP.

		σ'_r [kPa]			
		25	50	100	200
VBP [%]	0	6.0%	8.4%	9.8%	9.1%
	25	13.3%	12.3%	8.1%	8.5%
	45	21.9%	20.8%	22.2%	17.3%

In order to quantify the stiffness of the specimens subjected to different effective confinements in function of the different VBP of all the tested samples, the values of the secant deformability modulus relative to the axial strain range [0%; 0.1%] $E_{0.1\%}$, to a deviatoric stress value equal to half of the deviatoric stress value at failure were computed. Moreover, to be coherent with the procedure applied by Milan in 2020, the secant deformability modulus in correspondence of an axial strain of 9% were evaluated (Table 16).

Table 16: Values of the secant modulus corresponding to the range of axial strain [0%; 0.1%] $E_{0.1\%}$, to a deviatoric stress equal to half of the deviatoric stress at failure $E_{0.5}$ and to an axial strain of 9% (value at failure of the homogeneous samples) $E_{9\%}$ of all the tested samples for different effective confinements in function of VBP.

		VBP [%]								
		0			25			45		
		$E_{0.1\%}$	$E_{0.5}$	$E_{9\%}$	$E_{0.1\%}$	$E_{0.5}$	$E_{9\%}$	$E_{0.1\%}$	$E_{0.5}$	$E_{9\%}$
		[MPa]			[MPa]			[MPa]		
σ'_r [kPa]	25	6.1	2.1	0.3	6.5	2.8	0.3	10.2	2.9	0.4
	50	9.8	2.8	0.6	10.7	3.9	0.5	14.3	3.7	0.8
	100	14.5	4.4	0.7	13	5.2	0.7	23.8	6.5	1.1
	200	22.4	8.8	1.2	30.8	14.9	1.2	17.9	7.8	1.4

Considering the same deformative level and increasing the VBP, the presence of stone blocks has determined significant stiffness increases with respect the homogeneous reconstituted samples stiffness. It is important to note that the modules of deformability obtained are not to be considered properties of the tested material but are only used as terms of comparison for the analysis of the influence of blocks on the mechanical behaviour. In conclusion, in Annex 3 the differences between the trends of the excess pore pressure as a function of the axial strain for each confinement and varying the VBP are shown. Regarding the strength parameters obtained, as can be seen from the graphs shown in Figure 93 and Figure 94, increasing the VBP the effective cohesion c′ decreases and the effective friction angle φ’ increases. This result can be confirmed by the results obtained by Lindquist in 1994. His tests showed that the samples with the highest VBP had half the cohesion of the matrix, while the friction angle was about 1.5 times greater. This behaviour found explanation in the fact that the greater number of blocks determines on the one hand a greater number of block-matrix contact surfaces, which are points of weakness in which the failure is triggered, and on the other hand greater tortuosity of the failure surface, which is associated with an increase in the friction angle.

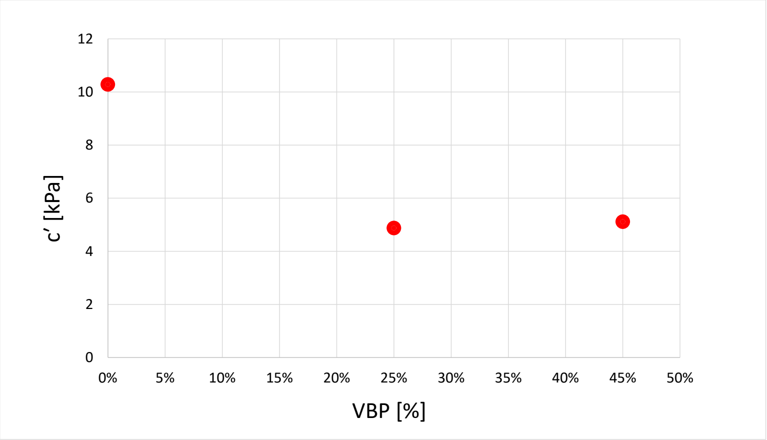

Figure 93: Effective cohesion trend as a function of VBP.

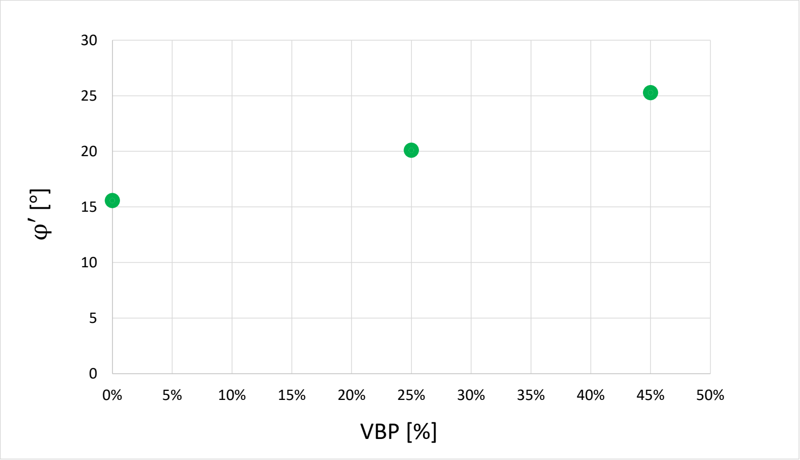

Figure 94: Effective friction angle trend as a function of VBP.

Conclusions and future developments

This thesis, following an introductory part about structurally complex formations, describes firstly the computation of an average tortuosity index of a failure surface and a possible failure zone width occurring in a potentially unstable slope in bimrock. In the second part, the experimental activity carried out in order to define the main characteristics of strength and deformability of a reconstituted block-in-matrix material is described and discussed. The considerable sample-making difficulties associated with the structure of the material under examination have made the execution and interpretation of this activity more complex than the characterization of ordinary soils and rocks. Indeed, tests have been conducted using unconventional methodologies.

Regarding the first part, it can be affirmed that as the VBP increases, the average tortuosity index of the failure surface increases. It is also evident that the variability within the set of 15 tortuous failure surfaces for VBP 25%, 40%, 55% and 70% increases as VBP increases. In this way we can quantify the variability of the failure behaviour of the tortuous surfaces, which changes as the VBP increases. This also allows us to affirm that the tortuous failure surfaces are not only more tortuous as the VBP increases, but also more irregular. So, if a potential failure width within a bimslope is considered, it' s possible to understand how to proceed in the design phase of the work that needs to be realized. In conclusion, it has been possible to say that the possible failure zone width is comprised between 0.1*Lc and 0.5*Lc, where LC is the characteristic engineering dimension. Therefore, having a Lc = 50m, the failure zone width has been evaluated to be comprised between 5 and 25m deep from the surface of the slope.

In the second part of the thesis the study focused on the influence of the volumetric percentage of blocks on the mechanical behaviour of a reconstituted material, evaluated by triaxial CIU tests. The choice to make reconstituted samples was due to the impossibility of coring undisturbed samples of standard shape and size for the execution of the tests directly on natural samples. In addition, this choice allowed a priori control of the volumetric percentage of the blocks (VBP) within the samples analysed. The material analyzed was made by incorporating gravel blocks with dimensions between 2 mm and 4.75 mm inside an overconsolidated marly matrix. The latter was obtained from the real marly matrix that composes a mélange (the Oltrepò Pavese mélange) natural sample by means of a consolidometer. The results obtained showed a significant influence of VBP on mechanical characteristics in terms of friction angle, stiffness, and post-failure behaviour of the material. The samples analyzed, in fact, showed increasing shear strenght as the volume percentage of the blocks increased. The values of deformation at failure, on the other hand, showed the influence of VBP on the plastic deformation capacity only for values of the latter exceeding a threshold between 25% and 45%. The stiffness, after evaluating it in different point of the q-εa curve obtained from each sample, increase as the VBP increase. Furthermore, about the shear strenght parameters it can be said that increasing the VBP the effective cohesion c′ decreases and the effective friction angle φ’ increases. The effective cohesion decreases because when the VBP increases, the block-matrix contact points, which are weak points, increase and consequently the effective friction angle increases.

Based on the experience gained during the experimental campaign, with reference to possible future improvements of the experimental research, it would be useful to perform two different consolidometers containing heterogeneous material with VBP = 25% and VBP = 45% to compare and improve the results obtained in this thesis. In addition, it would be important to find an alternative method for the extrusion of the specimens that does not involve the loss of blocks laterally. Instead, regarding the study about the tortuous failure surfaces the future developments could be to work with other types of materials to find again an indication of the failure zone width to provide to the technicians and to help them in the design phase.

Bibliography

AGI, 1979. *Some Italian experiences on the mechanical characterization of structurally complex formations.* Proc. Intern. Congr. on Rock Mechanics, Montreux, Vol. I, 872-846.

AGI, 1994. *Raccomandazioni sulle prove geotecniche di laboratorio*.

Anagnostou, G., Schuerch, R., Ramoni, M., 2014. *TBM tunnelling in complex rock formations*, in: Barla, G. (Ed.), MIR 2014, XV Ciclo Di Conferenze Di Meccanica e Ingegneria Delle Rocce, Torino, Italy, November 19-20, 2014. CELID, Torino, Italy, p. 331.

Barbier, R., 1977. *A few thoughts on structurally complex formations.* Proc. Int. Symp. on the Geotechnics of Structurally Complex Formations, Capri, Vol. 2, 170-174.

Barton, N., Choubey, V., 1977. *The shear strength of rock joints in theory and practice*. Rock Mechanics Felsmechanik Mécanique des Roches 10, 1–54. https://doi.org/10.1007/BF01261801

Cerise, M., 2019. *Caratterizzazione meccanica di una formazione complessa.*

Cianci, S., Garbin, F., Ori, F., Parente, M., Maurizio, S., 2016. *La caratterizzazione geotecnica mediante prove di laboratorio*. Professione geologo 1–48.

Dzulynski, S., 1977. *Origin, geological history and environmental factors leading to the development of structurally complex formations.* Proc. Int. Symp. on the Geotechnics of Structurally Complex Formations, Capri, Vol. 2, 157-166.

Festa, A., Pini, G.A., Dilek, Y., Codegone, G., 2010. *Mélanges and mélange-forming processes: A historical overview and new concepts.* International Geology Review 52, 1040–1105. https://doi.org/10.1080/00206810903557704

Guerra, C.I., Pinzón, J.J., Prada, L.F., Ramos, A.M., 2016. *Multiscale Modelling of the Slope Stability of Block-in-Matrix Materials*, 458–466.

Irfan, T.Y., Tang, K.Y., 1993. *Effect of the coarse fractions on the shear strength of colluvium*. Hong Kong.

Lancellotta, R., 2012. *Geotecnica*, 4th edition, Zanichelli, Bologna.

Lindquist, E.S., 1994. *The mechanical properties of physical model melange*, in: Oliveira, R., Rodrigues, L.F., Coelho, A.G., Cunha, A.P. (Eds.), 7th International IAEG Congress Vol. 2. A.A.Balkema, Lisbon, Portugal, pp. 819–826.

Medley, E.W., 2004. *Observations on tortuous failure surfaces in bimrocks*. Felsbau 22, 35–43.

Medley, E.W., 2002. *Estimating Block Size Distributions of Melanges and Similar Block-in-Matrix Rocks (Bimrocks)*. Proceedings of 5th North American Rock Mechanics Symposium (NARMS) 509–606.

Medley, E.W., 2001. *Orderly characterization of Chaotic Franciscan mélanges*. Felsbau 19, 20–33.

Medley, E.W., Ceg, P.G., Ge, D., Asce, F., 1994. *The engineering characterization of melanges and similar block-in- matrix rocks (Bimrocks) /.*

Medley, E.W., Sanz, P.F., 2004. *Characterization of Bimrocks (Rock / Soil Mixtures) With Application to Slope Stability Problems*, in: Eurock 2004 & 53rd Geomechanics Colloquium. Salzburg, Austria.

Medley, E.W., Zekkos, D., 2011. *Geopractitioner approaches to working with antisocial mélanges.* Special Paper of the Geological Society of America 480, 261–277. https://doi.org/10.1130/2011.2480(13)

Milan, L., 2020. *Caratterizzazione meccanica di una formazione complessa con struttura a blocco in matrice.*

Montoya-Araque, E.A., Suarez-Burgoa, L.O., 2019. *Automatic generation of tortuous failure surfaces in block-in-matrix materials for 2D slope stability assessments*. Computers and Geotechnics 112, 17–22. https://doi.org/10.1016/j.compgeo.2019.04.002

Montoya-Araque, E.A., Suarez-Burgoa, L.O., 2018. *pyBIMstab: Application software for 2D slope stability analysis of block-in-matrix and homogeneous materials.* SoftwareX 7, 383–387. https://doi.org/10.1016/j.softx.2018.11.003

Montoya-Araque, E.A., Suarez-Burgoa, L.O., Medley, E.W., 2020. *Application of the tortuous surface method to stochastic analysis of bimslope stability*. Bulletin of Engineering Geology and the Environment 79, 5329–5340. https://doi.org/10.1007/s10064-020-01909-5

Morgenstern, N.R., Cruden, D.M., 1977. *Description and classification of geotechnical complexities*, in: International Symposium on the Geotechnics of Structurally Complex Formations. Capri, Italy, pp. 1–19.

Napoli, M.L., Barbero, M., Ravera, E., Scavia, C., 2018. *A stochastic approach to slope stability analysis in bimrocks*. International Journal of Rock Mechanics and Mining Sciences 101, 41–49. https://doi.org/10.1016/j.ijrmms.2017.11.009

Skempton, A.W., 1954. *The pore-pressure coefficients a and b*, in: Geotechnique. pp. 143–147. https://doi.org/10.1680/geot.1954.4.4.143

Sonmez, H., Altinsoy, H., Gokceoglu, C., Medley, E.W., 2006. *Considerations in Developing an Empirical Strength Criterion for Bimrocks.* 4th Asian Rock Mechanics Symposium (ARMS 2006), Nov 6-10 2006.

Sonmez, H., Kasapoglu, K.E., Coskun, A., Tunusluoglu, C., Medley, E.W., Zimmerman, R.W., 2009. *A conceptual empirical approach for the overall strength of unwelded bimrocks*. Rock Engineering in Difficult Ground Conditions - Soft Rocks and Karst - Proceedings of the Regional Symposium of the International Society for Rock Mechanics, EUROCK 2009 357–360.

Terzaghi, K., 1923. *Die Berechnung der Durchlassigkeitsziffer des Tones aus dem Verlauf der hydrodynamischen Spannungserscheinungen, Sitz. Akad*. Wissen, Wien Mathnaturw Kl. Abt. IIa, 132, 125-138.

Terzaghi, K., 1941. *Undisturbed clay samples and undisturbed clays*. J. Boston Soc. Civ. Eng., 28, 211-231.

Wakabayashi, J., Medley, E.E.W., 2004. *Geological characterization of Melanges for practitioners*. Felsbau 22, 10–18.

Whitlow, R., 1996. *Basic Soil Mechanics*, 3rd ed.

Zhang, H.Y., Xu, W.J., Yu, Y.Z., 2016. *Triaxial tests of soil-rock mixtures with different rock block distributions*. Soils and Foundations 56, 44–56. https://doi.org/10.1016/j.sandf.2016.01.004

Annex 1

Images of all the samples with VBP = 25% and VBP = 45% after failure for different effective confinements obtained from the triaxial tests performed.

Figure 95: TX 317 sample confined at 25 kPa with VBP = 25%.

Figure 96: TX 319 sample confined at 50 kPa with VBP = 25%.

Figure 97: TX 312 sample confined at 100 kPa with VBP = 25%.

Figure 98: TX 318 sample confined at 200 kPa with VBP = 25%.

Figure 99: TX 320 sample confined at 25 kPa with VBP = 45%.

Figure 100: TX 310 sample confined at 50 kPa with VBP = 45%.

Figure 101: TX 313 sample confined at 100 kPa with VBP = 45%.

Figure 102: TX 321 sample confined at 200 kPa with VBP = 45%.

Annex 2

Stress paths of all the tested samples fixing the effective confinement at 25 kPa, 50 kPa, 100 kPa, 200 kPa and varying the VBP.

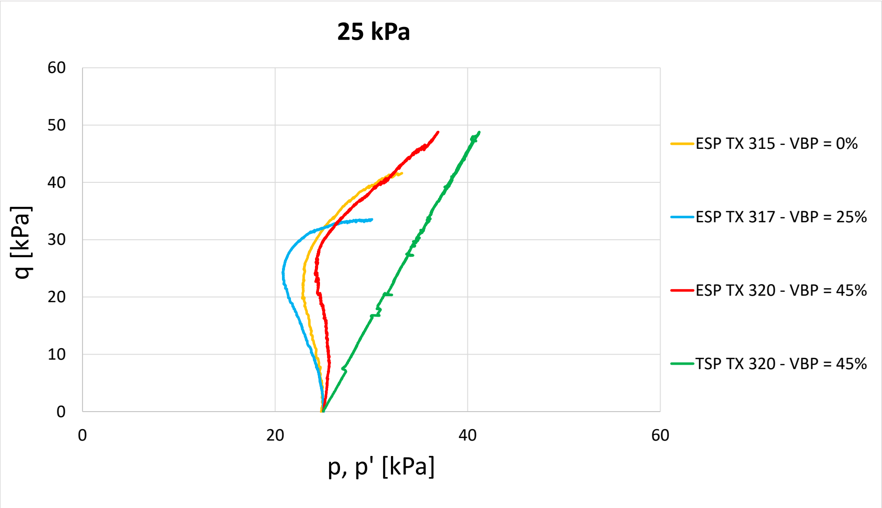

Figure 103: Change in effective stress paths of all the samples confined at 25 kPa as a function of VBP.

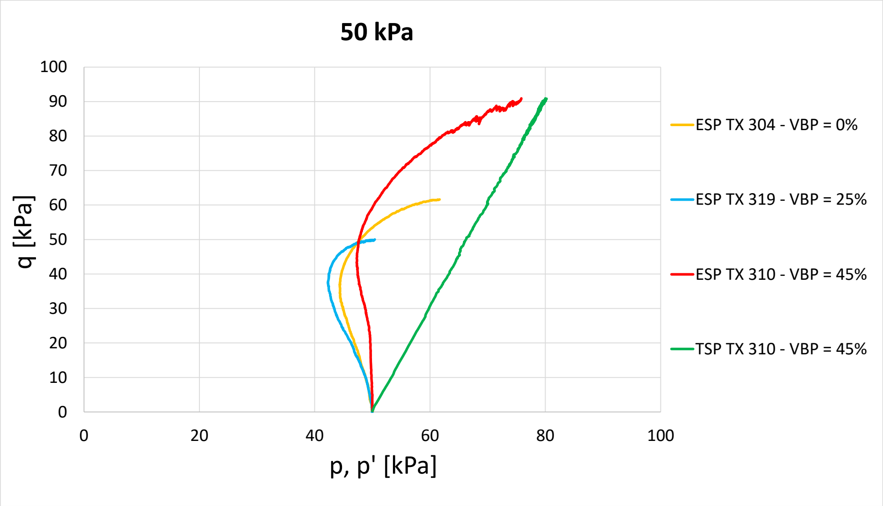

Figure 104: Change in effective stress paths of all the samples confined at 50 kPa as a function of VBP.

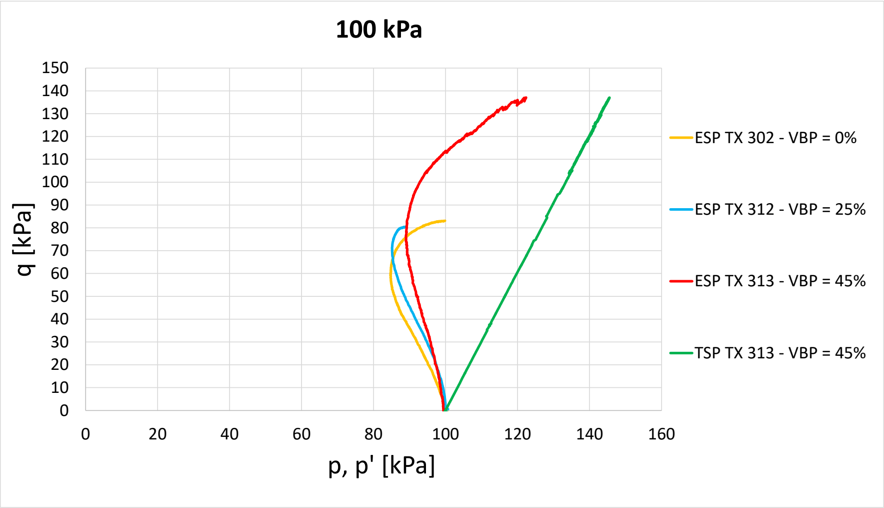

Figure 105: Change in effective stress paths of all the samples confined at 100 kPa as a function of VBP.

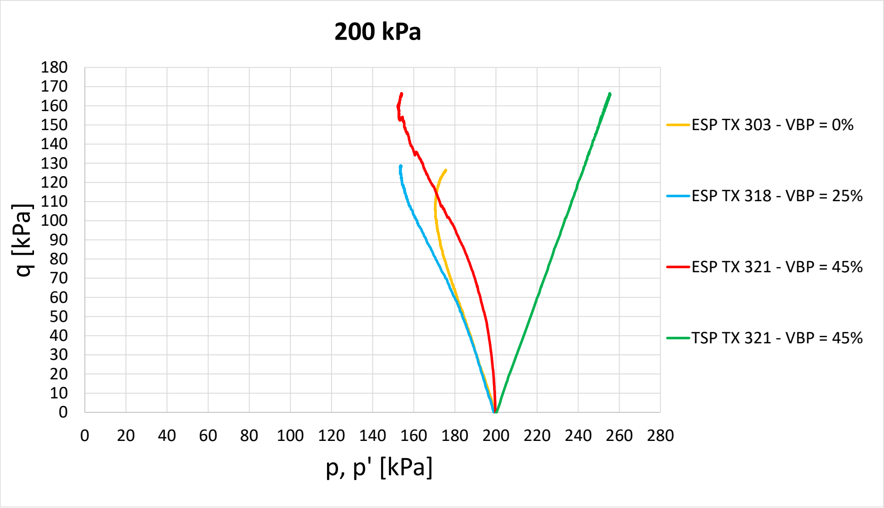

Figure 106: Change in effective stress paths of all the samples confined at 200 kPa as a function of VBP.

Annex 3

Excess pore pressure in function of axial strain of all the tested samples fixing the effective confinement at 25 kPa, 50 kPa, 100 kPa, 200 kPa and varying the VBP.

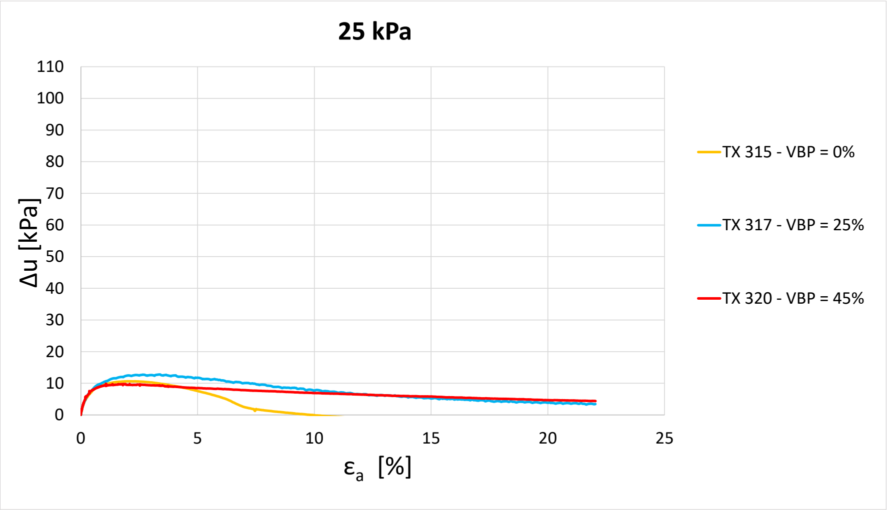

Figure 107: Excess pore pressure trends as a function of axial strain of all the samples confined at 25 kPa varying the VBP.

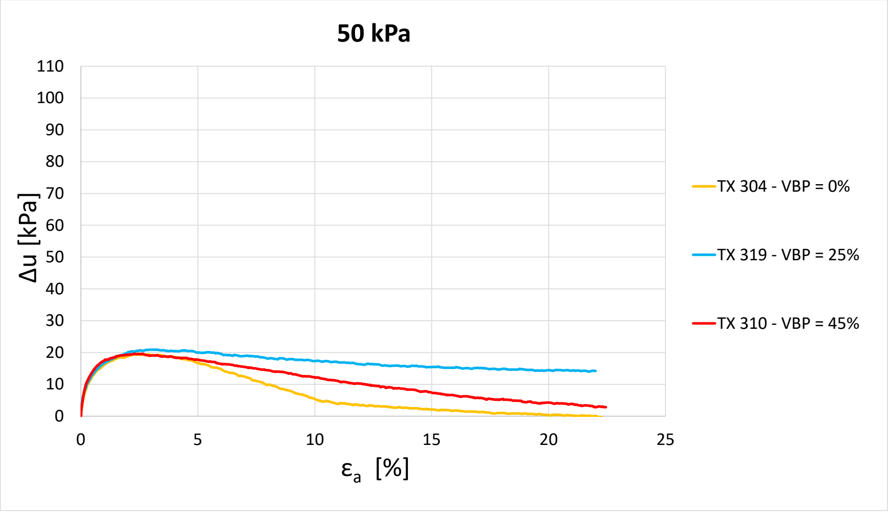

Figure 108: Excess pore pressure trends as a function of axial strain of all the samples confined at 50 kPa varying the VBP.

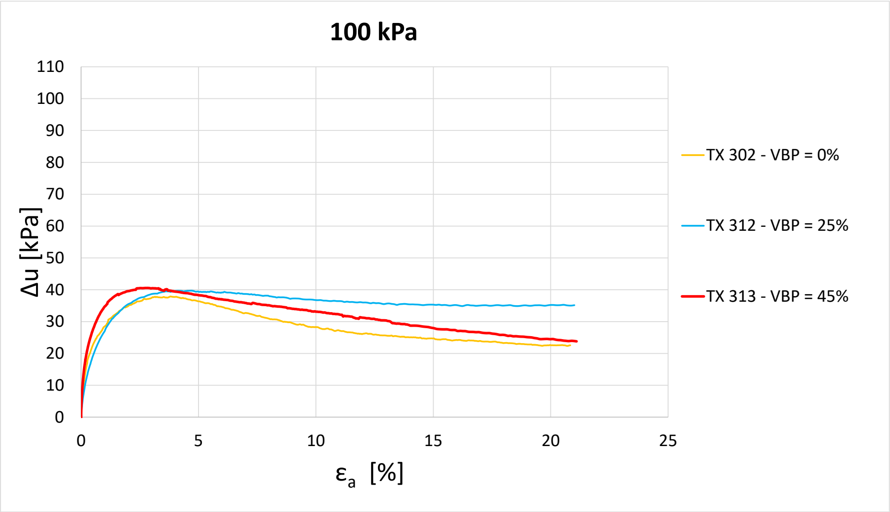

Figure 109:Excess pore pressure trends as a function of axial strain of all the samples confined at 100 kPa varying the VBP.

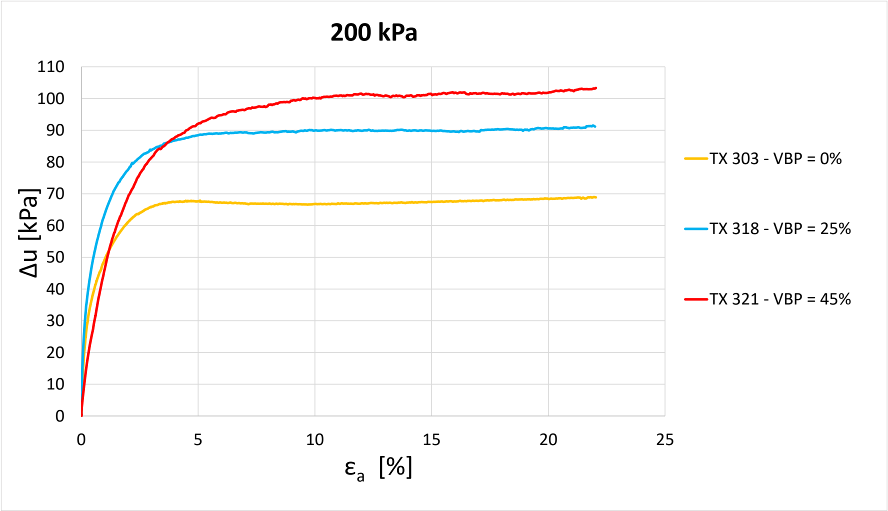

Figure 110: Excess pore pressure trends as a function of axial strain of all the samples confined at 200 kPa varying the VBP.

Acknowledgments

My thanks go first of all to the supervisors of this thesis, Prof.ssa Monica Barbero, Ing. Maria Lia Napoli and Ing. Lorenzo Milan for their support, their wise guide and the help they have given me to write and correct this elaboration.

Thanks also to Ing. Oronzo Pallara and Ing. Giampiero Bianchi who supported me in an excellent way and with much availability and kindness in the laboratory activities.

The last thanks but not for importance go to my parents, Lina and Massimo, who gave me the opportunity to study and to Maria Giulia who supported me in this difficult but fascinating path with all her patience and love.